Piezoelectric Impedance-Based Structural Health Monitoring using Bistable and Adaptive Piezoelectric Circuitry

by

Jinki Kim

A dissertation submitted in partial fulfillment
of the requirements for the degree of
Doctor of Philosophy
(Mechanical Engineering)
in the University of Michigan
2017

Doctoral Committee:

Professor Kon-Well Wang, Chair
Professor Carlos E. S. Cesnik
Professor Bogdan I. Epureanu
Professor Jerome P. Lynch

Jinki Kim

jinkikim@umich.edu

ORCID: 0000 – 0002 – 0921 – 9450

For my wife Mi-Goung and two daughters Hye-Yoon and Hye-Soo

ACKNOWLEDGEMENTS

First and foremost, I want to express my sincere appreciation to my advisor, Professor Kon-Well Wang for his invaluable and continuous support and encouragement of my Ph.D. study.

I am so grateful to have such an outstanding advisor for my graduate study. I gratefully thank my committee members, Professor Carlos Cesnik, Professor Bogdan Epureanu, and Professor Jerome Lynch for insightful conversations and even letting me use lab equipment.

I want to thank Professor Ryan Harne for the enlightening discussions and suggestions when I started this research. I also want to thank former and present SDCL members for the stimulating discussions and the great times spent together.

This research has been supported by the Air Force Office of Scientific Research (FA9550-11-1-0072) and the National Science Foundation (CMMI-DS-1232436). I gratefully thank these sponsors.

Last but not the least, I would like to thank my family and friends for supporting me throughout this study and for flourishing in my life.

TABLE OF CONTENTS

DEDICATION… .... **ii**

ACKNOWLEDGEMENTS .... **iii**

LIST OF FIGURES .... **vii**

LIST OF TABLES .... **xi**

ABSTRACT…… .... **xii**

CHAPTER 1 Introduction and Background **1**

1.1. Structural Health Monitoring Overview 1

1.2. Literature Review of the Piezoelectric Impedance-Based Structural Health Monitoring Methods 3

1.2.1. Data-Based Damage Identification 5

1.2.1.1. Frequency Spectra Analysis Methods 5

1.2.1.2. Time-Series Analysis Methods 8

1.2.1.3. Feature-Based Pattern Recognition Methods 11

1.2.2. Piezoelectric Impedance Model-Based Damage Identification 15

1.3. Problem Statement and Research Goal 19

1.4. Organization of the Thesis 20

CHAPTER 2 Damage Identification Enhancement using Adaptive Piezoelectric Circuitry **22**

2.1. Introduction 22

2.2. Integrated Method for Impedance-Based Damage Identification Enhancement 24

2.2.1. Spectral Element Model of the Electro-Mechanically Integrated System 24

2.2.2. Mathematical Formulation of the Damage Identification Equation 27
2.2.3. Data Enrichment via Adaptive Piezoelectric Circuitry 29
2.3. Numerical Analysis and Case Study 32
2.3.1. Identification of Single Damage under Noise 33
2.3.2. Identification of Multiple Damages under Noise 36
2.3.3. Investigation of Noise Influence on Damage Identification 37
2.3.4. Investigation of the Influence of Modeling Errors on Damage Identification 37
2.3.5. On the Number of inductance Tunings 41
2.4. Experimental Validation 45
2.5. Summary and Conclusion 49

CHAPTER 3 Preliminary Study on Damage Identification with Integrated Bistable and Adaptive Piezoelectric Circuitry 50
3.1. Introduction 50
3.2. Bifurcation-Based (BB) Detection of Frequency Shifts 52
3.2.1. Bifurcation-Based Sensing 52
3.2.2. Overview of Bifurcation-Based Frequency Shift Measurement Procedure 54
3.3. Verification of Bifurcation-Based Detection of Frequency Shifts 59
3.4. Improving Accuracy of BB Frequency Shift Detection through Greater Number of Evaluations 64
3.5. Investigation of Noise Influences 66
3.5.1. Case Study 1: Structure with Mild Damping 66
3.5.2. Case Study 2: Structure with Increased Damping 69
3.6. Summary and Conclusion 71

CHAPTER 4 Predicting Non-Stationary and Stochastic Activation of Saddle-Node Bifurcation in Non-Smooth Dynamical Systems 73
4.1. Introduction 73
4.2. Stochastic Normal Form of Dynamic Saddle-Node Bifurcation 76
4.3. Numerical and Experimental Investigations 79

4.4. Summary and Conclusion 85

CHAPTER 5 Enhancing Impedance-Based SHM using Bistable and Adaptive Piezoelectric Circuitry 87

5.1. Introduction 87

5.2. Overview of Damage Identification Using Adaptive Piezoelectric Circuitry 88

5.3. Impedance Change Measurement Using Bifurcations in Bistable Circuitry Network 90

5.3.1. Overview of Impedance Change Measurement Using a Network of Bistable Circuits 91

5.3.2. Gain Selection Strategy Considering Practical Implementation 95

5.4. Numerical Investigations 99

5.4.1. Case Study: Damage Identification under Noise Influences 99

5.4.2. Damage Identification Study for Various Damage Profiles 103

5.5. Experimental Investigation 105

5.6. Summary and Conclusion 109

CHAPTER 6 Scholarly Contributions, Broader Impacts, and Recommendations… 111

6.1. Summary of Scholarly Contributions and Broder Impacts 111

6.2. Recommendations for Future Work 113

BIBLIOGRAPHY 116

LIST OF FIGURES

Figure 2.1. Illustration of an example beam structure with piezoelectric transducer for measuring piezoelectric impedance. 25

Figure 2.2. Illustration of the structure integrated with the adaptive piezoelectric circuitry. 30

Figure 2.3. Schematic description of the idea of data enrichment to improve the rank-deficiency of the inverse equation. 32

Figure 2.4. (a) Piezoelectric impedance responses of the integrated system for different inductance values (b) Identification of damage on the 13th element of the example beam structure with 10% stiffness reduction. 35

Figure 2.5. Multiple damage identification on the 13th, 18th elements of the beam with 5%, 8% stiffness reduction, respectively. 36

Figure 2.6. (a) Damage identification comparison with varying degrees of noise. (b) Damage prediction error (RMSD). 38

Figure 2.7. Comparison of damage prediction results when there exists (a) 10% modelling error in inductances, (b) 0.1 GPa modelling error in the beam stiffness. 40

Figure 2.8. (a) Singular values of the augmented sensitivity matrix when different numbers of inductance tunings are employed (b) Damage prediction error (RMSD) with respect to the number of inductance tunings. 42

Figure 2.9. Damage prediction error (RMSD) comparison for frequency ranges with different number of resonances. 43

Figure 2.10. Configuration of the experimental beam structure (measures in millimeters). 46

Figure 2.11. (a) Schematic illustration of floating synthetic inductor (b) An example measurement of frequency dependent inductance of the tunable inductor (c)

Comparison of the piezoelectric impedance responses of the baseline model and the experiment result....................47

Figure 2.12. (a) Experimental damage identification on the 25th element of the beam structure (b) Damage prediction error (RMSD) with respect to the number of inductance tunings. 48

Figure 3.1. Schematic of excited host structure to be monitored (here, a cantilever beam) with piezoelectric transducer and attached bistable circuitry. 54

Figure 3.2. (a) Experimental bistable circuit output-to-input voltage frequency response function magnitude, as function of excitation frequency and level, as adapted and re-plotted from [103]. The dashed line on the contour approximately demarcates the threshold between intra- or interwell responses. Example experimental voltage time series for (b) interwell and (c) intrawell dynamics.55

Figure 3.3. (a) Structural response evaluated by the piezoelectric transducer following gain adjustment to serve as bistable circuit input voltage level, highlighting an example activation threshold. (b) Representative output voltage level triggering profile across the spectrum for healthy and damaged structures. 58

Figure 3.4. (a) Configuration of the cantilever beam integrated with bistable and adaptive piezoelectric circuitry. (b) Identification of damage on 2nd element of the cantilever beam with 15% stiffness reduction. 61

Figure 3.5. (a) Tracking of frequency shifts induced by tuning inductances as determined by BB method using 40 runs of the circuit responses each having random initial conditions. (b) Damage identification using the mean results from the 40 resonance frequency shifts. 65

Figure 3.6. Example of (a) noise-free integrated system resonance and (b) that with 32 dB SNR additive noise. 67

Figure 3.7. Frequency shifts determined by DPD or BB approaches as signal-to-noise ratio increases. Numerical values presented are the standard deviations of the approaches for given noise level....................68

Figure 3.8. (a) Damage identification comparison for structure with mild damping and with varying degrees of low level additive noise. (b) RMSD of damage identification. 69

Figure 3.9. (a) Damage identification comparison for structure with increased damping and for varying degrees of low level additive noise. (b) RMSD of damage identification. 71

Figure 4.1. Bifurcation diagrams of (a) smooth and (b) non-smooth saddle-node bifurcation. Solid (dotted) lines indicate (un)stable fixed points.................... 77

Figure 4.2. (a) Schematic diagram of the double-well Duffing analog circuit utilized in experimental analysis. (b) Experimentally measured nonlinear voltage function of the circuit with respect to output voltage amplitude. 81

Figure 4.3. The analytically predicted mean and standard deviation of escape time $\boldsymbol{T}$ using Fokker-Planck equation (solid line) and Kramer's rate (dashed line) are compared with the results obtained by Monte-Carlo simulation (triangle), and experimental measurement (square) with respect to the scaled noise level $\boldsymbol{\alpha}$. Inset figure shows zoomed view for small $\boldsymbol{\alpha}$.. 84

Figure 5.1. Illustration of monitored structure integrated with adaptive piezoelectric circuitry... 88

Figure 5.2. (a) Illustration of a structure integrated with bistable and adaptive piezoelectric circuitry. (b) Example of normalized input voltage levels of healthy and damaged structures. The right inset image shows a representative output voltage level profile with respect to the relative bifurcation threshold values determined by the input gain values of each bistable circuit for healthy and damaged structures. (c) Example bistable circuit output voltage time series for intrawell and interwell dynamics. 93

Figure 5.3. Cumulative probability distribution of bifurcation points.......................... 97

Figure 5.4. Distributions of admittance change measurement errors obtained by the (a) conventional and (b) proposed approaches. Standard deviations are given alongside the Gaussian fits to each distribution plotted as dashed lines......... 101

Figure 5.5. Damage identification results obtained by using (a) conventional method, (b) adaptive piezoelectric circuitry only, and (c) integrated bistable and adaptive piezoelectric circuitry 103

Figure 5.6. Distributions of damage identification errors obtained by using the (a) conventional and (b) proposed methods. Dashed lines included in both plots indicate the first (Q1) and third (Q3) quartiles of each distribution, respectively. 104

Figure 5.7. (a) Configuration of the experimental beam structure integrated with bistable and adaptive piezoelectric circuitry (distances given in millimeters). (b) Schematic illustration of the synthetic inductor. 106

Figure 5.8. Experimental damage identification results obtained by the conventional and new bifurcation approaches are presented in columns (a, b) and (c, d), respectively. Figure (a, c) show the damage identification results and the corresponding damage prediction errors (RMSD) are plotted in (b, d) with respect to the number of inductance tunings. 109

LIST OF TABLES

Table 2.1. System parameters. 33

Table 2.2. Inductance values selected for each resonance peak. 34

Table 2.3. Inductance tuning values used for data enrichment. 41

Table 2.4. Parameters of the tunable inductor, and dimensions of the beam and piezoelectric transducers. 45

Table 3.1. System parameters 60

Table 3.2. Damage-induced resonance frequency shifts measured by DPD and BB methods under inductance tuning. 63

Table 4.1. Experimental system parameters of the double-well Duffing analog circuit. 81

Table 4.2. Scaled noise level $\boldsymbol{\alpha}$ for each sweep rate and additive noise level applied in the experimental investigation. 83

Table 5.1. System parameters. 102

Table 5.2. Experimental system parameters. 106

ABSTRACT

Structural health monitoring (SHM) has been extensively explored for various aerospace, civil, and mechanical systems due to its significant importance in enhancing life-safety and economic benefits. Among various SHM approaches, the piezoelectric impedance-based method has shown excellent potential in identifying small-sized structural defects, while maintaining simplicity in implementation. This method utilizes high-frequency interrogation to detect small damages based on the electromechanical coupling effect of piezoelectric transducers. This coupling effect enables self-sensing, i.e., the transducer serves as sensor and actuator simultaneously, which facilitates simple implementation with reduced number of transducers and associated electrical wirings while consuming relatively low electric power. Furthermore, the damage characteristics such as the location and severity can be identified by employing baseline models.

Despite the promising potentials, important limitations exist to achieve reliable SHM implementations. For example, the number of available independent impedance data set is generally far smaller than the number of required system parameters. As a result, the inverse problems for damage identification are often underdetermined, which severely undermines the reliability of damage prediction since the inverse solutions become extremely sensitive to even small

measurement errors, especially in practical implementations where the response anomaly induced by small-sized damages may be easily suppressed by damping and buried in signal noise.

To address the limitations and advance the state of the art, this thesis presents a novel methodology that fundamentally improves the underdetermined inverse problem and accurately measures the damage-induced impedance variations to reliably identify small damages under noise influences. This is achieved by strategically integrating bistable and adaptive piezoelectric circuitry with the monitored structure. First, adaptive piezoelectric circuitry with tunable inductor is integrated with the monitored structure, which introduces additional degrees of freedom into the system. By systematically tuning the inductance values, the dynamic characteristics of the electromechanically coupled system can be altered; thereby significantly increased number of different independent impedance variations can be obtained with respect to same damage profile. The enriched data set is then utilized to fundamentally improve the underdetermined inverse problem for damage identification. Next, new bifurcation-based sensing approaches are developed, capitalizing on the strongly nonlinear bifurcation in bistable electrical circuits that exhibit dramatic changes in the response due to small input variations. By utilizing the voltage measured from the piezoelectric transducer as an input to the bistable circuit, the enriched damage-induced piezoelectric impedance changes can be assessed by tracking the circuitry bifurcation points. Considering the stochastic and non-stationary influences on the bifurcation points that are theoretically explored in this thesis, a novel bifurcation-

based sensing methodology is developed to provide accurate and robust measurements of the damage-induced impedance changes against unavoidable noise influences. Lastly, the impedance enrichment technique utilizing adaptive piezoelectric circuitry and the advanced bifurcation-based sensing approaches employing bistable circuits are integrated to significantly enhance the reliability of piezoelectric impedance-based damage identification.

The important scholarly contributions of this thesis include: (a) newly developed impedance-based SHM method that fundamentally improves the underdetermined inverse problem, (b) novel integration of the monitored structure with bistable circuits for bifurcation-based sensing, and (c) fundamental understanding of the stochastic and non-stationary influences on the saddle-node bifurcation in non-smooth dynamical systems. The bifurcation-based sensing and identification approaches not only enhances the impedance-based SHM, but has the potential of providing high impact to a broad range of sensing and identification systems that are exposed to noise problem.

CHAPTER 1

Introduction and Background

1.1. Structural Health Monitoring Overview

Structural health monitoring (SHM) is a process of identifying and evaluating damages in civil, aerospace, and mechanical engineering structures, which includes measurements of the system, extraction of characteristics closely related to the damage from these measurements, and analysis to assess the current status of the system [1]. SHM techniques offer great potential in improving life safety by preventing unpredicted catastrophic system failures, such as Aloha Airlines fuselage separation in 1988 and the collapse of I-35W Mississippi River Bridge in 2007, due to unsatisfactory maintenance and ill-conditioned manufacturing process. In addition, we can economically benefit from introducing SHM in the health management of system. The service life of the system can be extended by timely corrective maintenance based on the acquired knowledge on the structural integrity of the system. SHM allows shifting the organization of structural health management from periodically scheduled, time-based maintenance to condition-based maintenance that reduces the cost of labor and the service downtime [1,2]. In recent years, this imperative for monitoring health of structures has led to extensive research in various damage identification approaches suitable across a wide range of engineering applications. The various SHM techniques can be roughly classified into four levels based on the acquired structural damage information in the order of completeness [3]: (a) determination of the presence of damage in structure; (b) detection of damage location; (c) identification of damage location and severity; and (d) prognosis on the remaining service life of the structural system. Damage prognosis involves analysis on various coupled information, such as structural design, damages evaluated by SHM, and the current and future environmental and operational conditions [1]. Since damages generally deteriorate with time to adversely affect the future performance of the system, determination of the early-stage damage is critical in damage prognosis and determining the future management of the structural system. Thus, reliable identification of small-sized damage is one of the common objectives in this research area.

Among various approaches to accomplish this goal, there are two extensively studied classes utilizing structural dynamic responses for damage identification: the vibration-based methods and wave propagation-based methods. The vibration based-methods [4–6] determine damage by measuring the damage-induced changes in modal properties such as natural frequencies [7–9] and mode shapes [8,10,11], mode shape curvatures [12–14]. As these methods utilize measurements of global structural response, they generally benefit from large sensing area and ease in their implementation with small number of transducers since they do not require direct accessibility to damaged site. The location and severity of the damage can be identified by incorporating reliable numerical model into these methods. However, only the lower order modes with large wavelength can be realistically excited and measured; thus, these methods may not be sensitive to early-stage small damages. On the other hand, there have been various Lamb wave propagation-based methods proposed to enhance the interpretation of the transient wave pattern changes for detecting and locating structural damages. Raghaven and Cesnik [15] presented an extensive review on these methods which are usually based on changes in wave attenuations using wavelets [16,17], time-frequency analysis [18], wave reflections [19], and time of flight information [20,21]. These methods have been widely studied and have shown great success in especially detecting small defects though high frequency damage interrogation. On the other hand, these methods generally require physical accessibility to the vicinity of damage location known a priori for measurement due to their localized nature. Since the transient wave responses are very sensitive to local structural profile, it may be challenging to use such responses to accurately identify the damage severity in structures with complex geometries and boundaries [22].

1.2. Literature Review of the Piezoelectric Impedance-Based Structural Health Monitoring Methods

The piezoelectric impedance-based structural health monitoring methods have received great attention in recent years due to their potential in identifying small damages in tandem with maintaining the simplicity in implementation. Park et al. [23] present a comprehensive literature review on the early works developed in the field up to 2001. More recent advancements in the impedance-based techniques are summarized in [24,25]. These methods are pioneered by the piezoelectric impedance model presented by Liang et al. [26] which showed that the electrical impedance of the piezoelectric transducer attached to host structure is a direct combination of the mechanical impedance of the piezoelectric transducer Z and that of the host structure Z_m

$$Y(\omega) = \frac{I}{V} = i\omega M_a \left(\varepsilon_{33}^T - \frac{Z(\omega)}{Z(\omega)+Z_m(\omega)} d_{3x}^2 Y_{xx}^E \right) \qquad (1.1)$$

where Y, V, I, and ω are the electrical admittance (inverse of impedance), input voltage, output current, and harmonic excitation frequency of the piezoelectric transducer, respectively. M_a, d_{3x}, Y_{xx}^E, and ε_{33}^T are the geometry constant, the piezoelectric coupling constant, Young's modulus, and the complex dielectric constant of the piezoelectric transducer at constant stress, respectively. The piezoelectric impedance-based SHM methods are implemented based on the two-way electro-mechanical coupling effect of the piezoelectric transducer to indirectly monitor the damage-induced variations in the structural mechanical impedance by measuring the piezoelectric impedance. As a result, the change of piezoelectric impedance signature with respect to that of the undamaged baseline state is used as damage indicator in these methods. Here, the piezoelectric impedance refers to the electrical impedance of the piezoelectric transducer. Since the piezoelectric impedance can be measured at relatively high frequency [23], these SHM methods are considered to be sensitive to small-sized damages in the structure. As the piezoelectric impedance can be extracted from harmonic responses, harmonic stationary responses enable the identification of both damage location and severity in a systematic and rigorous manner by incorporating reliable numerical model into these methods. Furthermore, due to the electro-mechanical coupling of the piezoelectric transducers, both the actuation and sensing can be done with a single transducer, which provides great merit in implementation by simplifying the electrical wiring and associated hardware with relatively low electric power consumption. Generally, very low voltage, typically lower than 1V, is required for the piezoelectric transducers to generate high frequency excitation in the host structure. Along with these advantageous properties, the development of low-cost impedance measurement circuit [27], and wireless sensor instrumentation [28] have opened the door to practical implementation of the piezoelectric impedance-based SHM methods.

State of the art piezoelectric impedance-based SHM approaches are summarized in the following sections. These methods can be broadly classified into either data-based or physical model-based approaches. The data-based methods can be further categorized based on different types of data assessment techniques to extract damage signatures from the piezoelectric impedance measurements, such as frequency spectra analysis methods, time-series analysis methods, and feature-based pattern recognition methods.

1.2.1. Data-Based Damage Identification

1.2.1.1. Frequency Spectra Analysis Methods

It is well-acknowledged that frequency response functions (FRF) represent dynamic characteristics of a structure. Damages generally cause changes in the structural stiffness, mass, or damping properties of a system and alter the dynamic characteristics, which results in changes in the FRF of the system. While the piezoelectric response curve provides a qualitative measure for damage occurrence, generally an overall-statistical metric is adopted to quantitatively assess the damage characteristics. Since the root-mean-square-deviation (RMSD), which is based on comparison of the FRF before and after damage is occurred in the structure, was proposed as a scalar damage metric in one of the earlier works [29], the majority of the impedance-based SHM approaches have been studied based on the frequency domain analysis. Some representative studies performed at the early stage are briefly reviewed in the following.

Park et al. [30] extended and experimentally implemented the piezoelectric impedance-based SHM method pioneered by Sun et al. [29]. The experimental investigations of impedance-based SHM technique were conducted on various components of typical civil infrastructures. The experimental results on a composite reinforced-concrete wall provided promising possibility of implementing the impedance-based SHM technique to detect small-sized imminent damages in real-time by showing significant variations in the frequency response curve well in advance of actual failure. Experimental investigations were additionally conducted to detect loosened joints on a quarter-scale bridge section and a civil pipe. Furthermore, adverse environmental conditions such as temperature variations are considered in the experimental investigations, and the results confirmed the capability and robustness of the impedance method.

Yang et al. [31] implemented the impedance-based technique to monitor damage propagation, which is also an important objective in SHM since once damage occurs in a structure it may propagate along a certain direction and eventually lead to failure of the structure. Two identical aluminum plates each with holes drilled in sequence towards different directions were tested using piezoelectric transducers bonded the surface. The RMSD index was adopted to quantitatively investigate the damage propagation, which yielded increasing trend of RMSD values as damage propagates in both plates. However, the results showed that the RMSD values significantly depended on the selection of the frequency range for measurements. As a result, it may mislead the evaluation on the actual status of the system and subsequent corrective health management process.

Wang and Tang [32] introduced using an adaptive circuitry idea to enhance the piezoelectric impedance-based damage detection system. The main idea was to integrate the low-cost impedance measurement circuit [27] with an inductive circuit to induce resonant effect in the electro-mechanically coupled system, which dramatically increased the amplitude of admittance measurement and damage-induced change by orders-of-magnitude. The resonant effect is analytically analyzed to provide a guideline for optimal inductance choice and was experimentally verified on an aluminum beam with the proposed piezoelectric circuitry network. Furthermore, Wang and Tang [33] extended the adaptive circuitry idea by adopting negative capacitance element to broaden the frequency range of admittance amplification. Zhou and Zuo [34] modified the adaptive circuitry idea and further increased the admittance magnitude and its sensitivity to damage the by implementing a higher-order resonant circuit.

There have been extensive amount of experimental implementations of the impedance-based method comparing the frequency responses on a number of structures, for instance, civil structures [30,35,36], pipeline systems [37], aerospace structures [38–41], biomedical applications [42–44], and mechanical components, such as gears [45], bolted [46,47], welded [48,49], and bonded [50,51] joints, metallic thin plates [52–54], and composite structures [55–57]. Although the experimental investigations successfully verified the viability of comparing the piezoelectric impedance frequency responses for SHM purpose, most of them only provided detection of the damage occurrence (Level 1) and generally were incapable of identifying the location and severity of damage (Levels 2 and 3). Moreover, since these data-based approaches simply compared the measured frequency response of the damaged structure with that of the healthy baseline structure, the performance of the overall-statistical damage metrics generally adopted to assess the presence and severity of damages are highly dependent on the structure monitored and other measurement conditions, such as frequency range. Zagrai and Giurgiutiu [58] investigated several widely adopted overall-statistic damage metrics, such as RMSD, mean absolute percentage deviation (MAPD), and correlation coefficient deviation (CCD). They found that the third power of the CCD, $(1-R^2)^3$, was the most successful damage metric since it decreased linearly as the distance from the sensor to the crack damage increases in their experiment on metallic thin plates. On the other hand, Tseng and Naidu [53] also investigated the effectiveness of RMSD, MAPD, CCD, and covariance change (COV) and concluded that the RMSD and MAPD were more suitable for representing the growth and the location of damage while the CCD and COV were unfavorable in their experiments. These overall-statistical metrics are mostly phenomenological indices that characterize of the piezoelectric impedance variations, and are not explicitly related to the structural properties such as mass, stiffness, and damping factor. As a result, exact identification of damage characteristics remains to be a challenging issue for this class of approaches.

1.2.1.2. Time-Series Analysis Methods

The time-series predictive models have not been substantially utilized for the piezoelectric impedance-based SHM approaches compared to the techniques based on frequency domain analysis. However, in contrast to frequency domain analysis which generally requires intensive computational resources to average out measurement noise, the time-series analysis exhibits advantage in the improved speed and simplicity, which enables a real-time health monitoring and is favorable for both memory and power management, especially when implementing on low-power, wireless SHM units.

da Silva et al. [59] presented the potential of using autoregressive moving average with exogenous input (ARMAX) models on the piezoelectric impedance time-series data and statistical process control (SPC) charts to detect and locate damages. The proposed algorithm was experimentally verified to detect notches with three different depths in an aluminum beam. The polynomial orders of the ARMAX model were determined as ARMAX (34, 4, 4) using Akaike's information theoretical criteria. The number of outliers exceeding the control limits determined by SPC was employed as damage index, and the damage identification results were compared with the RMSD damage metric obtained by comparing the frequency responses. The number of outliers showed an increasing trend as the damage severity became larger. However, the results provided some false-positive values in the damage identification, and the number of data was deficient for statistical significance.

Figueiredo et.al [60] used a time-series autoregressive model with exogenous inputs (ARX) model to extract damage-sensitive features from the piezoelectric impedance measurements. Since the input is known by the nature of self-sensing with piezoelectric transducers, the ARX model could exploit the property and outperform the traditional output-only autoregressive time-series model. In contrast to the method introduced by Lynch [61] that also adopted the ARX model, the ARX input and output parameters were employed as the damage metric in their research. The performance of the proposed algorithms was experimentally investigated in a composite plate with four piezoelectric transducers bonded on the surface, where five impact damages were manually imposed. ARX coefficient comparisons showed qualitative indication of the damage severities. The correlation coefficient was calculated between each coefficient before and after the impact and was compared to that of FRF-based analysis to present a quantitative measure. Principal component analysis (PCA) provided a clear visualization tool that classifies the damage severity in a two-dimensional plane, and Mahalanobis distance analysis was adopted to show potential in compensating the environmental variations from the extracted features and detect the damage.

Shin, et al. [62] proposed a time-series ARX model to monitor the integrity of bolted joints attached on an unmanned aerial vehicle. Different types of damages are simulated into the structure by loosening the bolts. The ARX time-series predictive model was used as a damage-sensitive feature extractor because the residual errors showed large increase when damage was introduced. The RMSD of the residual errors were estimated from all structural state conditions and were compared with the cross-correlation (CC) coefficient metrics obtained from comparing the impedance FRF data. Furthermore, the Mahalanobis squared distance (MSD) was utilized to successfully remove the effects of the temperature variations, and enabled to detect the damaged conditions under these influences, which was not possible by analyzing the residual errors of the ARX model and the CC features obtained from frequency responses. However, the MSD-based algorithm was not capable of classifying the severity of damages.

Although the time-series predictive models provided promising ability in SHM, the prediction performance significantly depends on the size of the model, which needs to be chosen a priori [61]. Additionally, it should be noted that the time-series models are determined based on the assumption of linear stationary system, thus they may not be favorable for analyzing systems with non-stationary influences [60].

1.2.1.3. Feature-Based Pattern Recognition Methods

Neural networks (NN) are statistical learning models inspired by the functionality of biological nerve systems to estimate generally unknown functions that relate the input to the output of systems. Neural networks have recently gained attention as a promising technique for monitoring and identifying damages in structural systems due to their learning capability of pattern recognition [63]. A neural network consists of a number of processing elements that are connected to form layers of neurons. The NN generates a map between the inputs and outputs by training the network with a priori known patterns of inputs and outputs to determine the optimal synaptic weights and biases. The input variables to the NN are $[x_1, x_2, \dots, x_N]$, which are weighted by $w_{j,i}^h$ and biased by b_j^h, and the output results, $[y_1, y_2, \dots, y_M]$, are passed into the hidden layer. The output of the j-th neuron in the hidden layer is a summation of the biased and weighted inputs as

$$y_j^h = F_h\left(b_j^h + \sum_{j=1}^{\boldsymbol{N}} w_{j,i}^h \cdot x_i\right) \tag{1.2}$$

where the superscript h indicates the quantities of the hidden layer and F_h is a nonlinear function. The output of the NN is similarly weighted and biased by sum of the hidden layer outputs:

$$y_m = F_{\boldsymbol{o}}\left(b_m^{\boldsymbol{o}} + \sum_{j=1}^{H} w_{j,i}^h \cdot y_j^h\right) \tag{1.3}$$

where the superscript o means the output. H is the number of neurons in the hidden layer and F_o is a linear transfer function. In the training step, the inputs are propagated through each hidden layer with a random set of weights and biases until an output is generated. The error is then calculated from a priori known outputs for every input set, and transmitted backwards from the output layer. The biases and weights are optimized to minimize the error. This learning structure is often referred to backpropagation. The NN model is finally determined with nodal biases and weights when a preset error level is reached. The trained NN model is validated and generalized by testing with sets of input data that have not been used in the training step. From the stand point of SHM, the NN is trained to recognize the frequency responses or other extracted features of an intact structure as well as those of each structure with different damage locations and severities. The trained NN will then have a capability of recognizing the location and extent of the individual damage when the responses of the corresponding damaged structure are entered into the NN.

Lopes et al. [63] applied the NN technique to the piezoelectric impedance-based structural health monitoring method for damage detection, localization, and quantification. The proposed damage identification methodology was designed in two steps. The impedance-based method was used to detect and locate structural damage based on the location of the piezoelectric transducer in the first step. In the second step, the backpropagation NN approach was employed to investigate the severity of damage if damage was detected. The NN was designed to utilize eight metrics extracted from the frequency response of piezoelectric impedance for input patterns: (a) the area between the undamaged and the damaged impedance curves, (b) the root means square (RMS) of each curve, (c) the RMS of the difference between the undamaged and damaged curves, and (d) the correlation coefficient between the undamaged and damaged curves. These metrics were obtained for both real and imaginary parts of the impedance, respectively. Experimental investigations were performed on two applications of a quarter scale bridge section and a space truss structure. The results verified that the proposed method is able to quantify the severity of the damages without prior knowledge of the model of structures.

Giurgiutiu and Zagrai [58] introduced the probabilistic neural network (PNN) technique to the piezoelectric impedance-based SHM method for damage detection and quantification. PNN is a special form of NN which implements Bayesian classification approach. Probabilistic density function is assigned for each input neuron and the output is determined as the class having maximum probability. Further detailed information on the PNN can be found in [64]. First, experiments were performed on circular thin plates with piezoelectric transducers attached at the center and circumferential slits introduced as damages at 4 different distances from the center. The damages were quantified by employing the PNN technique and the classification results were compared with overall-statistics damage metrics, such as RMSD, MAPD, and CCD. The PNN utilized the resonance frequencies as input data and provided successful classification of the damage severity which qualitatively matched with the overall-statistics damage metrics. Further experimental investigation on aging aircraft panels validated the PNN-based approach. However, it was required to increase the size and choice of the input vectors to correctly estimate weak damage levels.

Min et al [65] proposed an impedance-based SHM method incorporated with NN pattern analysis technique to estimate the damage type and severity. Since the accuracy and generalization capacity of the NN highly depend on the choice of input patterns, an algorithm to identify damage-sensitive frequency ranges for piezoelectric impedance measurement was included simultaneously. The effectiveness of the proposed NN-based methodology was experimentally validated through identifications of loose bolts and notches on a bolt-jointed aluminum beam and a lab-scale pipe structure. In addition, the proposed approach was embedded into a wireless sensing unit to detect simulated damages in a full-scale bridge. Although the proposed algorithm successfully identified the damage extent and optimal frequency range, it required a large amount of training patterns and enormous computing efforts. For example, the backpropagation-based NN algorithm was trained with 2250 input metrics (250 metrics extracted each from 9 different frequency ranges) for damage detection and optimal frequency identification on a bolt-jointed aluminum beam.

Overall, the NN approach is found successful in classification of damage severities without prior information on the physics-based model of structures. Thus, this technique offers great potential for structures where physics-based model is unknown or not available to accurately identify. However, the accuracy of the damage identification strongly depends on the choice and amount of input pattern that should be known in advance for different damage types. Furthermore, the NN method requires excessive number of training data, and thus computationally expensive. As a result, NN-based SHM methods are generally suitable to structures where a significant database of damage information is available.

1.2.2. Piezoelectric Impedance Model-Based Damage Identification

Piezoelectric impedance model-based methods use mathematical models that theoretically predict the piezoelectric impedance by simulating the actual physical behaviors that govern the electro-mechanically coupled system. In contrast to data-based methods, model-based approaches are capable of predicting system responses to identify the location and severity of damages simultaneously, even for new loading/damage conditions that are not presented in previous data sets. Moreover, developing an accurate model of the piezoelectric transducer and structure interaction enables formulating predictive models to estimate the remaining service life of systems [1]. The physics-based models facilitate sensor self-diagnostics [66], and can be utilized to optimize the frequency ranges and sensor locations when designing the impedance-based SHM approaches [67]. Since the mathematical model of the piezoelectric impedance was first introduced by Liang et al. [26], several analytical models have been developed to improve Liang's model [58,68,69]. Among various advancements, Bhalla and Soh [69], for example, accurately predicted the piezoelectric impedance by considering the bonding layers effect into the model. Giurgiutiu and Zagrai [58] developed an analytical model for two dimensional thin-wall structures, which accounts for the axial and flexural vibrations of the structure, and validated with experimental investigation on circular thin plates.

Finite element methods (FEM) also have been extensively employed to model the piezoelectric impedance for damage identification. Fairweather and Craig [70] formulated a finite element model to accurately estimate the impedance of the piezoelectric transducer bonded onto two dimensional structure, and Littlefield et al. [71] experimentally validated the FEM model. Lim and Soh [72] improved the accuracy of the

FEM model by carefully identifying the damping and bonding layer parameters. Tseng [73] proposed a finite element model-based damage identification method to locate and quantify the structural damage. The piezoelectric impedance of the damaged structure is measured and compared with the numerically obtained frequency response based on a finite element model. The finite element model of the damaged state is then updated to match the numerically simulated response to the measured response from the actual damaged structure as closely as possible through a nonlinear optimization algorithm. The optimized finite element model is finally used to identify the structural damage information. A numerical case study on a beam structure was conducted to illustrate the performance of the proposed algorithm. In addition, the influence of measurement noise on the final damage identification results was investigated. Although the study has demonstrated successful results, FEM may not be suitable for impedance-based SHM since the impedance method generally utilizes high frequency excitation. It is well known that the element size in FEM requires to be significantly smaller than the wavelength involved in analysis to accurately reproduce the system dynamics [74]. As a result, when high frequency interrogation is required, extremely large number of elements are necessary, causing computationally high cost and severely underdetermined mathematical equation for damage identification [9,75,76].

To overcome this shortcoming, spectral element method (SEM) has been introduced for piezoelectric impedance model. In contrast to conventional FEM models that utilize polynomial as shape function, SEM employs a dynamic stiffness matrix which treats the mass distribution in the structural element by using the exact solutions of the governing differential equations of each spectral element as shape function [77]. This means that each element can exactly represent the structural dynamics [78,79]. Thus, a single spectral element can be enough to model the entire section of a homogeneous structure without any discontinuities. As result, SEM can significantly reduce the computational cost. Moreover, each local spectral element can be assembled to form a global stiffness matrix in the same manner as traditional FEM. Thus, SEM is recognized for superior efficiency in computation and accuracy in high frequency dynamic analysis. There have been several studies that utilize the SEM in modeling the high frequency piezoelectric impedance in different structures, such as bolt jointed metallic beams [80] and composite beams [81]. Peairs et al. [82] used the SEM in combination with the low-cost impedance measurement circuit [27] to model the piezoelectric impedance. The model successfully predicted the response up to approximately 20 kHz by employing the Timoshenko beam and Love's rod theories which account for transverse shear, rotational inertia, and transverse velocity effect in axial vibration of beams and plates, respectively.

Ritdumrongkul and Fujino [83] developed a piezoelectric impedance-based damage identification method using SEM to identify the location and severity of damages in multiple-bolted-joint structure. The damage identification algorithm was based on a model-updating technique that minimizes the difference between the measured and the simulated impedances. Laboratory experiment was conducted on a two-joint aluminum beam to illustrate the effectiveness of the algorithm. The structure was numerically modeled by using SEM, and the damage, loosened bolts, was modeled as changes in stiffness and damping of the element. The damage was successfully identified by determining these parameter changes for each bolt by using genetic algorithm that minimizes the discrepancy between the responses. Guo and Sun [84] similarly proposed and numerically validated a damage identification method based on spectral element model-updating algorithm. These studies showed great possibility of using the spectral element model-updating technique for quantitative damage identification. However, although SEM significantly reduces the required computational effort compared to FEM, these methods may still be computationally expensive due to the nature of model-updating techniques.

Wang and Tang [85] proposed an efficient sensitivity-based inverse problem using SEM to identify both the location and severity of damages. First, a spectral element model of piezoelectric impedance was formulated assuming damage as bending stiffness change in each spectral element. Then, the model for damaged case was derived by using first-order Taylor series expansion and approximating the partial derivative of the dynamic stiffness matrix to the elemental stiffness matrix of conventional FEM for small damages. As a result, a linear relationship was formulated between the damage indices and the damage-induced piezoelectric impedance changes. The damage-induced variations were used as input to formulate a sensitivity-based inverse problem that directly extracts the property change of the structural elements. The effectiveness of the proposed method was verified by accurately identifying the location and severity of damages throughout numerical and experimental investigations. The inverse problem of the current approach could still be seriously ill-conditioned, which may significantly reduce the accuracy of identifying the damage location and severity when the response is contaminated by noise and modeling errors. However, these studies were performed without considering measurement noise and uncertainties in the model, which are unavoidable in practical applications.

1.3. Problem Statement and Research Goal

The research efforts reviewed in Section 1.2 illustrate that the piezoelectric impedance-based SHM approaches have significant potential in identifying small-sized damages, while maintaining simplicity in implementation. Especially, the physical model-based approaches have shown successful results in identifying the location and severity of structural damages without requiring information about the damage characteristics a priori. Yet, ***the state of the art impedance model-based SHM techniques still have limitations and gaps for reliable and robust implementation in practical SHM applications.*** The limitations and gaps are summarized as follows.

i. The state of the art piezoelectric impedance model-based SHM techniques often suffer from underdetermined inverse problems [83–85]. In other words, the number of available independent impedance measurement data is generally far smaller than the number of system parameters required to identify small damages with sufficient resolution. Therefore, the inverse solution indicating damage characteristics becomes unstable and thus extremely sensitive to small errors that generally stem from environmental noise, measurement accuracy, and uncertainty in modeling [86].

ii. In addition, it is challenging to accurately measure the piezoelectric impedance changes induced by small damages. Since the impedance response anomalies associated with small-sized damages need to be measured in high frequency ranges, they are suppressed by damping and thus easily buried in noise. However, there are no effective means, which are easy to implement and robust to noise contamination and structural damping, for accurate measurement of the damage-induced piezoelectric impedance variations.

In order to address the problems stated above, ***the goal of this thesis is to overcome the limitations and develop a new method that can accurately and completely capture the features of small-sized damages from piezoelectric impedance variations.*** More specifically, this thesis advances the state of the art piezoelectric impedance-based SHM by achieving the following objectives:

i. Develop a methodology that fundamentally improves the severely underdetermined nature of the inverse problem formulation for accurate damage identification.

ii. Develop a method that accurately determines the damage-induced piezoelectric impedance variations, even under environmental noise and system damping.

1.4. Organization of the Thesis

The thesis consists of six chapters and they are organized as follows. Chapter 2 introduces (a) the impedance data enrichment concept utilizing adaptive piezoelectric circuitry and (b) damage identification algorithm that fully leverages the enriched data set to improve the underdetermined inverse problem. In Chapter 3, the potential of employing bifurcation-based sensing technique for enhancing the measurements of damage-induced impedance changes is then investigated as preliminary study in relatively low frequency range by utilizing bistable circuitry. Chapter 4 presents the theoretical framework for predicting the stochastic and non-stationary influences on the activation of saddle-node bifurcation in non-smooth dynamical systems. In Chapter 5, the insights developed in the preceding chapters will be combined to significantly enhance the impedance-based damage identification under noise influences. Following the technical contributions of this thesis, the scholarly contributions and broader impacts are summarized in Chapter 6 with recommendations for future directions towards the improvement and implementation of the insights developed in this thesis.

CHAPTER 2

Damage Identification Enhancement using Adaptive Piezoelectric Circuitry

2.1. Introduction

As stated in Chapter 1, the piezoelectric impedance-based damage identification incorporated with the spectral element model shows promising results. However, the current approach may be inhibited by the fact that the inverse problem could still be seriously rank-deficient. This issue would significantly reduce the accuracy of identifying the location/severity of the damage, especially with unavoidable measurement noise and modeling error.

In general, the sensitivity based inverse problem for damage identification can be formulated as $\mathbf{G} \times \mathbf{d} = \mathbf{m}$ where $\mathbf{G}$ is the sensitivity matrix that is derived from the system model, vector $\mathbf{m}$ is the measurements of impedance changes in this study, and $\mathbf{d}$ is a vector that contains the damage information, which will be solved inversely from this equation. The detailed derivation of $\mathbf{G}$, $\mathbf{m}$, and $\mathbf{d}$ is presented in Section 2.2. In case the inverse problem is ill-posed, or $\mathbf{G}$ is rank-deficient, a generalized inverse of $\mathbf{G}$, such as the Moore-Penrose pseudoinverse [86], can be employed to solve the least square solution $\tilde{\mathbf{d}}$.

This generalized inverse solution can be analyzed by using singular value decomposition (SVD). The matrix $\mathbf{G}$ can be factored into $\mathbf{G} = \mathbf{USV}^{\mathrm{T}}$ where $\mathbf{U}$, $\mathbf{V}$ are orthogonal matrices, and $\mathbf{S}$ is diagonal matrix with diagonal entries $\mathrm{s_i}$, called singular values, listed in descending order. We can express the approximate solution of the inverse problem in terms of SVD as following

$$\tilde{\mathbf{d}} = \mathbf{G}^{-1}\mathbf{m} = \mathbf{VS}^{-1}\mathbf{U}^{\mathbf{T}}\mathbf{m} = \sum_{\mathrm{i}=1}^{\mathrm{n}} \frac{\mathbf{u}_{\mathbf{i}}^{\mathbf{T}}\mathbf{m}}{\mathbf{s}_{\mathbf{i}}} \mathbf{v}_{\mathbf{i}} \tag{2.1}$$

where $\mathbf{G}^{-1}$ is the generalized inverse of $\mathbf{G}$, $\mathbf{u}_{\mathrm{i}}$, $\mathbf{v}_{\mathrm{i}}$ are the i-th column vectors of the orthogonal matrices $\mathbf{U}$, $\mathbf{V}$, respectively. When error $\mathbf{e}$ is now introduced in the measurement, the inverse problem can be modified as $\mathbf{G} \times \mathbf{d}^* = \mathbf{m} + \mathbf{e}$. The generalized inverse solution of this equation $\mathbf{d}^*$ can be computed as below:

$$\mathbf{d}^* = \mathbf{G}^{-1}(\mathbf{m} + \mathbf{e}) = \mathbf{G}^{-1}\left(\mathbf{G} \times \tilde{\mathbf{d}} + \mathbf{e}\right) = \tilde{\mathbf{d}} + \mathbf{G}^{-1}\mathbf{e} \tag{2.2}$$

It is useful to examine the effect of error in the generalized inverse solution by rewriting Eq. (2.2) in the form of Eq. (2.1).

$$\mathbf{d}^* = \tilde{\mathbf{d}} + \sum_{\mathbf{i}=1}^{\mathbf{n}} \frac{\mathbf{u}_{\mathbf{i}}^{\mathbf{T}}\mathbf{e}}{\mathbf{s}_{\mathbf{i}}} \mathbf{v}_{\mathbf{i}} \tag{2.3}$$

When the inverse problem is ill-posed, the singular values of matrix $\mathbf{G}$ decrease fast with respect to singular value index *i*. As a result, very small singular values in the denominator of Eq. (2.3) can significantly amplify the error term, and the desired solution without error $\tilde{\mathbf{d}}$ gets buried in this amplified error term. Thus, when the inverse problem is ill-posed, the generalized inverse solution becomes extremely sensitive to even small amount of error in the data. To advance the state of the art, this chapter aims to address this issue and develop an approach that can identify the damage from piezoelectric impedance variations with high accuracy. In conjunction with the prior research on the impedance-based damage identification formulated by SEM [85], this chapter focus on designing an adaptive piezoelectric circuitry with inductive element to enrich the piezoelectric impedance responses and reduce the degree of rank-deficiency of the inverse problem, and developing inverse identification algorithms that can effectively utilize the enriched data set.

The following sections discuss the damage identification method based on the SEM, and introduce the new approach using adaptive piezoelectric circuitry for impedance data enhancement. Numerical and experimental investigations with a series of case studies are provided to examine the effectiveness of the proposed concept.

2.2. Integrated Method for Impedance-Based Damage Identification Enhancement

In this section, the concept of incorporating adaptive piezoelectric circuitry to the host structure for piezoelectric impedance measurement is mathematically derived using the spectral element method, and the damage identification algorithm that exploits the enhanced impedance measurement is introduced.

2.2.1. Spectral Element Model of the Electro-Mechanically Integrated System

The schematic of an example fixed-fixed beam integrated with electric circuit for piezoelectric impedance measurement is shown in Figure 2.1. The piezoelectric transducer is assumed to be perfectly bonded onto the P_1-th element of the beam structure that is discretized into N elements. When the piezoelectric transducer is excited by voltage V_e, moment M_p is generated due to the reverse piezoelectric effect [82,85].

$$M_p = K_1 V_e \tag{2.4}$$

$$K_1 = \frac{b_p E_p d_{31}}{2h_p(1+i\omega R C_p)}\left[\left(\frac{1}{2}(h_p + h_b)\right)^2 - \left(\frac{1}{2}h_b\right)^2\right] \tag{2.4a}$$

where b_p, h_p, d_{31}, E_p, and C_p are the width, thickness, piezoelectric coefficient, elastic modulus, and capacitance of the piezoelectric transducer, respectively. h_b is the thickness of the beam, ω is the excitation frequency, and R is the resistor serially connected to the piezoelectric transducer. The generalized force vector **F** can be expressed by using a vector $\mathbf{\Phi}_p = \left[(0,0)_{i=1}, (0,0)_{i=2}, \cdots, (0,1)_{i=P_1}, (0,-1)_{i=P_1+1}, \cdots, (0,0)_{i=N+1}\right]$ that indicates the location of the transducer.

$$\mathbf{F} = M_p \mathbf{\Phi}_p^{\mathrm{T}} \tag{2.5}$$

Timoshenko beam theory is applied to SEM for modeling the beam structure since the impedance-based damage interrogation is conducted in high frequency range. The displacement magnitude vector **U** in the frequency domain can be calculated as

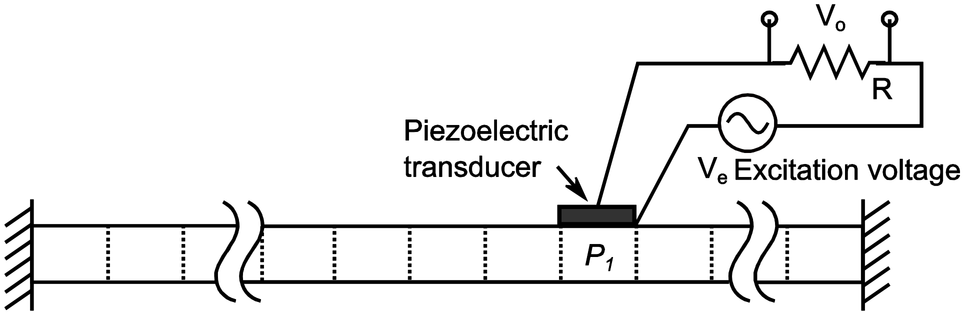

Figure 2.1. Illustration of an example beam structure with piezoelectric transducer for measuring piezoelectric impedance.

$$\mathbf{U} = \mathbf{S}^{-1}(\boldsymbol{\omega})\mathbf{F} \tag{2.6}$$

$$\mathbf{U} = [v_1, \theta_1, v_2, \theta_2, \cdots, v_{N+1}, \theta_{N+1}]^{\mathbf{T}} \tag{2.6a}$$

where $\mathbf{S}(\omega)$ is the dynamic stiffness matrix of the beam structure formulated by SEM, and v, θ are the transversal displacement and rotation angle at each node, respectively. The detailed derivation of $\mathbf{S}(\omega)$ can be found in [77]. The voltage V_p generated by the piezoelectric transducer due to the displacement field can be expressed as the following [87].

$$V_p = K_2 \boldsymbol{\Phi}_{\boldsymbol{p}} \mathbf{U} \tag{2.7}$$

$$K_2 = \frac{\boldsymbol{h_p h_b E_p d_{31}}}{\boldsymbol{2\varepsilon_{33}^T l_p}} \tag{2.7a}$$

where ε_{33}^T and l_p are the permittivity and length of the piezoelectric transducer. The piezoelectric admittance, inverse of the impedance, can be obtained as the following by measuring voltage drop V_o across the resistor [27,82].

$$Y(\omega) = \frac{1}{R}\frac{V_o}{V_e} \tag{2.8}$$

where the output voltage is

$$V_o = K_3(V_e + V_p) \tag{2.8a}$$

$$K_3 = \frac{i\omega R C_p}{1 + i\omega R C_p} \tag{2.8b}$$

Eventually, the piezoelectric admittance $Y(\omega)$ can be derived by substituting equations from (2.4) to (2.7) into Eq. (2.8).

$$Y(\omega) = \frac{1}{R} K_3 \left[K_1 K_2 \boldsymbol{\Phi}_{\boldsymbol{p}} \mathbf{S}^{-1}(\boldsymbol{\omega}) \boldsymbol{\Phi}_{\boldsymbol{p}}^{\mathbf{T}} + 1\right] \tag{2.9}$$

2.2.2. Mathematical Formulation of the Damage Identification Equation

Without loss of generality, in this research we assume that the structural damage is represented by the element bending stiffness reduction. Since these stiffness terms are nonlinearly nested in the dynamic stiffness matrix inverse $\hat{\mathbf{S}}^{-1}(\omega)$ of the damaged structure, Taylor series expansion is employed to explicitly determine the stiffness reduction induced by damage [85].

$$\hat{\mathbf{S}}^{-\mathbf{1}}(\omega) = \mathbf{S}^{-\mathbf{1}}(\omega) + \sum_{i=1}^{N} \left.\frac{\boldsymbol{\partial}\hat{\mathbf{S}}^{-\mathbf{1}}(\omega)}{\boldsymbol{\partial} d_i}\right|_{d_i=0} d_i \tag{2.10}$$

$$\begin{aligned}\left.\frac{\boldsymbol{\partial}\hat{\mathbf{S}}^{-\mathbf{1}}(\omega)}{\boldsymbol{\partial} d_i}\right|_{d_i=0} &= -\left.\hat{\mathbf{S}}^{-\mathbf{1}}(\omega)\frac{\boldsymbol{\partial}\hat{\mathbf{S}}(\boldsymbol{\omega})}{\boldsymbol{\partial d_i}}\hat{\mathbf{S}}^{-\mathbf{1}}(\omega)\right|_{\boldsymbol{d_i}=0} \\ &= -\mathbf{S}^{-\mathbf{1}}(\omega)\left[\mathbf{C}_{\boldsymbol{i}}^{\mathbf{T}}\frac{\boldsymbol{\partial}\hat{\mathbf{S}}_{ei}\,(\omega)}{\boldsymbol{\partial} d_i}\mathbf{C}_{\boldsymbol{i}}\right]\mathbf{S}^{-\mathbf{1}}(\omega) \\ &\approx \mathbf{S}^{-\mathbf{1}}(\omega)\left[\mathbf{C}_{\boldsymbol{i}}^{\mathbf{T}}\mathbf{K}_{\boldsymbol{ei}}\mathbf{C}_{\boldsymbol{i}}\right]\mathbf{S}^{-\mathbf{1}}(\omega)\end{aligned} \tag{2.10a}$$

where d_i is the stiffness reduction of the i-th element, and $\mathbf{C}_i$ is the connectivity matrix for assembling elemental matrices into global stiffness matrix. $\mathbf{K}_{ei}$ is the i-th elemental stiffness matrix formulated by FEM [88], which is used to approximate the partial derivative of the damaged stiffness matrix inverse $\hat{\mathbf{S}}^{-1}(\omega)$ [79]. Thus, the damage index d_i can be extracted from $\hat{\mathbf{S}}^{-1}(\omega)$ as in Eq. (2.10), and by substituting into (2.9), the piezoelectric admittance $\hat{Y}(\omega)$ of the damaged beam can be finalized as

$$\hat{Y}(\omega) = \frac{1}{R}K_3\left[K_1K_2\boldsymbol{\Phi_p}\left[\mathbf{S}^{-\mathbf{1}}(\omega) + \mathbf{S}^{-\mathbf{1}}(\omega)\left[\sum_{\boldsymbol{i}=\mathbf{1}}^{\boldsymbol{N}}\mathbf{C}_{\boldsymbol{i}}^{\mathbf{T}}\mathbf{K}_{\boldsymbol{ei}}\mathbf{C}_{\boldsymbol{i}}d_i\right]\mathbf{S}^{-\mathbf{1}}(\omega)\right]\boldsymbol{\Phi}_{\boldsymbol{p}}^{\mathbf{T}} + 1\right] \tag{2.11}$$

The difference of the undamaged and damaged piezoelectric admittance $\Delta\boldsymbol{Y}$ can be easily obtained from Eqs. (2.9) and (2.11), and after some derivations, the inverse equation that directly relates damage indices to the admittance difference can be formulated as the following.

$$\Delta \boldsymbol{Y} = \frac{1}{R} K_1 K_2 K_3 \boldsymbol{\Phi}_{\boldsymbol{p}} \left[\mathbf{S}^{-1}(\omega)\left[\sum_{i=1}^{N} \mathbf{C}_{\boldsymbol{i}}^{\mathbf{T}} \mathbf{K}_{\boldsymbol{ei}} \mathbf{C}_{\boldsymbol{i}} d_i\right]\mathbf{S}^{-1}(\omega)\right] \boldsymbol{\Phi}_{\boldsymbol{p}}^{\mathbf{T}}$$

$$= \mathbf{G} \times \mathbf{d} \tag{2.12}$$

$$\Delta \boldsymbol{Y} = \left[\hat{Y}(\omega_1), \hat{Y}(\omega_2), \dots, \hat{Y}(\omega_m)\right]^{\mathrm{T}} - \left[Y(\omega_1), Y(\omega_2), \dots, Y(\omega_m)\right]^{\mathrm{T}} \tag{2.12a}$$

$$\mathrm{G}_{ji} = \frac{1}{R} K_1 K_2 K_3 \boldsymbol{\Phi}_{\boldsymbol{p}} \left[\mathbf{S}^{-1}(\omega_j) \mathbf{C}_{\boldsymbol{i}}^{\mathbf{T}} \mathbf{K}_{\mathbf{e}\boldsymbol{i}} \mathbf{C}_{\boldsymbol{i}} \mathbf{S}^{-1}(\omega_j)\right] \boldsymbol{\Phi}_{\boldsymbol{p}}^{\mathbf{T}}$$

$$i=1,2,\dots,N \text{ and } j=1,2,\dots,m \tag{2.12b}$$

$$\mathbf{d} = [d_1, d_2, \dots, d_N]^{\mathrm{T}} \tag{2.12c}$$

where m is the number of admittance measurements of the integrated system. The location and severity of the damage can be identified by solving the damage index vector **d** in Eq. (2.12). However, this vector **d** cannot be uniquely obtained and become highly susceptible to noise when the sensitivity matrix **G** is rank-deficient. We can improve the ill-posedness of the inverse equation either by reducing the number of elements N in the model, or by increasing the number of admittance measurements m. The beauty of the SEM is that a very small number of elements are required for accurate analysis in high-frequency regime. An extreme example is that the spectrum dynamics of a homogenous beam structure can be accurately analyzed with only one spectral element [77]. However, sufficient numbers of elements are still essential to identify the damage's location with satisfactory resolution which is otherwise too coarse to pinpoint a specific location of the damage. On the other hand, since the damage effect is most significant around resonance peaks [23], we can fully take advantage of this feature by selecting a large number of measurement frequencies near the resonance. However, the information attained around the same resonance are similar to each other since they are represented by that same specific mode. Thus, simply increasing the number of measurements near each resonant frequency may not be a viable approach to enrich the measurement inputs of the Eq. (2.12).

2.2.3. Data Enrichment via Adaptive Piezoelectric Circuitry

The spectral element model of the piezoelectric impedance has mitigated the significantly ill-posed inverse equation when compared to the FEM approach. Yet, Eq. (2.12) still remains rank-deficient, which would result in erroneous damage identification especially when the system is subject to unavoidable error and noise. To address the concern, this section introduces a concept of adaptive piezoelectric circuitry implemented for impedance data enrichment. Jiang et al. [9,75,76] proposed the idea of incorporating adaptive piezoelectric circuitry into structures to increase the modal frequency measurements in the integrated system. By introducing a similar concept to the problem at hand, additional degrees of freedom can be introduced by the circuitry elements and the modified dynamics of the coupled system can be reflected in the piezoelectric impedance responses. An enriched data set of impedance measurements can thus be obtained by selectively tuning the inductance values in the circuitry, and this data set can be utilized to improve the underdetermined inverse problem to accurately predict the damage characteristics.

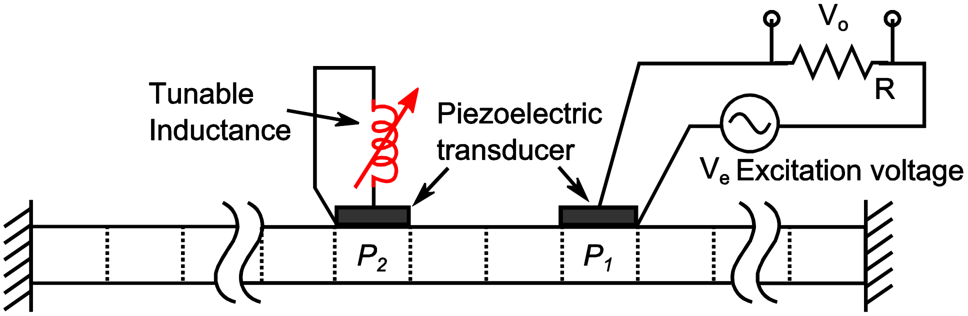

Figure 2.2. Illustration of the structure integrated with the adaptive piezoelectric circuitry.

Figure 2.2 presents the additional piezoelectric transducer with tunable inductance L implemented at the P_2-th element of the previous configuration shown in Figure 2.1. The displacement field $\mathbf{U}_{new}$ of the newly integrated system introduced by harmonic excitation voltage V_e generates voltage V_{p_2} at the additional piezoelectric transducer due to its direct piezoelectric effect.

$$V_{p_2} = K_2 \boldsymbol{\Phi}_{\boldsymbol{p_2}} \mathbf{U}_{\boldsymbol{new}} \tag{2.13}$$

$$\boldsymbol{\Phi}_{\boldsymbol{p_2}} = \left[(0,0)_{i=1}, (0,0)_{i=2}, \cdots, (0,1)_{i=P_2}, (0,-1)_{i=P_2+1}, \cdots, (0,0)_{i=N+1}\right] \tag{2.13a}$$

where $\boldsymbol{\Phi}_{p_2}$ indicates the location of the additional piezoelectric transducer. The moment M_{p_2} across this transducer can be calculated as

$$M_{\mathrm{P}_2} = K_{1A} V_{\mathrm{P}_2} \tag{2.14}$$

$$K_{1A} = \frac{b_p E_p d_{31}(\omega^2 L C_{p_2})}{2h_p(1-\omega^2 L C_{p_2})}\left[\left(\frac{1}{2}(h_p + h_b)\right)^2 - \left(\frac{1}{2}h_b\right)^2\right] \tag{2.14a}$$

where C_{p_2} is the capacitance of the additional piezoelectric transducer. Now, the generalized force vector in Eq. (2.5) is added by another term as the following

$$\mathbf{F} = M_p \boldsymbol{\Phi}_{\boldsymbol{p}}^{\mathbf{T}} + M_{p_2} \boldsymbol{\Phi}_{\boldsymbol{p_2}}^{\mathbf{T}} \tag{2.15}$$

We can solve the displacement vector $\mathbf{U}_{new}$ by substituting the Eqs. (2.13) – (2.15) into (2.6). After some derivation, the modified stiffness matrix $\mathbf{S}_{new}$ of the integrated system can be obtained as

$$\mathbf{S}_{\boldsymbol{new}} = \mathbf{S} - K_{1A} K_2 \boldsymbol{\Phi}_{\boldsymbol{p_2}}^{\mathbf{T}} \boldsymbol{\Phi}_{\boldsymbol{p_2}} \tag{2.16}$$

The inverse equation for the integrated system can be formulated by similar development in the previous section:

$$\Delta \boldsymbol{Y}_{\boldsymbol{new}} = \frac{1}{R} K_1 K_2 K_3 \boldsymbol{\Phi}_{\boldsymbol{p}} \left[\mathbf{S}_{\boldsymbol{new}}^{\mathbf{-1}}(\omega) \left[\sum_{\boldsymbol{i=1}}^{\boldsymbol{N}} \mathbf{C}_{\boldsymbol{i}}^{\mathrm{T}} \mathbf{K}_{\boldsymbol{ei}} \mathbf{C}_{\boldsymbol{i}} \boldsymbol{d}_{\boldsymbol{i}} \right] \mathbf{S}_{\boldsymbol{new}}^{\mathbf{-1}}(\omega) \right] \boldsymbol{\Phi}_{\boldsymbol{p}}^{\mathbf{T}}$$

$$= \mathbf{G}_{\boldsymbol{new}} \times \mathbf{d} \tag{2.17}$$

$$\Delta \boldsymbol{Y}_{\boldsymbol{new}}(\omega) = \widehat{\boldsymbol{Y}}_{\boldsymbol{new}}(\omega) - \boldsymbol{Y}_{\boldsymbol{new}}(\omega) \tag{2.17a}$$

$$\mathrm{G}_{new_{ji}} = \frac{1}{R} K_1 K_2 K_3 \boldsymbol{\Phi}_{\boldsymbol{p}} \left[\mathbf{S}_{new}^{-1}(\omega_j) \mathbf{C}_{\boldsymbol{i}}^{\mathbf{T}} \mathbf{K}_{\boldsymbol{ei}} \mathbf{C}_{\boldsymbol{i}} \mathbf{S}_{\boldsymbol{new}}^{-1}(\omega_j) \right] \boldsymbol{\Phi}_{\boldsymbol{p}}^{\mathbf{T}}$$

$$i=1,2,\ldots,N \text{ and } j=1,2,\ldots,m \tag{2.17b}$$

The dynamic characteristic of the integrated system can be easily altered by tuning the inductance value systematically, which enables to obtain different impedance responses from the same structural damage. When the inductance is tuned from L_1 to L_P, we can derive *P* different groups of altered inverse equations and augment them in the matrix form as following.

$$\Delta \boldsymbol{Y}_{sum} = \mathbf{G}_{sum} \times \mathbf{d} \tag{2.18}$$

$$\Delta \boldsymbol{Y}_{\boldsymbol{sum}} = \begin{Bmatrix} \Delta \boldsymbol{Y}_{new}(L_1) \\ \Delta \boldsymbol{Y}_{new}(L_2) \\ \vdots \\ \Delta \boldsymbol{Y}_{new}(L_P) \end{Bmatrix}, \mathbf{G}_{\boldsymbol{sum}} = \begin{bmatrix} \mathbf{G}_{new}(L_1) \\ \mathbf{G}_{\boldsymbol{new}}(L_2) \\ \vdots \\ \mathbf{G}_{\boldsymbol{new}}(L_P) \end{bmatrix} \tag{2.18a}$$

Eq. (2.18) and Figure 2.3 show the merit of applying adaptive piezoelectric circuitry. The original sensitivity matrix $\mathbf{G}_{new}$ has a dimension of *m* by *N*, where *m* is the number of impedance measurements and *N* is the number of elements in the SEM model.

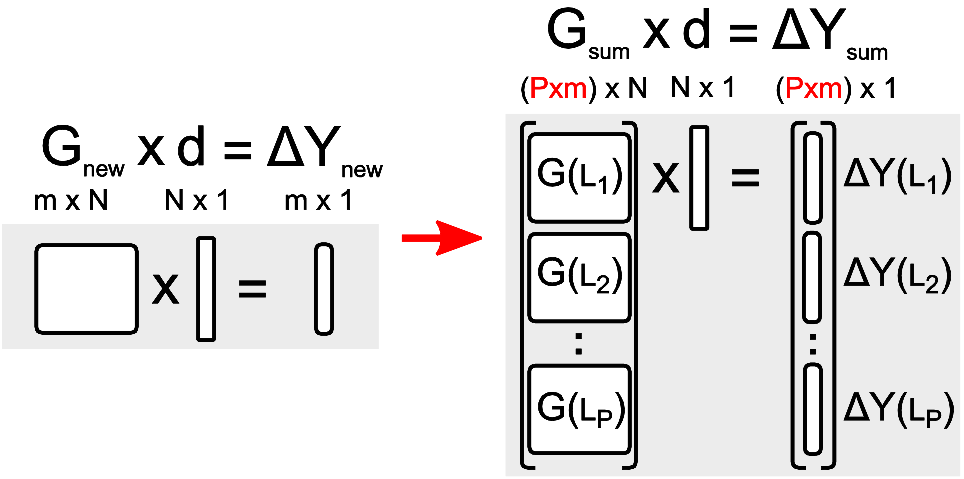

Figure 2.3. Schematic description of the idea of data enrichment to improve the rank-deficiency of the inverse equation.

As P different inductance values are applied to the circuitry, the number of impedance measurements and the sensitivity matrix can be greatly enriched up to $P \times m$, thus the original ill-posed inverse problem can be highly improved.

2.3. Numerical Analysis and Case Study

In this section, damage identification studies are conducted using a beam structure model integrated with adaptive piezoelectric circuitry to demonstrate the viability of the proposed approach for impedance data enrichment. The configuration of the illustrative system is given in Figure 2.2. A fixed-fixed beam is divided into 31 elements, and the piezoelectric transducers are integrated at the 3rd and 21st element. The dynamics of the integrated system is altered by tuning the inductance connected to the transducer at the 3rd element, and the other transducer is serially connected to a resistor for impedance measurement. Some relevant system parameters are listed in Table 2.1 In this analysis, Tikhonov regularization [86] is employed to solve the inverse problems. The regularization parameter α is obtained from the L-curve criterion that selects α to give the closest solution to the corner of the L-curve.

$$\mathbf{min}(\|\mathbf{G}\times\mathbf{d}-\boldsymbol{\Delta}\mathbf{Y}\|^2+\boldsymbol{\alpha}^2\|\mathbf{d}\|^2) \tag{2.19}$$

2.3.1. Identification of Single Damage under Noise

In the first case, the damage is assumed to be 10% stiffness reduction on the 13th element. Random noise of 62 dB signal-to-noise ratio (SNR) is introduced to the piezoelectric impedance response. Since the damage effect in the piezoelectric impedance becomes more significant near the resonance peaks, the impedance changes at 9 points around each resonance peak are utilized in the damage identification algorithm. Then, the inductances are selectively tuned to match the electrical resonance of the adaptive piezoelectric circuity to each structural resonance peak to alter the dynamic characteristics of the integrated system [9,75,76]. Eight inductance values selected for all resonant frequencies in the range of 5 kHz to 11 kHz are provided in Table 2.2.

Table 2.1. System parameters.

Beam structure		**Piezoelectric material**	
Length × Thickness × Width, mm	607.8 × 7.62 × 3.175	**Length × Thickness × Width, mm**	17 × 7.62 × 0.191
Young's modulus, GPa	73.4	**Young's modulus, GPa**	66
Density, $\mathbf{kg/m^3}$	2780	**Density, $\mathbf{kg/m^3}$**	7800
Loss factor, %	0.15	**Permittivity, ε_{33}^{T} , F/m**	1.6× 10^{-8}
Poisson's ratio	0.33	**Piezoelectric constant, $\mathbf{d_{31}}$, m/V**	-190× 10^{-12}

An illustrative example of the piezoelectric impedance responses with different inductance tunings is shown in Figure 2.4(a). As can be seen from the figure, the piezoelectric impedance of the integrated system can be easily modified by tuning the inductance to different values. As we utilize these tuned impedance measurements in the form of Eq. (2.18), the total number of piezoelectric impedance data set used for damage identification can be enriched by 8 times in this case study. A comparison of the damage prediction results with and without this impedance data enrichment is provided in Figure 2.4(b). The horizontal axis is the element number and the damage index, stiffness reduction of the element is provided along the vertical axis. The dotted line shows the actual damage distribution: 10% stiffness loss at the 13th element. It can be observed that the prediction using traditional method without data enrichment cannot accurately identify damage characteristics due to its severely ill-posed inverse equation, even when a low level of noise (62 dB SNR) is included in the simulation. However, when the proposed method of impedance data enrichment is applied, the damage identification result indicates approximately 10% stiffness reduction at the 13th element. The root mean square deviation (RMSD) between the predicted stiffness loss $\mathbf{d}$ and the actual damage $\mathbf{d}^0$ is employed as a metric to quantify the prediction error and compare the performance of damage identification.

Table 2.2. Inductance values selected for each resonance peak.

Resonant frequency, kHz	5.39	6.05	6.75	7.49	8.26	9.06	9.91	10.79
Inductance, mH	134.6	106.4	85.1	68.9	56.4	46.6	38.8	32.6

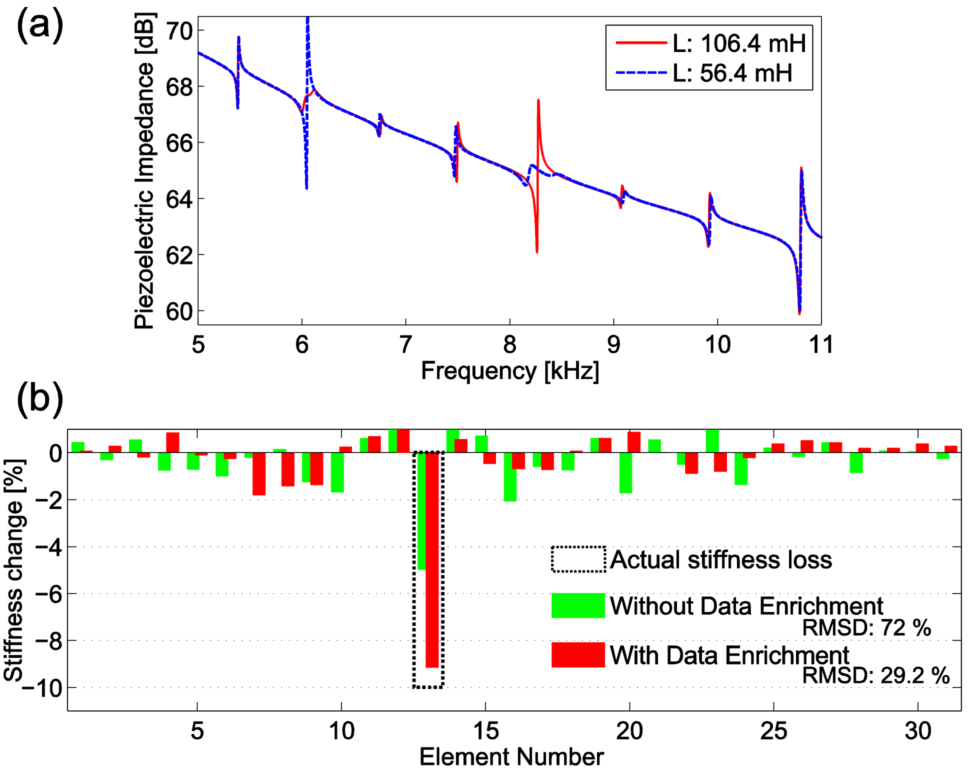

Figure 2.4. (a) Piezoelectric impedance responses of the integrated system for different inductance values (b) Identification of damage on the 13th element of the example beam structure with 10% stiffness reduction.

$$\mathrm{RMSD} = \sqrt{\frac{\sum_{i=1}^{N}\left(d_i - d_i^0\right)^2}{\sum_{i=1}^{N} {d_i^0}^2}} \tag{2.20}$$

where d_i, d_i^0 are the predicted and actual damage indices of the i-th element, respectively. When the piezoelectric impedance data is enhanced by the adaptive circuitry, RMSD is reduced from 72 % to 29.2 %.

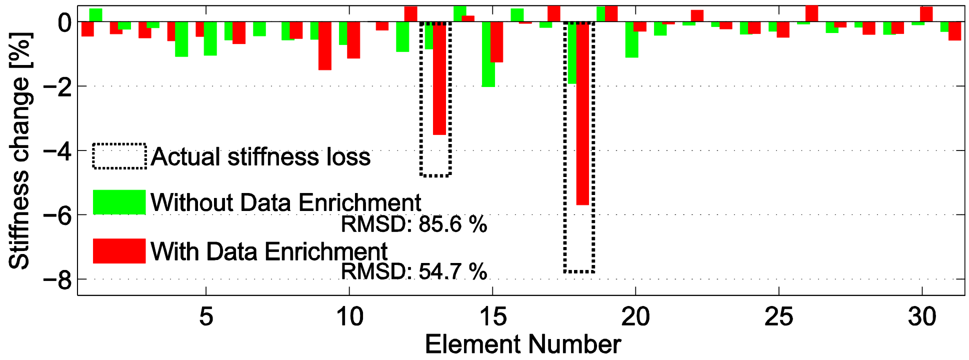

Figure 2.5. Multiple damage identification on the 13th, 18th elements of the beam with 5%, 8% stiffness reduction, respectively.

2.3.2. Identification of Multiple Damages under Noise

This section presents an example of damage identification when multiple damages are simulated in the beam structure. The structural damages are assumed to be 5% and 8% stiffness reductions at the 13th and 18th elements, respectively. In this case, higher level of noise (36 dB SNR) is applied in the impedance response. The damage prediction result is plotted in Figure 2.5. When the traditional method without data enrichment is applied, the damaged elements are virtually indistinguishable, and the largest two damages are falsely predicted on the 15th and 18th elements indicating approximately 2% stiffness reductions. However, as the impedance data is enriched, both damage indices at the 13th and 18th elements clearly indicate the simulated damages in the structure. The damage identified by using the traditional method has 85.6 % of RMSD error, whereas the prediction error obtained from the proposed approach reduced to RMSD of 54.7 %.

2.3.3. Investigation of Noise Influence on Damage Identification

This section investigates the influence of random noise ranging from 62 dB to 36 dB SNR on the single damage prediction results. Figure 2.6(a) shows the corresponding damage identification results, and a comparison of the prediction error (RMSD) is followed in Figure 2.6(b). Figure 2.6(a) presents that damage identification results of both methods deteriorate when noise level increases. However, although the noise level is increased by 26 dB, we can still observe that the proposed approach using inductance tuning predicts both location and severity of the damage more accurately than the conventional method. We can also clearly observe from Figure 2.6(b) that the damage prediction errors decrease for all 3 different noise levels when the proposed method is applied. Moreover, the damage prediction error for the noise case of 36 dB SNR with inductance tuning circuitry is much less than the error obtained from the traditional method even for the lowest level of noise (62 dB SNR). From these results, it can be concluded that the proposed method with adaptive piezoelectric circuitry for data enrichment significantly improves the accuracy in damage identification especially when noise is included in the impedance responses.

2.3.4. Investigation of the Influence of Modeling Errors on Damage Identification

In this section, modelling errors are considered in the inverse problem to evaluate their effect on the final damage prediction results. Here, measurement noise is not considered to explicitly focus on the modelling error. The inverse equation is given as the following

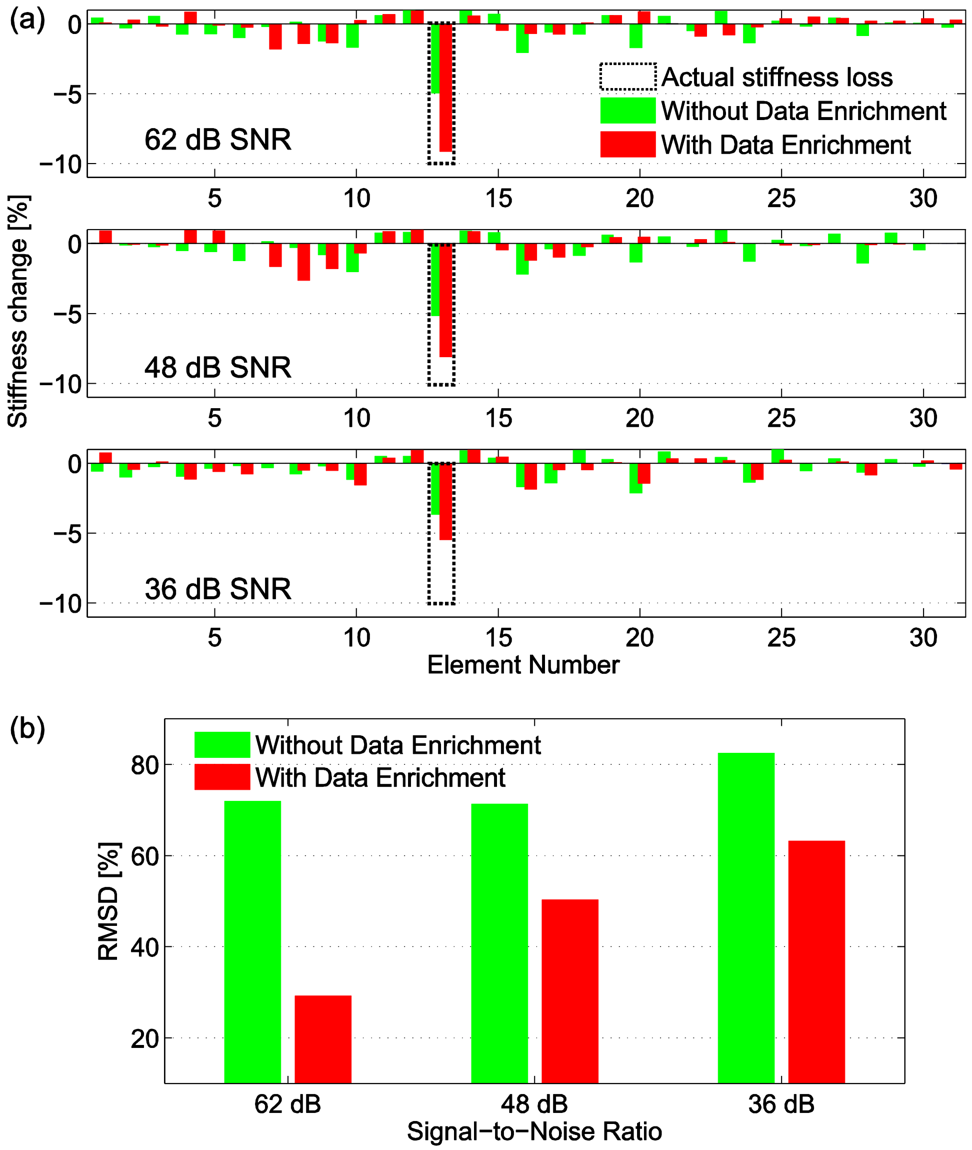

Figure 2.6. (a) Damage identification comparison with varying degrees of noise. (b) Damage prediction error (RMSD).

$$\mathbf{G}_{\mathrm{tr}} \times \mathbf{d}_{\mathrm{tr}} = \boldsymbol{\Delta}\mathbf{Y}_{\mathrm{tr}} \tag{2.21}$$

where we assume $\mathbf{G}_{\mathrm{tr}}$ is the true model without any modelling error and $\boldsymbol{\Delta}\mathbf{Y}_{\mathrm{tr}}$ is the true measurement when true damage $\mathbf{d}_{\mathrm{tr}}$ is occurred. Now we introduce a model $\mathbf{G}^{*}$ that has errors, and this results in $\boldsymbol{\Delta}\mathbf{Y}^{*}$ when true damage $\mathbf{d}_{\mathrm{tr}}$ is introduced in the model.

$$\mathbf{G}^{*} \times \mathbf{d}_{\mathrm{tr}} = \boldsymbol{\Delta}\mathbf{Y}^{*} \tag{2.22}$$

There is difference between the true measurement $\mathbf{\Delta Y}_{\mathrm{tr}}$ and $\mathbf{\Delta Y}^*$ which is denoted as $\mathbf{\Delta Y}_{\mathrm{err}}$.

$$\mathbf{\Delta Y_{err}} = \mathbf{\Delta Y_{tr}} - \mathbf{\Delta Y}^* \tag{2.23}$$

Now, when we predict the damage $\hat{\mathbf{d}}$ by solving the inverse equation, what we have at hand are the model $\mathbf{G}^*$ which is designed to approximate the true system and the true measurement $\mathbf{\Delta Y}_{\mathrm{tr}}$.

$$\mathbf{G}^* \times \hat{\mathbf{d}} = \mathbf{\Delta Y_{tr}} \tag{2.24}$$

When we substitute Eq. (2.23) into (2.24), the measurement difference $\mathbf{\Delta Y}_{\mathrm{err}}$ now can be considered as measurement noise with respect to $\mathbf{\Delta Y}^*$ as in Eq. (2.25).

$$\mathbf{G}^* \times \hat{\mathbf{d}} = \mathbf{\Delta Y}^* + \mathbf{\Delta Y_{err}} \tag{2.25}$$

By substituting Eq. (2.22) into (2.25) and solving the inverse equation, the damage prediction $\widehat{\mathbf{d}}$ becomes the sum of true damage $\mathbf{d}_{\mathrm{tr}}$ and the term induced by modelling error.

$$\begin{aligned} \widehat{\mathbf{d}} &= \mathbf{G}^{*^{-1}}(\mathbf{\Delta Y}^* + \mathbf{\Delta Y_{err}}) \\ &= \mathbf{d_{tr}} + \mathbf{G}^{*^{-1}}\mathbf{\Delta Y_{err}} \end{aligned} \tag{2.26}$$

The detrimental effect of measurement noise on damage prediction, especially when the inverse equation is ill-posed, is explained in the previous Section 2.1, and it is shown that the accuracy of damage identification under measurement noise can be greatly improved by incorporating well designed adaptive piezoelectric circuitry. Therefore, the adverse effect of modelling error, which is analogous to measurement noise, can be surmounted similarly by employing the suggested approach for data enhancement.

$$\begin{bmatrix} \mathbf{G}^{*}(L_1) \\ \mathbf{G}^{*}(L_2) \\ \vdots \\ \mathbf{G}^{*}(L_\mathrm{P}) \end{bmatrix} \times \hat{\mathbf{d}} = \begin{Bmatrix} \Delta\mathbf{Y}_{\mathbf{tr}}(L_1) \\ \Delta\mathbf{Y}_{\mathbf{tr}}(L_2) \\ \vdots \\ \Delta\mathbf{Y}_{\mathbf{tr}}(L_\mathrm{P}) \end{Bmatrix} \tag{2.27}$$

Figure 2.7 shows the numerical examples of the damage prediction when modelling errors are introduced. A case of 10% estimation error in the inductances is given in Figure 2.7(a), and Figure 2.7(b) shows the results when beam stiffness (73.4 GPa) is incorrectly estimated by 0.1 GPa. The horizontal axis is the element number and the vertical axis shows the stiffness reduction of each element. The dotted line indicates the actual damage distribution: 10% stiffness loss at the 13th element. It can be observed that the prediction using traditional method without data enrichment cannot accurately

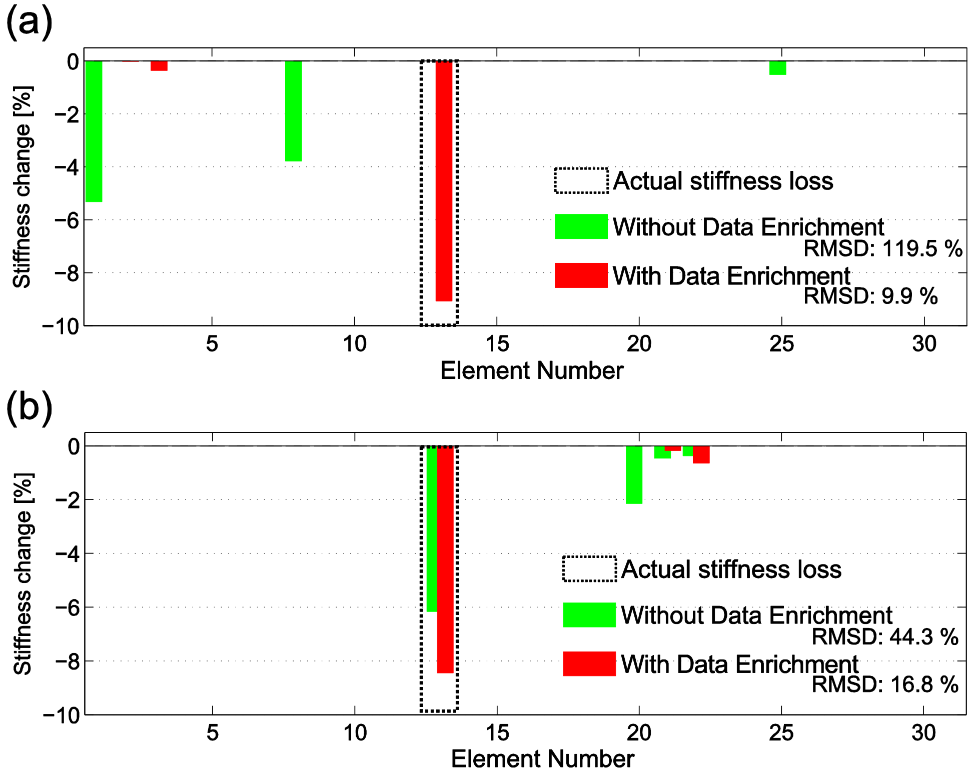

Figure 2.7. Comparison of damage prediction results when there exists (a) 10% modelling error in inductances, (b) 0.1 GPa modelling error in the beam stiffness.

identify damage characteristics in both cases. However, when the proposed method of data enrichment is applied, both of the damage predictions are significantly improved. The RMSD errors are reduced from 119.5 %, 44.3 % to 9.9 % and 16.8 %, respectively. From these results, it can be concluded that the proposed method for data enrichment can improve the accuracy in damage identification when the model includes estimation errors.

2.3.5. On the Number of inductance Tunings

This section investigates how the number of inductance tunings for data enrichment influences the damage identification performance. Singular value decomposition (SVD) is performed to evaluate the condition of the augmented sensitivity matrix as the number of inductance tunings is increased. The inductance values are first tuned to match the electrical resonance of the adaptive piezoelectric circuitry with each structural resonance in the interested frequency range of the host structure by following the procedure of Jiang et al [75]. The next tuning values are deviated ± 1% from the previously selected inductances for resonances, and then ± 2%, and so on. A case study is performed at the frequency range of 5 kHz to 11 kHz, which contains 8 resonance frequencies, and here we increased the number of inductance tunings to 20. The inductance tuning values used

Table 2.3. Inductance tuning values used for data enrichment.

Number	**1**	**2**	**3**	**4**	**5**	**6**	**7**	**8**	**9**	**10**
Inductance, mH	134.6	106.4	85.1	68.9	56.4	46.6	38.8	32.6	135.9	107.5
Number	**11**	**12**	**13**	**14**	**15**	**16**	**17**	**18**	**19**	**20**
Inductance, mH	86.0	69.6	57.0	47.1	39.2	32.9	133.3	105.3	84.2	68.2

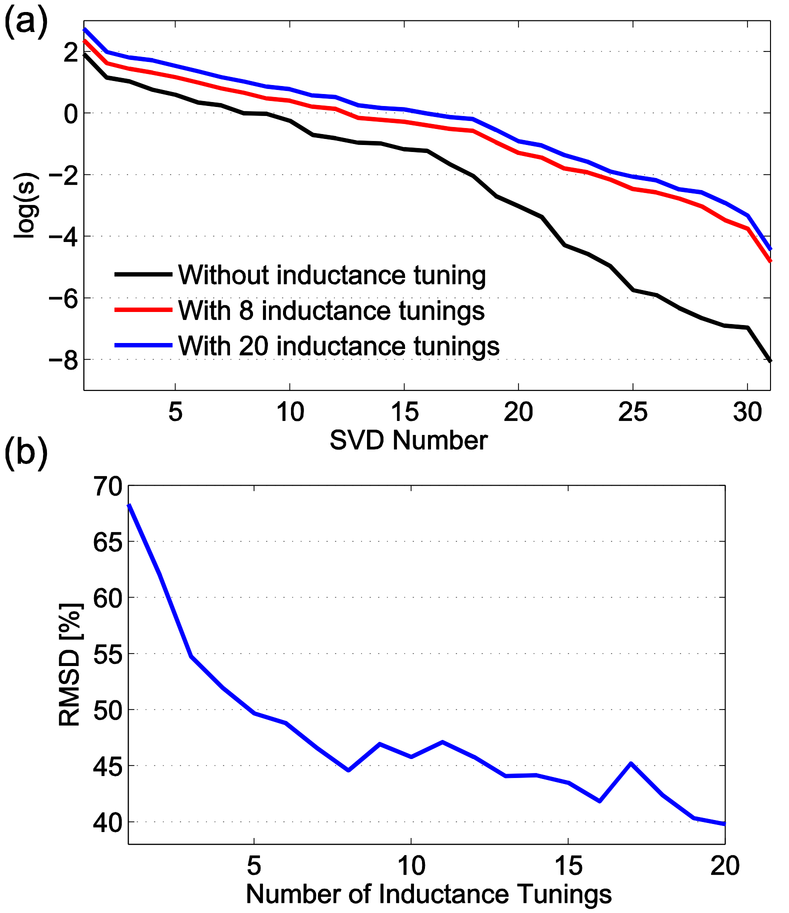

Figure 2.8. (a) Singular values of the augmented sensitivity matrix when different numbers of inductance tunings are employed (b) Damage prediction error (RMSD) with respect to the number of inductance tunings.

in this case study are listed in Table 2.3.

Figure 2.8(a) shows the logarithm of the singular values of the augmented sensitivity matrix $\mathbf{G}_{sum}$ in Eq. (2.18). As can be seen from the figure, the singular values are notably increased overall as 8 inductance tunings are employed for impedance data enrichment, and these values are even more increased when the number of inductance tunings is increased to 20. This implies that the ill-posed sensitivity matrix can be improved as more inductance tunings are applied for data enrichment. As a result, the damage prediction error (RMSD) decreases when the number of inductance tunings increases as displayed in Figure 2.8(b). Here, we can notice from Figure 2.8(b) that the damage identification error dramatically decreases for the first several inductance tunings, and then decreases gradually afterwards.

We considered other cases with 4 resonances in the frequency range from 8 kHz to 11 kHz, and 12 resonances in the range of 4 kHz to 13 kHz to investigate whether the damage prediction errors decrease similarly in other frequency ranges. All three case studies with different frequency ranges are repeated 5 times, and the average damage prediction errors for each case are compared in Figure 2.9. As can be observed from the

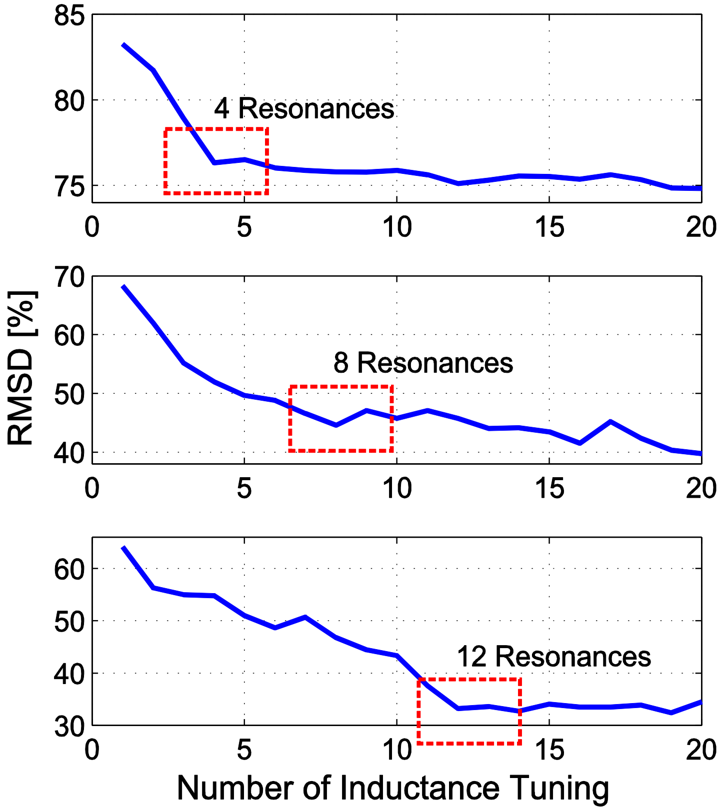

Figure 2.9. Damage prediction error (RMSD) comparison for frequency ranges with different number of resonances.

highlighted boxes in the figure, the RMSD starts to decrease gradually from near the 4th, 8th, and 12th inductance tuning augmentation when there are 4, 8, and 12 resonances in the interested frequency ranges, respectively. These results show that there appears to be a relation between the number of inductance tunings and the number of resonances employed for damage identification. This can be explained by looking into how the inductance values are selected, and how they affect the inverse equation for damage identification from the case study of 8 resonances as an example.

As described previously, the first 8 inductance values are tuned to each resonance, and then the next inductance values are varied from these. When the inductances are tuned for each resonant frequency, the piezoelectric impedances of the integrated system are altered distinctively from each other as shown in Figure 2.4(a). Formulating these responses in the form of Eq. (2.18), we can fully exploit the merit of the proposed data enrichment concept by augmenting unique and independent information into the sensitivity matrix. Therefore, the rank-deficiency of the inverse equation can be highly improved, which results in significant decrease of the damage identification error. On the other hand, the next following inductances are variations of the first group of 8 inductances tuned for resonances, thus the corresponding impedance responses are similar to the first group of impedance responses as well. These impedance responses add analogous information into the augmented sensitivity matrix, and thus the rank-deficiency of the matrix can be improved gradually. For this reason, the damage identification error decrease gradually near after 8th inductance tunings for data enrichment. From these results, it can be concluded that the more inductance tunings are applied, the more accurate damage identification can be achieved by improving the rank-deficiency of the sensitivity matrix. On the other hand, to exploit the benefit of data enrichment efficiently, the damage identification algorithm can be performed with the inductances tuned once for each resonance in the interested frequency range.

2.4. Experimental Validation

In this section, an experimental study is performed to validate the proposed method of data enrichment. A fixed-fixed aluminum beam (Al-2024) is discretized into 61 elements, and two piezoelectric transducers (PSI-5A4E) are bonded on the top surface of the 29th and 41st elements for inductance tuning and impedance measurement purposes, respectively. For the damaged case, we introduced damage as a surface notch at the 25th element of the beam structure. The notch is 0.09 mm deep (2.8% of the beam thickness) and 10.4 mm long having same width of the beam, which results in 8.3% reduction of the local bending stiffness [78].

Table 2.4. Parameters of the tunable inductor, and dimensions of the beam and piezoelectric transducers.

Beam, mm	627.2 × 7.21 × 3.175		**P_1, mm**	16.85 × 7.09 × 0.191		**P_2, mm**	16.3 × 7.09 × 0.191	
Circuitry element	C_1 ,nF	C_2, nF	R_2, Ω	R_3, Ω	R_4, Ω	R_5, Ω	R_6, Ω	R_7, Ω
	9.788	9.807	4620	4629	4629	4628	4632	4629
	L, mH	39.45	40.367	41.272	45.32	46.16	63.1	80.12
	R_1, Ω	850	870	890	980	1000	1371	1750

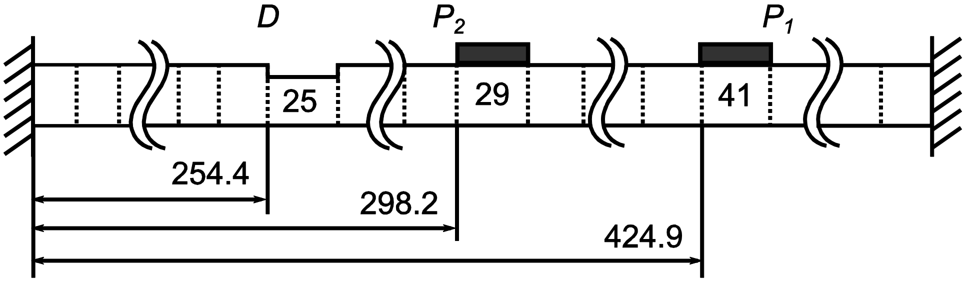

Figure 2.10. Configuration of the experimental beam structure (measures in millimeters).

Figure 2.10 presents the experimental configuration including the location of the piezoelectric transducers and damage. The tunable inductor [89] used in this study is shown in Figure 2.11(a), which is realized by using op-amps (LM324), resistors, and capacitors. As can be seen in Figure 2.11(b), the tunable inductor exhibits frequency dependent property; the variation is approximately 20% of the inductance steps for data enrichment. This frequency dependent property is considered in the baseline model. Seven inductance tunings are employed for data enrichment, and the relevant parameters are provided in Table 2.4. In order to minimize the modeling errors stemming from the measurement of the beam dimensions and material properties, the baseline model was tailored by modifying the length and mechanical loss factor of the beam, and the location of the piezoelectric transducers. Figure 2.11(c) compares the impedance responses of the baseline model and the experiment. The measurement noise is 42 dB SNR, however considering the uncertainty in the baseline model, the total noise level can increase. In this analysis, the damage indices were solved by employing least-square algorithms with negative constraints. We restricted to have negative coefficients since we assumed damage as stiffness reduction and designed damage as surface notch in the experiment.

Figure 2.12 presents the corresponding damage prediction result, and the damage identification errors with respect to the number of inductance tunings. When the traditional method without data enrichment is employed for damage identification, the result indicates false location at the 22nd element with 4.3 % stiffness reduction. Since the damaged locations may not be known in advance for real applications, and the structural health monitoring system may not be able to distinguish erroneous results, the incorrect predictions would mislead the subsequent decisions for remedy. However, as the

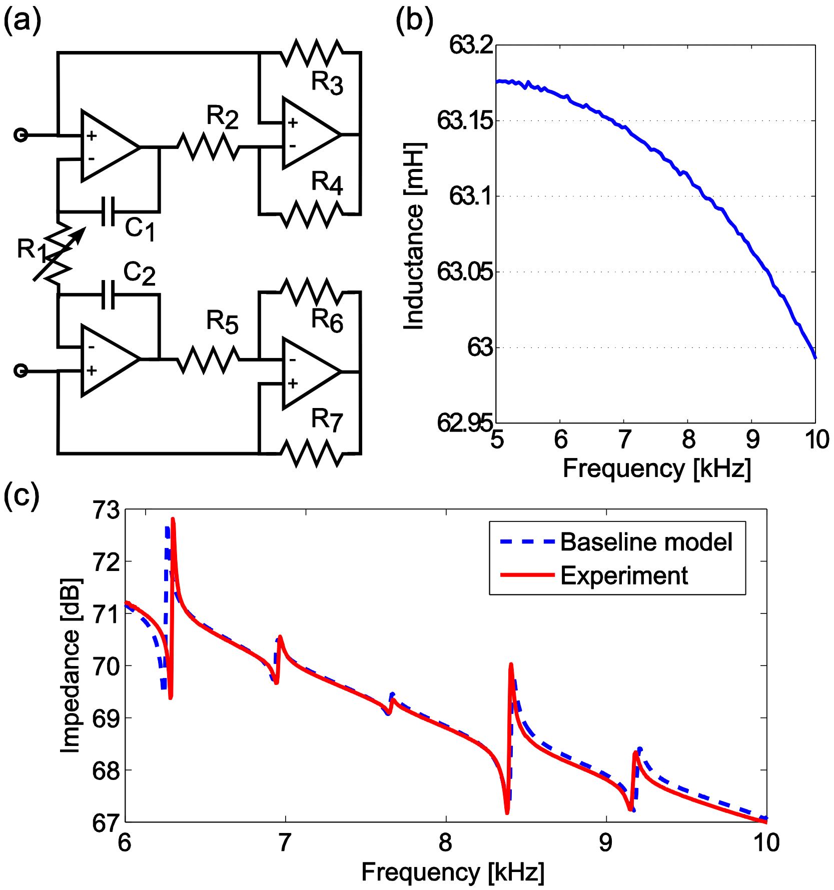

Figure 2.11. (a) Schematic illustration of floating synthetic inductor (b) An example measurement of frequency dependent inductance of the tunable inductor (c) Comparison of the piezoelectric impedance responses of the baseline model and the experiment result

inductance tunings are applied, the damage prediction error gradually decreased, and the final result correctly identified the damage at the 25th element with predicted stiffness loss (6.8%) close to the actual 8.3% value. From these experimental results, it is verified that the proposed concept of data enrichment can indeed improve the damage identification accuracy effectively.

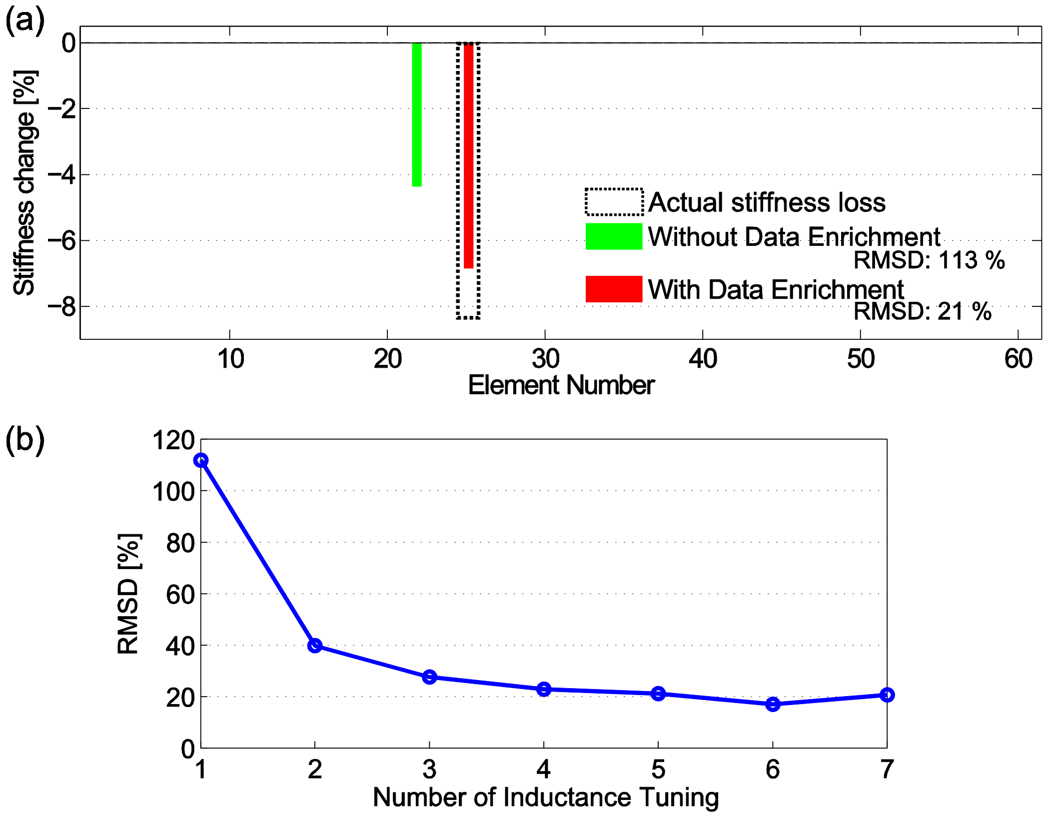

Figure 2.12. (a) Experimental damage identification on the 25th element of the beam structure (b) Damage prediction error (RMSD) with respect to the number of inductance tunings.

2.5. Summary and Conclusion

This chapter shows that the piezoelectric impedance model-based SHM method can be remarkably enhanced by incorporating well designed adaptive piezoelectric circuitry. As the circuitry inductance values are tuned, the dynamics of the integrated system is altered, which enables an increased measurement data set of piezoelectric impedance. This method improves the condition of the otherwise severely ill-posed inverse problem, and can significantly improve the accuracy of the impedance-based structural damage identification, especially when the system is subject to unavoidable measurement noise and modelling error. The proposed concept is numerically implemented on a beam structure showing significantly improved accuracy in damage predictions. The influence of data enrichment on the damage identification performance is analyzed, and guideline is presented for the selection of tuning inductances. Experimental investigations are also performed, which clearly verified the effectiveness of the proposed approach.

CHAPTER 3

Preliminary Study on Damage Identification with Integrated Bistable and Adaptive Piezoelectric Circuitry

3.1. Introduction

While the piezoelectric impedance-model based SHM techniques has shown great success in identifying the damage characteristics, the current state of the art has two notable limitations for reliable implementation as stated in Chapter 1. The limitation of rank-deficiency is addressed in Chapter 2 by impedance data enhancement capitalizing on adaptive piezoelectric circuity. However, the other concern in accurate measurement of the damage-induced impedance variations under environmental noise and system damping still needs to be addressed. When measurement error is combined with the rank-deficiency of inverse problem, damage prediction error can become adversely amplified [90]. To overcome this shortcoming, sensitivity enhancing control techniques have been investigated [90–92] in the vibration-based damage detection research to increase the damage-induced resonance frequency shifts. The approaches manipulate closed-loop eigenvalues and -vectors by integrating active feedback control with the structure such that structural response changes due to damage are enhanced. Although these studies have shown promising ability to address the issue, the sensitivity enhancing control concepts typically require multiple transducers for implementation in addition to being cumbersome due to the active implementation.

This chapter aims to develop a measurement technique that is robust to noise and damping influences but still easy to implement without active feedback controls. To exemplify the effectiveness of the proposed measurement technique, this chapter conducts damage interrogation in relatively low frequency range by detecting the damage-induced resonance frequency shifts [9]. Since the sensitivity of frequency shifts due to damage effects becomes low, generally less than 1 Hz, in low frequency range, even minute measurement error can be critical to the final damage identification performance. In conjunction with the prior adaptive piezoelectric circuitry presented in Chapter 2, this chapter investigates a new means for structural damage identification which is found to be notably robust when response signals are distorted due to realistic noise and damping. Although accurate determination of the damage-induced impedance variation is the principal aim of the proposed alternative approach, this chapter provides additional focus on the final damage identification as an unambiguous metric of success because reducing measurement error may not equally correlate to the improvement of damage identification.

3.2. Bifurcation-Based (BB) Detection of Frequency Shifts

3.2.1. Bifurcation-Based Sensing

Direct peak detection (DPD) is a straightforward means to extract resonant frequency shifts due to structural changes. However, the frequency shifts may be difficult or impossible to accurately determine by conventional approaches since peaks are distorted due to inevitable noise and damping in real applications. As will be shown, even mild damping and low level noise can lead to significant error for damage identification if employing DPD for determination of frequency shifts. To surmount these concerns, an alternative approach for frequency shift detection is developed based upon bifurcation phenomena associated with strongly nonlinear dynamic systems. The term bifurcation denotes a sudden qualitative change of response in consequence to infinitesimal parameter change. In fundamental physics studies, bifurcations have been utilized in the Josephson bifurcation amplifier to detect otherwise imperceptible shifts in current level [93,94]. In microscale mass sensing, change in resonance frequency of MEMS is tracked by activating bifurcations of the sensors in consequence to minute adsorption of the target analyte mass [95–98]. Studies in the context of MEMS mass sensing have shown that frequency shift-tracking using bifurcations is much less susceptible to deteriorating performance due to measurement noise and damping than traditional DPD [95]. This is because change in environmental damping may be rectified in a bifurcation-based sensing method by adjustment of the excitation amplitude which does not similarly alleviate accuracy concerns for DPD, particularly on the microscale [95]. The comparable objectives of this work, albeit on much larger scales, encourage the present adoption of bifurcations for SHM applications. However, a notable distinction between micro- and macroscale structures makes direct implementation of bifurcations for structural sensing a challenge: the existence of strong nonlinearity.

Nonlinear responses for microscale sensors are common due to geometry and material effects, even before higher excitation levels drive the structures to nonlinear regimes [99]. In contrast, it is often unfavorable for larger-scale mechanical or civil structures that are monitored for damage to undergo strongly nonlinear behaviors. As a result, other means must be introduced to harness bifurcations on larger structural scales.

Recently, Lim and Epureanu [100–102] pioneered the application of bifurcation phenomena for sensing in macroscale structures by introducing the strong nonlinearity via nonlinear feedback control. By forecasting the bifurcation point, which enables to maintain the structural system in the safe pre-bifurcation regime, it has been shown that tracking the bifurcation points provides an order of magnitude higher sensitivity of detecting mass changes in a cantilever-based sensor compared to the conventional resonance frequency shift detection approach. Harne and Wang [103] explored an integration of the monitored structure with piezoelectric transducer and bistable circuitry. The composite system enabled the detection of structural change (mass addition) due to activation of circuitry bifurcations. As compared to the monitored structural system exhibiting strongly nonlinear behaviors, the bifurcations used for change detection are strictly a matter of the strongly nonlinear bistable circuitry which has negligible back-coupling to the host structure response. Observing the utility of the structure and bistable circuit integration in Ref. [103], this chapter adopts a similar configuration in tandem with the adaptive piezoelectric circuitry to track the structural frequency shifts induced due to damage. By utilizing the piezoelectric admittance response measured from the piezoelectric transducer with the adaptive circuitry approach as the input voltage for the bistable circuit, the host structural spectral change induced by damage can be assessed by the activation of circuitry bifurcations. Thus, the proposed sensing framework introduces the required strong nonlinearity via the attachment or inclusion of bistable circuitry into the damage detection process. Therefore, this chapter investigates the viability of the system integration and its robustness and accuracy in the presence of realistic noise and damping as compared to traditional peak detection approaches.

3.2.2. Overview of Bifurcation-Based Frequency Shift Measurement Procedure

This section describes a procedure to monitor frequency shifts when utilizing bistable circuitry bifurcations. Figure 3.1 shows the bistable circuit employed in this study and the essential components of the structural integration: host structure to be

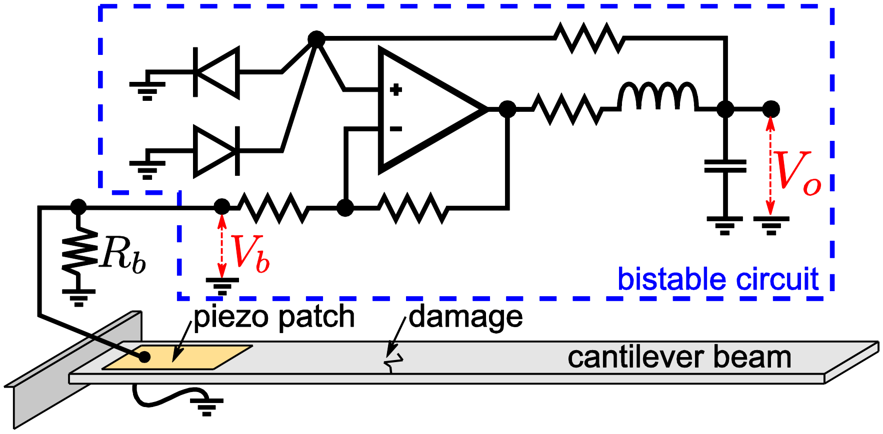

Figure 3.1. Schematic of excited host structure to be monitored (here, a cantilever beam) with piezoelectric transducer and attached bistable circuitry.

monitored, piezoelectric transducer, and electrical connection from the transducer to measure piezoelectric impedance and serve as input voltage V_b for the bistable circuit having output voltage V_o.

For low input voltage level, the bistable circuit undergoes small amplitude,

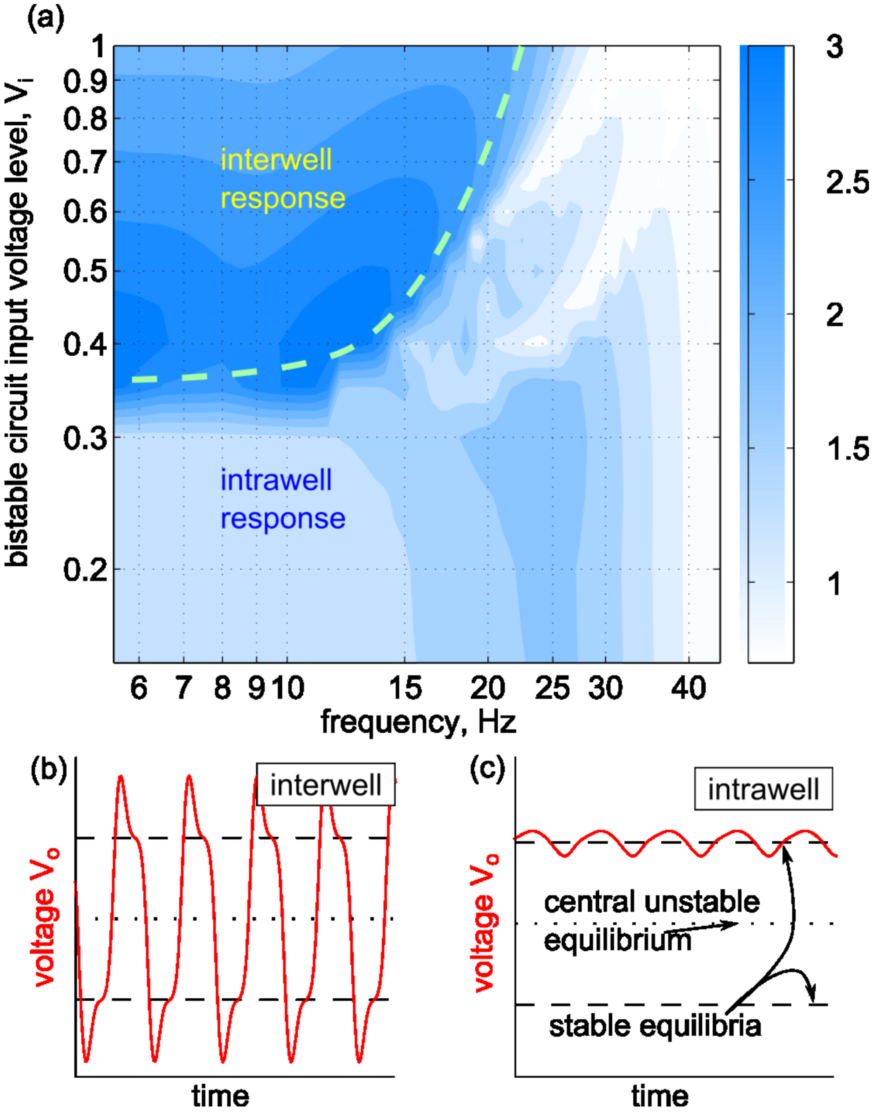

Figure 3.2. (a) Experimental bistable circuit output-to-input voltage frequency response function magnitude, as function of excitation frequency and level, as adapted and re-plotted from [103]**. The dashed line on the contour approximately demarcates the threshold between intra- or interwell responses. Example experimental voltage time series for (b) interwell and (c) intrawell dynamics.**

intrawell oscillations of output level; whereas higher input levels may trigger energetic, interwell oscillations. Figure 3.2(a) plots an experimental contour of bistable circuit output-to-input voltage FRF magnitude as function of excitation frequency and level, as adapted and re-plotted from [103]. For constant harmonic excitation frequency, an increasing input voltage level may activate the bifurcation leading to dramatic change in output response level, from intra- to interwell response, or vice versa. The quantitative and qualitative differences between typical measured intra- to interwell circuit output voltage responses are shown in Figure 3.2(b,c). An approximate demarcation boundary between the two steady-state response regimes is denoted in Figure 3.2(a) by the light dashed curve. By tuning bistable circuit component values, the frequency sensitivity of the sudden change in circuit output voltage amplitude can be designed to target a specific structural mode. In Figure 3.2(a), the sensitive region is located around excitation frequencies 7 to 10 Hz, where small changes in input voltage level around 0.34 V activate a saddle-node bifurcation in output voltage level. It is this region of sensitive bistable circuit response that is exploited in the proposed sensing scheme.

Through the strategic integration of the structure and bistable circuitry, the structural responses effectively become the input voltage level to the circuit, following a coupling provided by the transducer and a gain adjustment provided by a tuning resistance R_b. Thus, amplified structural response leads to amplified input voltage level for the circuit. This trend is exploited to detect and measure frequency shifts in resonance peaks using the overall procedure illustrated in Figure. 4.3. The piezoelectric admittance before and after damage, measured via the piezoelectric transducer, are used as discrete input to the bistable circuit following adjustment of gain and frequency sensitivity. The tuning resistance R_b linearly adjusts the amplitude of the piezoelectric admittance measurements from the piezoelectric transducer such that an activation threshold is aligned with an intermediate amplitude of the resonance, and sets this level to be the critical level that may activate the bistable circuit bifurcations. In Figure 3.2(a), this critical level is seen to be approximately 0.34 V, and in Figure 3.3(a) the resonance peak amplitude has been adjusted by tuning the gain such that a portion of the peak is above this critical input voltage level. The frequency sensitivity is adjusted such that the favorable threshold bandwidth is shifted to occur around the structural mode being monitored (i.e., shifting the comparable bandwidth of 7-10 Hz in Figure 3.2(a) to the bandwidth around the resonance of interest).

Then, the corresponding voltage level for each frequency after the gain adjustment is utilized as input signal to the bistable circuit. The structure is harmonically excited at a single frequency and the response from the piezoelectric transducer is directly fed to the bistable circuit following gain adjustment; such direct integration of the electrical and mechanical domains is that depicted in Figure 3.1. The steady-state circuit output voltage response is then evaluated for whether it obtained intra- or interwell oscillations, as illustrated by comparable intra- and interwell responses of the bistable circuit shown in Figure 3.2(b,c). Repeating this process across the spectrum containing the resonance frequency yields two bifurcations in response: one up and one down in circuit output voltage level. Repeating this process again for the damaged structural responses yields two more bifurcations at certain frequencies. Figure 3.3(b) presents example output results from this overall procedure indicating that over certain bandwidths the interwell responses are activated whereas across other frequencies the intrawell responses were

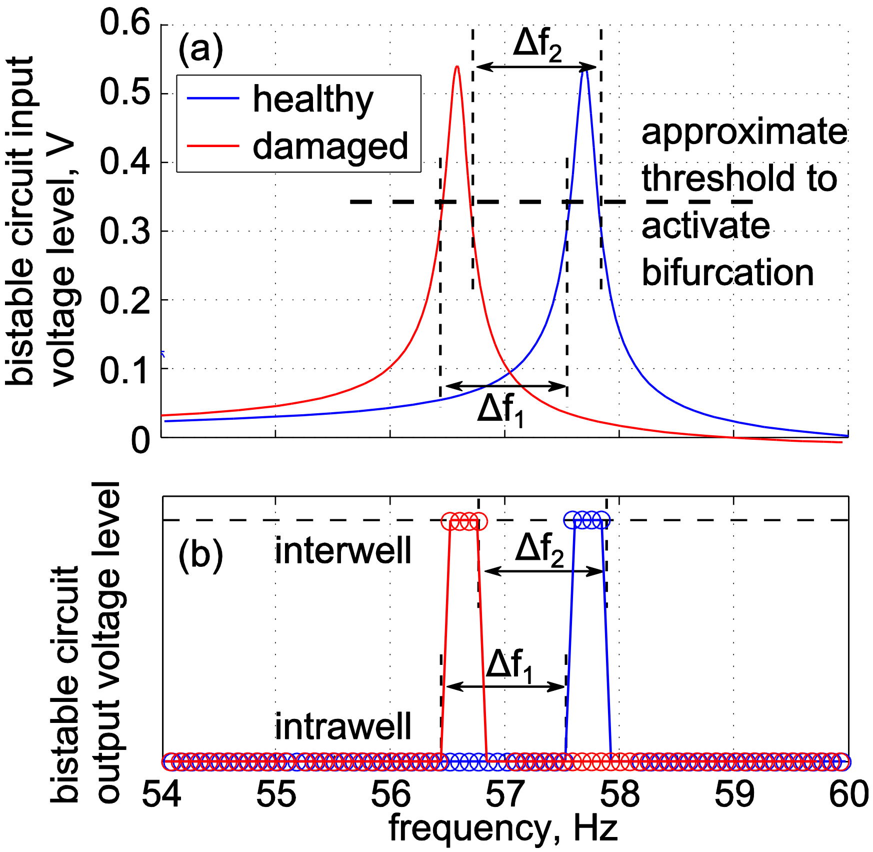

Figure 3.3. (a) Structural response evaluated by the piezoelectric transducer following gain adjustment to serve as bistable circuit input voltage level, highlighting an example activation threshold. (b) Representative output voltage level triggering profile across the spectrum for healthy and damaged structures.

obtained. Thus, from healthy to damaged states, two shifts in frequency are acquired, shown in Figure 3.3(b): one corresponding to the jumps up in output voltage level, and one corresponding to the drops down in level. In this investigation, all of the following results utilize the mean of the two frequency shifts which is considered to be the damage induced frequency shift of the resonance. Moreover, repeating this process using different gain adjustment or bistable circuit parameters (e.g., resistance or inductance) leads to still further frequency shifts, all of which may be taken into consideration when determining a mean frequency shift from healthy to damage structural states which can increase the confidence that the final result is the true frequency shift. By these procedures, the multiple frequency shifts induced by damage may be quantified and employed in the damage identification routine.

3.3. Verification of Bifurcation-Based Detection of Frequency Shifts

In this section, the viability of the bifurcation-based (BB) approach is assessed as compared to DPD method. Since the bistable circuit used in [103] showed good agreement between the numerically predicted and experimentally measured responses, the following damage identification studies are conducted using the same bistable circuit model formulation. The configuration considered of a cantilever beam with integrated bistable and adaptive piezoelectric circuit network is shown in Figure 3.4(a), which specifically represents the implementation of the bifurcation-based frequency shift determination strategy. A cantilevered beam is evenly discretized into ten finite elements and the piezoelectric transducer is considered to be perfectly bonded to the top surface of the beam from the 2nd to 4th element. The transducer is serially connected to an adaptive circuitry. In practice, the tunable inductance may be realized using a floating synthetic inductor as employed by Wang and Tang [32]. Without loss of generality, damage is represented by 15% structural stiffness reduction on the 2nd element in the finite element model of the beam. Relevant parameters used in the damage identification model are listed in Table 3.1.

The following describes the complete damage identification approach using the integrated bistable and adaptive piezoelectric circuitry as employed in this chapter. The healthy structure is first evaluated as a baseline. The excitation voltage V_e is swept over the chosen frequency range, and the piezoelectric admittance of the electro-mechanical system are measured by voltage drops V_i across resistor R. Around each natural frequency of interest, the amplitudes of voltage V_i are scaled to a suitable level by tuning resistor R_b, and this signal is the excitation for the bistable circuit V_b. The activation of bistable circuit bifurcations is then evaluated by analyzing the output voltage level V_o of the bistable circuit as described in Section 3.2. Then, the inductance of the adaptive circuit is selectively tuned as provided in Chapter 2, and the process is repeated for a desired number of inductances to enrich the data set. Once completed, this forms the data set of bifurcation frequencies for the healthy, baseline structure. For damage, the process is repeated, yielding a second data set of bifurcation frequencies. The difference between the data sets of bifurcation frequencies is therefore the collection of frequency shifts to be used in the damage identification routine. To comment on practical implementation of the BB method, for an ideal op-amp junction in the bistable circuit shown in Figure 3.1 no

Table 3.1. System parameters

Beam structure		**Piezoelectric material**	
Length	209.2 mm	**Length**	62.8 mm
Thickness	3.175 mm	**Thickness**	0.191 mm
Width	38.1 mm	**Young's modulus**	66 GPa
Young's modulus	71 GPa	**Density**	7800 $\mathrm{kg/m^3}$
Loss factor	0.3%	**Dielectric constant, β_{33}**	7.1445× 10^{-7} V.m/C
Density	2700 $\mathrm{kg/m^3}$	**Piezoelectric constant, h_{31}**	1.0707× 10^9 N/C

backwards coupling of electrical response will occur to influence the voltage V_i across resistor R [103]. In practice, very small coupling will exist for an on-line implementation of the BB method.

In this initial evaluation, the response signals are free of additive noise. The resonance frequency shift data set is enriched by selecting 14 tunable inductances L, seven different values for each of the 1st and 2nd resonance frequency. Without the adaptive circuitry network, only two resonance frequencies exist in the frequency

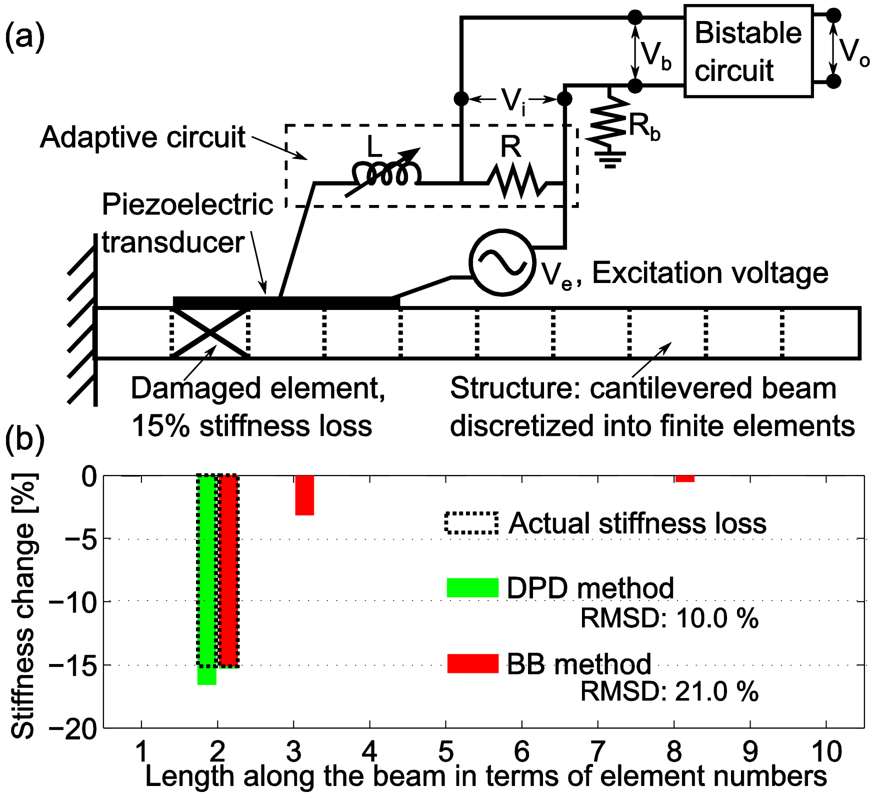

Figure 3.4. (a) Configuration of the cantilever beam integrated with bistable and adaptive piezoelectric circuitry. (b) Identification of damage on 2nd element of the cantilever beam with 15% stiffness reduction.

bandwidth considered. The addition of the circuitry generates a third resonance, and all three are shifted 14 times due to inductance tuning, yielding a total of 42 shifts. The resonance frequency shifts are determined by conventional DPD and the proposed BB approach. In the following studies, the BB method was implemented with numerical simulations of the bistable circuit responses using the governing equations formulated in [103] and random initial conditions. The DPD results were likewise generated by direct computation. Then, damage is identified and prediction results are compared.

The first three resonance frequency shifts as determined by BB and DPD approaches are given in Table 3.2. The resonance frequency shifts obtained by DPD are considered to be accurate because no noise is included in the investigation. Due to the selection of inductances, the 1st and 2nd resonance frequencies of the integrated system vary significantly when the inductance is tuned around 40.0 H; the 2nd and 3rd resonances change when the inductance is tuned around 1.04 H. The multiple frequency shifts acquired by tailoring the tunable inductance value indicate that information about damage is enriched, which improves the rank-deficiency of the inverse problem for damage identification in a similar fashion as presented in Figure 2.3. Table 3.2 shows that the frequency shifts detected by BB and DPD methods exhibit little absolute difference. The mean and standard deviation of the differences are -0.01 and 0.05 Hz, respectively, while the maximum difference is 0.13 Hz.

Figure 3.4(b) presents the damage location and severity predictions following BB or DPD frequency shift detection. It is seen that the results from DPD and BB methods both predict close to the actual 15% stiffness loss at the 2nd element. Root-mean-square deviation (RMSD) between the predicted stiffness reduction $\delta\boldsymbol{d}^{predict}$ and the actual damage $\delta\boldsymbol{d}^{actual}$ is employed as a metric to quantify prediction error:

$$\text{RMSD} = \sqrt{\frac{\sum_{i=1}^{N_{el}}\left(\delta d_i^{predict} - \delta d_i^{actual}\right)^2}{\sum_{i=1}^{N_{el}}\left(\delta d_i^{actual}\right)^2}} \tag{3.1}$$

RMSD by DPD and BB methods both showed relatively small error levels: 10.0 and 21.0 %, respectively. From these results, it can be concluded that the BB method shows comparable performance to the traditional DPD strategy with respect to frequency

Table 3.2. Damage-induced resonance frequency shifts measured by DPD and BB methods under inductance tuning.

Inductance, H	1st resonance frequency shift, Hz			2nd resonance frequency shift, Hz			3rd resonance frequency shift, Hz		
	DPD	BB	Difference	DPD	BB	Difference	DPD	BB	Difference
0.89	1.32	1.34	-0.02	1.22	1.37	-0.15	0.14	0.10	0.04
0.94	1.32	1.33	-0.01	1.16	1.25	-0.09	0.19	0.25	-0.06
0.99	1.32	1.31	0.01	1.01	1.13	-0.12	0.38	0.52	-0.13
1.04	1.32	1.31	0.01	0.44	0.52	-0.08	0.97	1.02	-0.05
1.09	1.33	1.32	0.01	0.05	0.13	-0.08	1.28	1.31	-0.03
1.14	1.30	1.29	0.01	0.03	0.06	-0.03	1.33	1.33	0.00
1.19	1.31	1.31	0.00	0.02	0.06	-0.04	1.33	1.32	0.01
32.5	1.20	1.20	0.00	0.12	0.09	0.03	1.31	1.18	0.13
35.0	1.10	1.10	0.00	0.19	0.21	-0.02	1.31	1.31	0.00
37.5	1.00	1.00	0.00	0.29	0.30	-0.01	1.32	1.31	0.01
40.0	0.87	0.87	0.00	0.45	0.43	0.02	1.31	1.30	0.01
42.5	0.73	0.73	0.00	0.58	0.61	-0.03	1.31	1.28	0.03
45.0	0.59	0.60	-0.01	0.72	0.71	0.01	1.31	1.22	0.09
47.5	0.48	0.48	0.00	0.82	0.82	0.00	1.31	1.23	0.08

shift determination and final damage identification when the response signals are free of noise.

3.4. Improving Accuracy of BB Frequency Shift Detection through Greater Number of Evaluations

The prior section employed a single run of the BB frequency shift detection procedure for use in the damage identification routine. It was found that the identification results following noise-free BB frequency shift determination slightly differed from the DPD approach. Because dynamics associated with the saddle-node bifurcation used in this research are sensitive to initial conditions, and thus activation of the bifurcations may be slightly inconsistent from one time series circuit simulation to the next, it may be anticipated that increased number of runs using randomly selected initial conditions to determine a greater number of frequency shifts may improve confidence in the BB damage identification result. With greater number of runs, the final mean value of detected frequency shift may then be used in the damage identification routine.

Therefore, using the model of Section 3.3, the BB frequency shift detection procedure was carried out for 40 runs with random initial conditions covering several multiples of the stable equilibria of output voltage level (± 1 V) to ensure sufficient sampling of the initial condition parameter space. The mean and first standard deviation of the resulting frequency shifts determined by the BB method are plotted in Figure 3.5(a) (circles and error bars) as compared to the actual resonance frequency shifts (squares), considered to be the DPD method values. The horizontal axis indicates the inductance values used for the data enrichment routine. The individual shift errors determined from

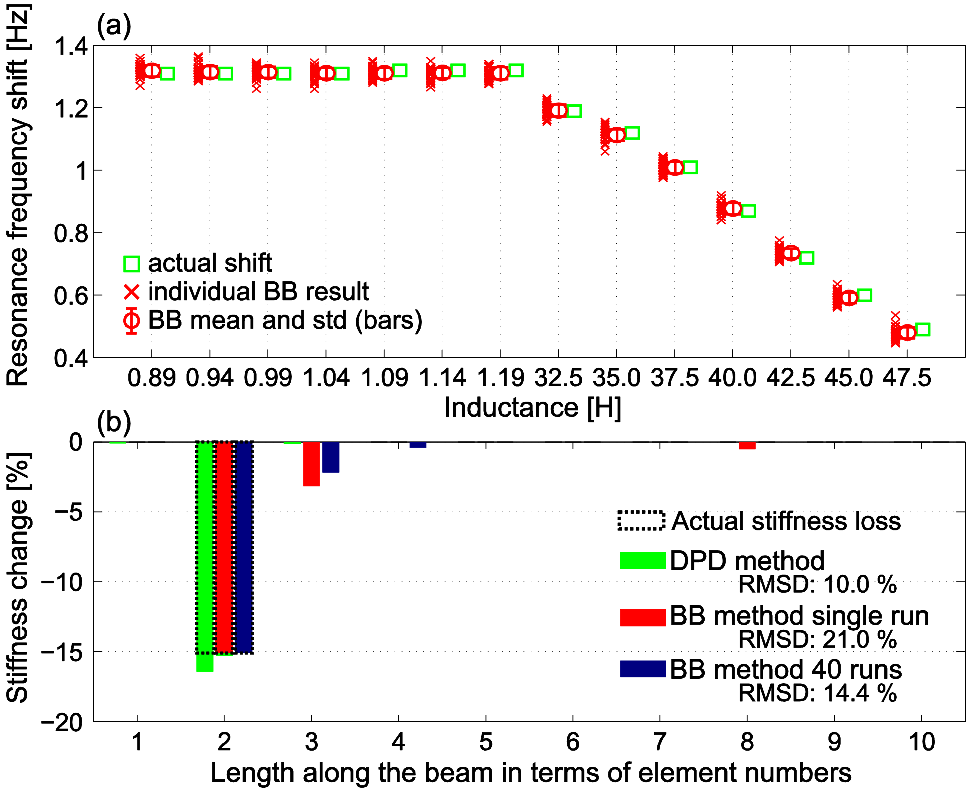

Figure 3.5. (a) Tracking of frequency shifts induced by tuning inductances as determined by BB method using 40 runs of the circuit responses each having random initial conditions. (b) Damage identification using the mean results from the 40 resonance frequency shifts.

all 40 runs for each inductance are plotted as crosses. For conciseness, results from the first resonance peak are plotted; results from the remaining two resonances are comparable. As shown in Figure 3.5(a), the actual resonance frequency shifts are within 1 standard deviation of the BB method mean shift, and the BB method accurately tracks the shifts as inductance is tuned to enrich the data set for the damage identification routine.

The means of the 40 frequency shifts for each of the three shifting resonance frequencies were then utilized for damage identification; the results are provided in Figure 3.5(b). The accuracy of damage predicted by the mean of 40 runs is improved from that computed from a single run: the RMSD is reduced from 21.0 % to 14.4 %. The results indicate that greater number of runs using the BB method may enhance the accuracy of frequency shift determination.

3.5. Investigation of Noise Influences

3.5.1. Case Study 1: Structure with Mild Damping

The prior sections evaluated BB frequency shift determination when the response signals from the structure and adaptive piezoelectric circuitry network were free of noise. However, measurement noise is oftentimes unavoidable. Therefore, this section investigates the addition of random noise, ranging from 44 to 32 dB signal-to-noise ratio (SNR), with the response signals of Sections 4.3 and 4.4 to assess how detection of frequency shifts by DPD and BB methods are affected and how the final damage identification results are influenced. To appreciate the low level of noises employed, Figure 3.6 plots a comparison of an example response resonance used in the following investigation for the noise-free case and that with 32 dB SNR additive low-pass filtered random noise which is the highest level utilized in the following sections. In practice, such low-level noise could be caused by conventional sensor sensitivity constraints [28,104].

The investigation of Section 3.3 was then repeated but now, with each case of inductance tuning, white noise is added to the response signals. Thus, for each of the 14 inductance tuning cases, different frequency shifts for the three resonance peaks may be determined following both DPD and BB methods should noise influence the results. For

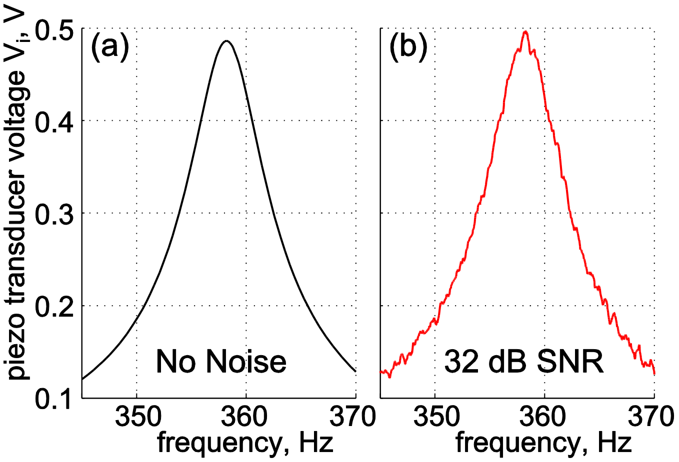

Figure 3.6. Example of (a) noise-free integrated system resonance and (b) that with 32 dB SNR additive noise.

each scenario, a single run of the BB frequency shift detection method and the DPD approach are utilized with a structural response spectra distorted by the same randomly generated additive noise. Figure 3.7 plots the frequency shift error of the 42 individual results (crosses) for each case of noise and detection method, while the mean values are shown as circles with first standard deviations indicated by error bars. The numerical values of first standard deviation are presented alongside each case.

As detailed in the prior sections, the frequency shifts determined by the BB approach when the responses are noise-free exhibit a small but finite spread of values and thus a small range of errors. However, as noise is added to the response signals, the deviations of the frequency shifts by the BB method remain small and steady while those determined by DPD grow significantly, even for the lowest level of noise. Figure 3.8 presents the corresponding damage identification results. Figure 3.8(a) shows that damage location results by DPD alter dramatically with the addition of the lowest level of noise; although the DPD method still correctly predicts approximately 15% stiffness reduction at the 2nd element, now a 41% stiffness reduction is estimated at the 10th element. Since structural health monitoring systems may not distinguish false from accurate damage identification, the incorrect DPD predictions may mislead corrective measures. Figure 3.8(b) presents the RMSD which indicates the BB method is substantially less influenced by the noise addition and its damage identification maintains higher degree of confidence for correctness.

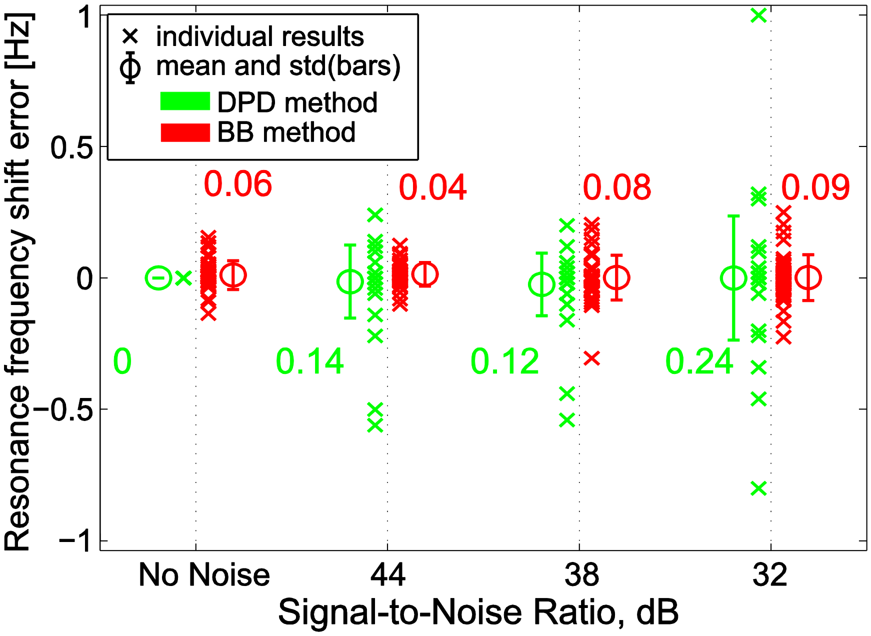

Figure 3.7. Frequency shifts determined by DPD or BB approaches as signal-to-noise ratio increases. Numerical values presented are the standard deviations of the approaches for given noise level.

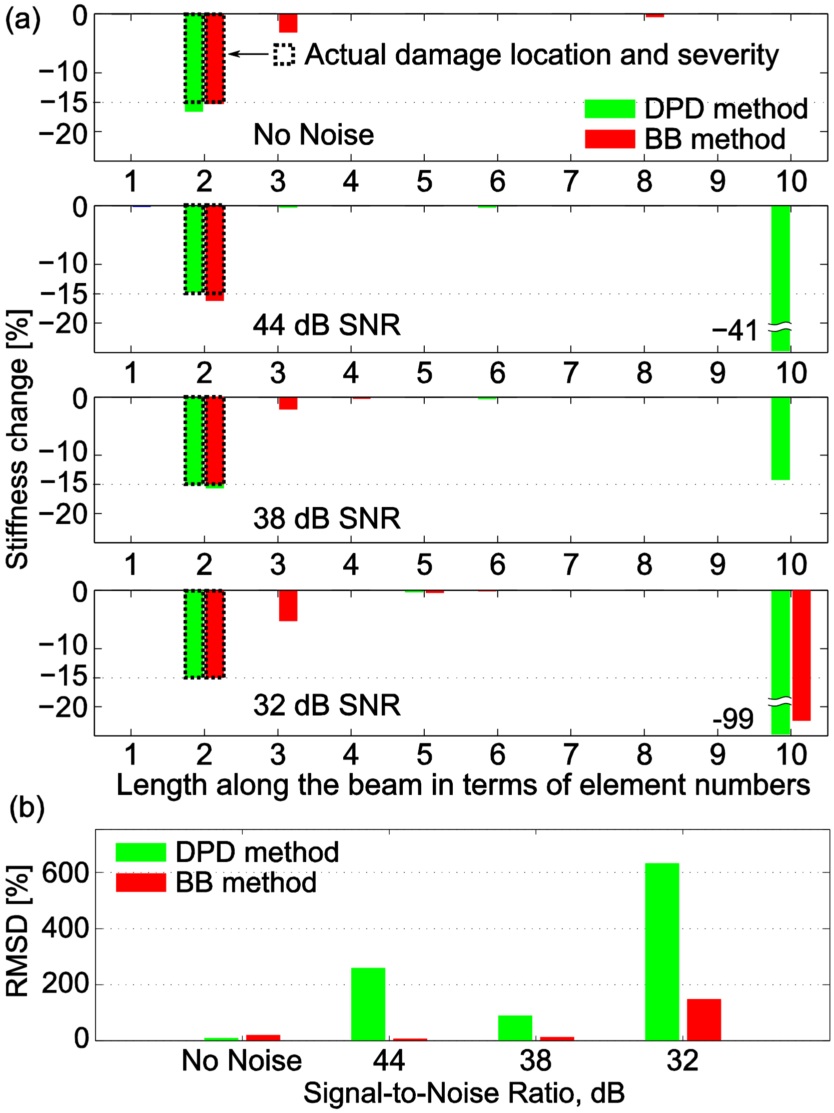

Figure 3.8. (a) Damage identification comparison for structure with mild damping and with varying degrees of low level additive noise. (b) RMSD of damage identification.

3.5.2. Case Study 2: Structure with Increased Damping

The prior investigation considered a lightly damped structure with loss factor 0.3%. While some structural systems may have such low damping in an ideal form and configuration, the introduction of boundary conditions, imperfections in mounting, and even structural-acoustic factors often contribute to increase damping levels in civil and mechanical structures. Thus, this section repeats the additive noise study of Section 3.5.1 but increases the cantilever beam loss factor from 0.3 to 0.5%.

Figure 3.9(a) presents the resulting damage identification comparing DPD and BB frequency shift detection approaches as noise increases while 4.9(b) provides the corresponding RMSD. In tandem with increased structural damping levels, Figure 3.9 shows that DPD-based damage identification becomes unreliable and justifies common suspicions that the approach has clear disadvantages despite its appealing ease of implementation. In contrast, the BB method for frequency shift determination provides improved robustness to noise and damping and the more accurate damage predictions attest to its advantages. While the BB method ultimately yields some measurement error, as described in earlier sections, increasing the number of runs, using greater number of gain adjustments, or tailoring bistable circuit parameters could provide means to heighten confidence in its robust measurement capability and further enhance its performance for accurate damage identification.

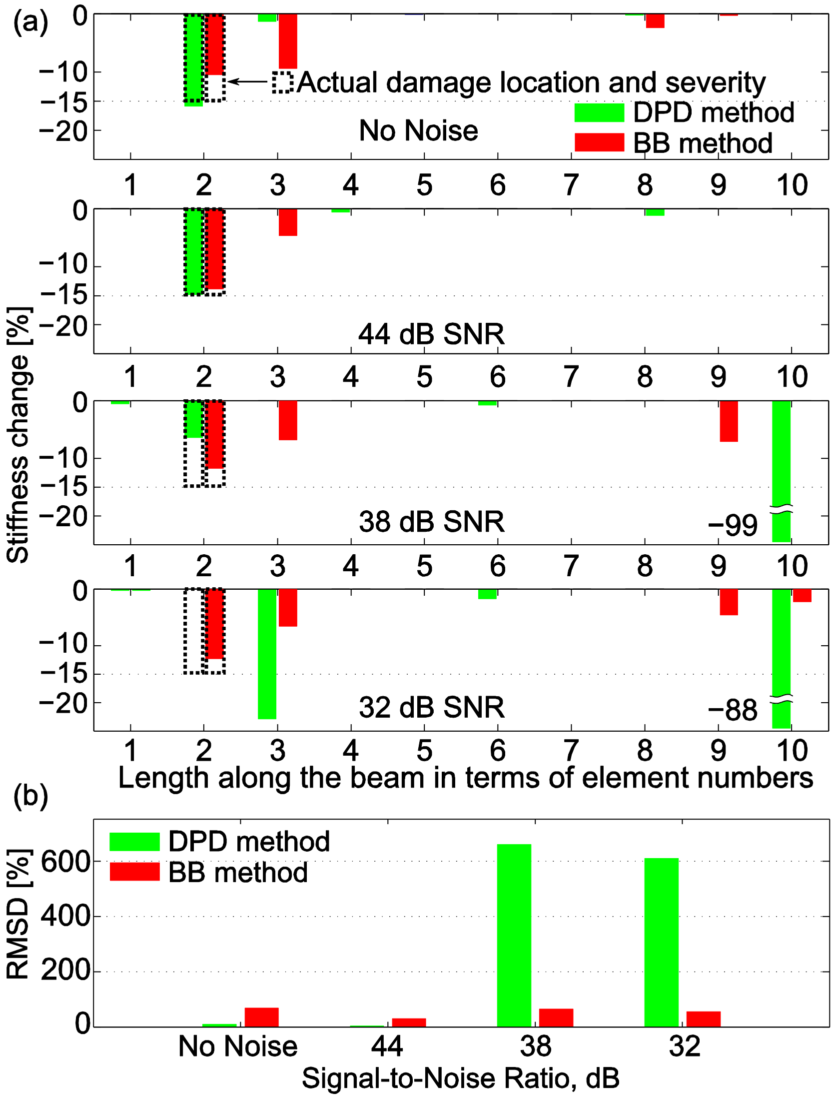

Figure 3.9. (a) Damage identification comparison for structure with increased damping and for varying degrees of low level additive noise. (b) RMSD of damage identification.

3.6. Summary and Conclusion

This chapter investigates an integration of bistable and adaptive piezoelectric circuitry to enhance the robustness and accuracy of the impedance model-based structural damage identification, which are otherwise compromised due to noise and damping. A novel methodology to determine the damage-induced spectral change of the structure is explored based on the utilization of strongly nonlinear bifurcation phenomena. The strong nonlinearity, which is not common in large-scale structures, is introduced by a bistable electric circuit integrated to the host structure through piezoelectric transducer. The electrical admittance measured from the piezoelectric transducer is fed into the bistable circuitry which exhibits saddle-node bifurcation. By tracking the activation of this circuitry bifurcation, the damage-induced resonance frequency shift can be clearly determined. Numerical investigation verifies that this bifurcation-based sensing approach is significantly less affected by the addition of noise and damping in the response signals, and thus provides higher level of confidence in its final damage identification results.

CHAPTER 4

Predicting Non-Stationary and Stochastic Activation of Saddle-Node Bifurcation in Non-Smooth Dynamical Systems

4.1. Introduction

As illustrated in Chapter 3, the core principle of the proposed bifurcation-based sensing approach is based on tracking the onset of saddle-node bifurcation that induces dramatic changes in the response level. On the other hand, it is well known that saddle-node bifurcation activation is strongly influenced by noise and non-stationary influences that are unavoidable and ever-present in practical applications. As a result, it is critical to understand whether the bifurcation is activated due to actual damage-related structural changes or the noise and nonstationary influences to successfully implement the advanced bifurcation-based sensing approach. Otherwise, the reliability of bifurcation-based sensing will be greatly degraded. Although the results presented in Chapter 3 bolsters the remarkable potential of the new bifurcation-based sensing approach using bistable circuitry, the preliminary analysis only considered stationary inputs to the circuit. Therefore, in this chapter the dynamic and stochastic activation of saddle-node bifurcation is theoretically investigated to estimate the onset of bifurcation, so that the findings can be incorporated into developing a reliable sensing strategy for practical applications.

Bifurcation is an important consideration in dynamical systems since it may lead to qualitative changes in the response topology by even minute variation of system parameters across the critical point [105]. Especially, saddle-node bifurcation generally induces large and sudden changes in the response amplitude since the system loses local stability as two coexisting equilibria collide and annihilate each other [105,106]. In order to exploit or avoid the dramatic changes induced by saddle-node bifurcation, it is critical to accurately estimate the onset of saddle-node bifurcation, or the conditions that induce the associated stability loss.

The classical saddle-node bifurcation in smooth dynamical systems has been extensively studied, motivated by various engineering and scientific applications including Josephson-junction circuits [94,107], micro-/nanomechanical oscillators [108,109], chemical reactions [110], and ecological [111–113] and climate systems [114,115]. It is well known that saddle-node bifurcation is strongly affected by stochastic and non-stationary factors. For example, noise may result in premature saddle-node bifurcations [116–118] which occur even before the governing parameter reaches the critical value that activates deterministic bifurcations. In contrast, non-stationarity of the key parameters may delay the activation of bifurcation [119,120]. It has been extensively studied to understand how the dual influence of stochastic and non-stationary factors affects the activation of smooth saddle-node bifurcations by introducing scaling laws [121–123], deriving exact and approximate responses of the stochastic normal form [124], and approximating the distribution of the escape events induced by the bifurcation [125,126].

On the other hand, non-smooth dynamics are observed in many practical systems. Examples of these systems range from mechanical devices with physical phenomena such as dry friction [127] and impact [128], robotic applications with walking and hopping mechanics [129,130], and electrical circuits with diode elements [103,131–133] to biological system model of neural networks [134] and economic models [135,136]. An extensive set of examples can be found in [137–139]. Although non-smooth dynamical systems have received increased attention in recent years, little is known about the bifurcations in non-smooth systems compared to those of the classical smooth systems. Since the saddle-node bifurcation induces local stability loss of the system, investigation on the bifurcation point is directly associated with stability analysis. A number of researchers have studied the stability of non-smooth dynamical systems, for example, by examining how small perturbations from the initial conditions propagate in periodic response [140,141] and evaluating the eigenvalues of the Jacobian matrix of a Poincaré map [138,142,143]. On the other hand, these advancements are focused on the steady-state response of deterministic system not considering the critical influences of noise and non-stationarity on the stability. Therefore, in this chapter, the coupled influence of stochastic and non-stationary factors is investigated to accurately predict the onset of non-smooth saddle-node bifurcation. While a qualitative scaling law of the time delay near non-smooth saddle-node bifurcation is introduced in [144], this chapter presents quantitative results about the distribution of bifurcation points, which will provide a direct means for enhancing practical applications involving non-smooth saddle-node bifurcation.

In the following sections, a stochastic normal form of non-smooth saddle-node bifurcation is introduced to examine the dual influence of noise and non-stationarity on the bifurcation activation by using a single parameter. Numerical and experimental investigations employing a double-well Duffing analog circuit are carried out to verify the distribution of the onset of bifurcations predicted by the theoretical framework. Following the investigations, concluding remarks summarize and reflect upon the potential of the new approach.

4.2. Stochastic Normal Form of Dynamic Saddle-Node Bifurcation

The normal form of classical saddle-node bifurcation of a smooth system

$$\dot{x} = \mu + x^2 \tag{4.1}$$

exhibits two equilibria for bifurcation parameter $\mu < 0$, where fixed point $x^* = -\sqrt{\mu}$ is stable while $x^* = \sqrt{\mu}$ is unstable. When the parameter $\mu < 0$ quasi-statically increases, the system becomes unstable as saddle-node bifurcation occurs at $\mu = 0$ annihilating the two equilibria (Figure 4.1(a)), and the response of the system escapes from the dynamics local to the bifurcation point and generally jumps to other stable equilibrium of the system. Now the counterpart in non-smooth systems can be obtained by replacing the term x^2 by $|x|$

$$\dot{x} = \mu + |x|, \tag{4.2}$$

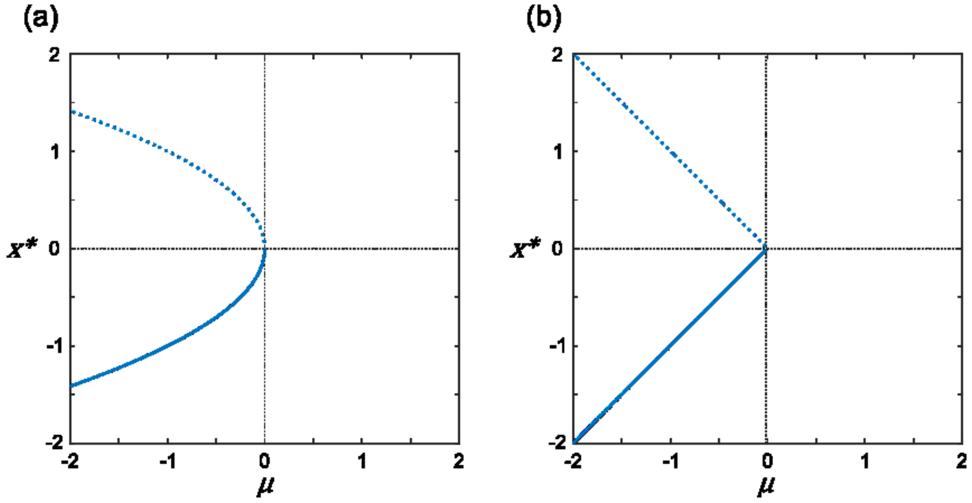

Figure 4.1. Bifurcation diagrams of (a) smooth and (b) non-smooth saddle-node bifurcation. Solid (dotted) lines indicate (un)stable fixed points.

which has two equilibria $x = \pm\mu$ for $\mu < 0$ as shown in the bifurcation diagram, Figure 4.1(b). The stochastic normal form of the saddle-node bifurcation is utilized to investigate the stochastic and non-stationary influences on the activation of saddle-node bifurcations.

$$\dot{x} = \mu(t) + |x| + D\xi, \tag{4.3}$$

where D is effective noise strength and ξ is Gaussian white noise with autocorrelation $\langle \xi(t)\xi(\tilde{t}) \rangle = 2\delta(t - \tilde{t})$. The non-stationary influence on the saddle-node bifurcation is assessed by examining the system stability with respect to a time dependent bifurcation parameter $\mu(t)$. For a common case of broad practical applications, a first order Taylor expansion of $\mu(t)$ in time is employed in this analysis, such that

$$\mu(t) = \mu_0 + rt. \tag{4.4}$$

In this research, it is assumed that the bifurcation parameter is swept from $\mu_0 < 0$ at a sweep rate of $r > 0$. Since the bifurcation parameter $\mu(t)$ varies linearly in time, the time can be scaled according to the parameter sweep rate. By introducing new variables

$$\tau = \mu r^{-1}, \tag{4.5}$$

$$z = x r^{-1}, \tag{4.6}$$

and substituting them into Eq. (4.3), a new scaled normal form can be obtained as,

$$z' = \tau + |z| + \alpha\xi, \tag{4.7}$$

$$\alpha = D/r, \tag{4.8}$$

where $(\ )'$ indicates differentiation with respect to scaled time τ. As a result, one can utilize a single parameter, scaled noise level α, to investigate the dual influence of noise and non-stationarity on the activation of non-smooth saddle-node bifurcation. Since the normal form describes the local dynamics near bifurcation point, when bifurcation is activated the system trajectories become very steep diverging to infinity. In this work, it is assumed that the time T at which the system reaches a large value $(z_\infty \gg 1)$ is equivalent to the time taken to infinity. Therefore, our goal is to determine the distribution of escape time T at which the response of Eq. (4.7) becomes unbounded, i.e. $z(T) \to \infty$. The Fokker-Planck Equation (FPE) [145] can be derived from the scaled stochastic normal form (Eq. (4.7)) as

$$\frac{\partial \rho(z,\tau)}{\partial \tau} = -\frac{\partial}{\partial z}\left[(\tau + |z|)\rho(z,\tau)\right] + \alpha^2 \frac{\partial^2 \rho(z,\tau)}{\partial z^2}, \tag{4.9}$$

where $\rho(z,\tau)$ is the probability density function (PDF) for finding the system at z at time τ. By integrating the FPE, the PDF for escape at time T can be obtained as

$$P(T) = \frac{d}{d\tau}\left(1 - \int_{-\infty}^{z_\infty} \rho(z,\tau)dz\right). \tag{4.10}$$

For conditions where bifurcation parameter μ increases relatively slowly with respect to the noise level $(\alpha \gg 1)$, one can assume that the bifurcation parameter is adiabatically swept through the critical value, and thus the rate of escape events can be approximated by the well-known Kramer's rate $W(\tau)$ in Eq. (4.11) [116]. As a result, the approximate PDF of escape $P_K(T)$ can be derived as Eq. (4.12).

$$W(\tau) = \frac{1}{2\pi} \exp\left(-\frac{(-\tau)^2}{\alpha^2}\right) \tag{4.11}$$

$$P_K(T) = W(T) \exp\left(-\int_{\tau_0}^{T} W(\tau) d\tau\right) \tag{4.12}$$

In summary, the key result is that the stochastic and non-stationary activation of non-smooth saddle-node bifurcation can be estimated by using a single parameter, scaled noise α in Eq. (4.8). The distribution of escape time T can be used to assess the bifurcation point, or the actual critical parameter value, that triggers the bifurcation by straightforward back-calculation from Eq. (4.5).

4.3. Numerical and Experimental Investigations

In this section, the theoretical prediction of the escape statistics utilizing the scaled normal form of non-smooth saddle-node bifurcation is validated through numerical and experimental investigations. Figure 4.2(a) shows a schematic diagram of a double-well Duffing analog circuit employed in this research. This circuit exhibits bistability with piecewise-linear characteristics introduced by nonlinear feedback loop among an op-amp and a pair of anti-parallel diodes, i.e., diodes with two terminals shortened in opposite directions. As a result, non-smooth saddle-node bifurcation occurs when the excitation amplitude of the circuit increases while the excitation frequency is fixed below the linear resonance frequency. By virtue of the saddle-node bifurcation that activates drastic transitions between the intra- and interwell oscillations in the output voltage level, the bistable circuit has been successfully utilized for several applications including bifurcation-based sensing for detecting parameter changes and damages in structures [103,132].

The governing equation of the bistable circuit can be derived by assuming ideal op-amp and diode characteristics as the following [146].

$$LC\,\ddot{V}_o + RC\,\dot{V}_o + F(V_o) = V_i\,, \tag{4.13}$$

$$F(V_o) = \begin{cases} V_o - gV_D\,, & V_o > V_D \\ (1-g)V_o\,, & |V_o| \le V_D, \\ V_o + gV_D\,, & V_o < -V_D \end{cases} \tag{4.14}$$

where L, C, R, and $F(V_o)$ represent the inductance, capacitance, resistance, and a nonlinear voltage function, respectively; V_i, V_o, and V_D respectively indicate the input and output voltage amplitudes of the bistable circuit, and voltage drop over an open diode; and the overdot indicates a time derivative. Following ideal op-amp assumption, the feedback gain is $g = 1 + R_2/R_1$. The op-amp employed in this research is LM741CN and the diodes are 1N4148. The other relevant circuit parameters are provided in Table 4.1.

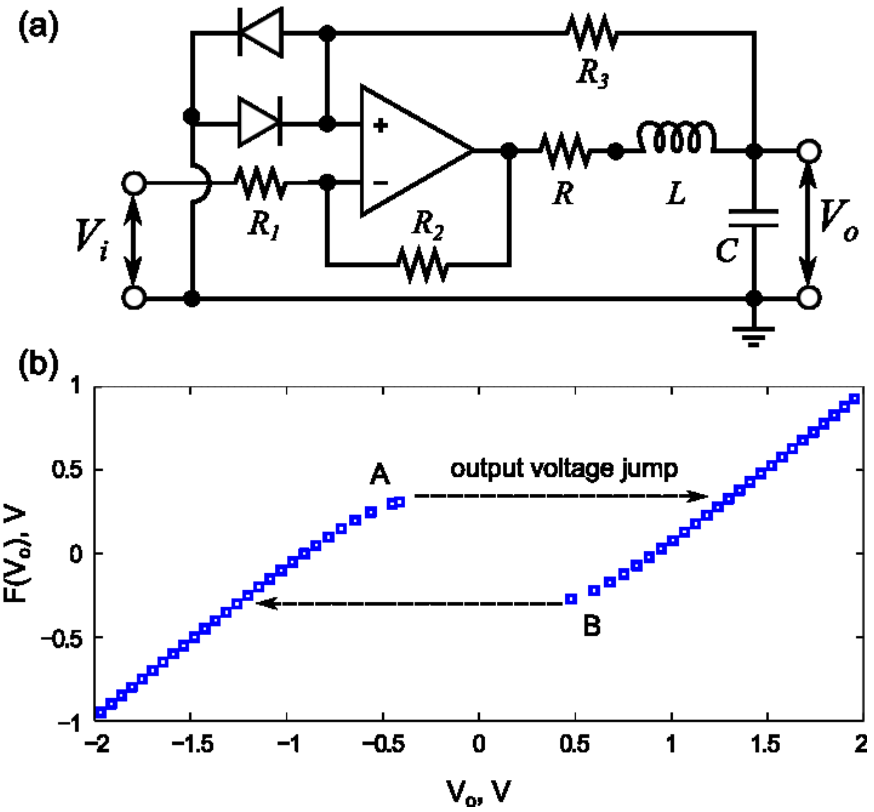

Figure 4.2. (a) Schematic diagram of the double-well Duffing analog circuit utilized in experimental analysis. (b) Experimentally measured nonlinear voltage function of the circuit with respect to output voltage amplitude.

Table 4.1. Experimental system parameters of the double-well Duffing analog circuit.

L, *mH*	C, *uF*	R, Ω	R_1, *k*Ω	R_2, *k*Ω	R_3, *k*Ω
10.24	*0.96*	*800*	*9.07*	*9.08*	*10*

Considering the overdamped limit of large damping, the term $LC\ddot{V}_o$ can be neglected. Although the circuit exhibits two saddle-node bifurcations as the amplitude of harmonic excitation is increased and decreased, for consistency it is focused on the saddle-node bifurcation that occurs for increasing amplitude of the excitation. When small perturbations $\eta = V_i - V_i^{cr}$ and $x = V_o - V_o^{cr}$ near a critical fixed point $(V_i^{cr}, V_o^{cr}) = \big((g-1)V_D, -V_D\big)$ at which the bifurcation is induced for deterministic system are introduced and substituted into Eqs. (4.13) and (4.14), the local dynamics around the bifurcation point can be expressed by

$$\dot{x} = \frac{1}{RC}(\eta + |x|). \tag{4.15}$$

By assuming the stochastic influence as an additive Gaussian white noise term $D\xi$ [147] and scaling the variables as $\tau = \mu(r_V RC)^{-1}$ and $z = x(r_V RC)^{-1}$ in a similar manner to Eqs. (4.5) and (4.6), a scaled normal form of non-smooth saddle-node bifurcation is finally derived:

$$z' = \tau + |z| + \alpha_V \xi. \tag{4.16}$$

r_V is input voltage amplitude sweep rate and scaled noise level $\alpha_V = \frac{D}{RC\, r_V}$. $(\ )'$ indicates differentiation with respect to scaled time τ.

Figure 4.2(b) displays the qualitative piecewise-linear characteristics of the nonlinear voltage function $F(V_o)$ of the bistable circuit, which corresponds to the smooth restoring force of a conventional double-well Duffing oscillator expressed by a cubic polynomial with negative linear and positive cubic terms [106,148]. The voltage function is experimentally obtained by measuring the output voltage V_o while quasi-statically varying the DC input voltage within the range that encompasses the two stable equilibria of the bistable circuit. Starting from large negative value, when the DC input voltage is quasi-statically increased around 0.32 V, indicated as point A in Figure 4.2(b), bifurcation is activated and the output voltage V_o undergoes a sudden transition from approximately -0.42 V to 1.30 V. For decreasing input voltage level, the bistable circuit exhibits a symmetric behavior of jump event due to the bifurcation. The critical fixed point (V_i^{cr}, V_o^{cr}) in this analysis can be determined as $(0.32, -0.42)$. On the other hand, due to the practical factors ignored in the ideal diode model, such as temperature effect and nonlinearity in the diode [149], the slope near the bifurcation point decreases as shown in Figure 4.2(b). To account for these effects, the slope was measured ($a \approx 0.2$) and considered in the normal form derivation, yielding $\alpha_V = \frac{aD}{RC\, r_V}$.

The double-well Duffing analog circuit is harmonically excited at 35 Hz and the input voltage amplitude is increased by sweeping across the bifurcation point starting from 0.3 V to 0.4 V. In addition to the ambient noise level, different levels of Gaussian white noise are added to the excitation input voltage to examine the stochastic influences on the saddle-node bifurcation activation. The root-mean-square (rms) amplitude of the ambient noise in the experiment is 0.015 mV. The input voltage amplitude sweep rates and the additive noise levels applied in the experiment are given in Table 4.2. Note that the sweep conditions and noise levels are in the range that does not induce other

Table 4.2. Scaled noise level α for each sweep rate and additive noise level applied in the experimental investigation.

sweep rate, mV/s	0.5	2	10	10	10	10
noise level, mV rms	10	50	10	50	100	100
α	9.2	7.4	184.1	36.8	18.4	7.4
sweep rate, mV/s	50	50	50	50	50	50
noise level, mV rms	10	50	100	250	500	1000
α	920.7	184.1	92.1	36.8	18.4	9.2

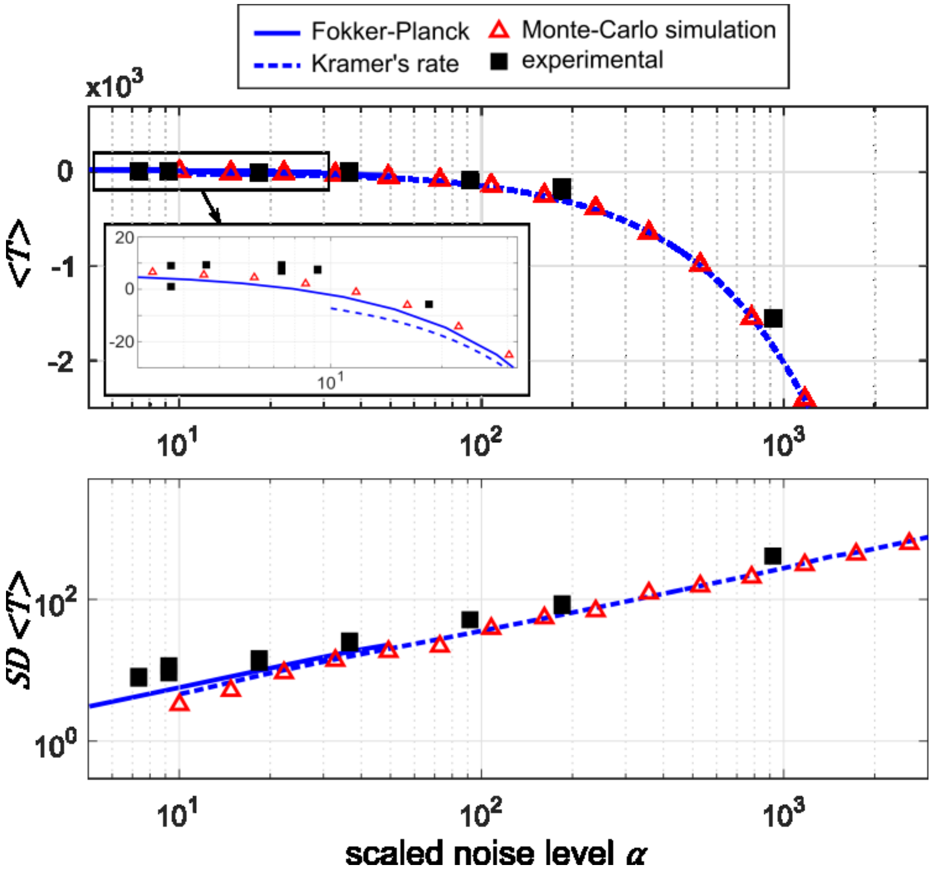

Figure 4.3. The analytically predicted mean and standard deviation of escape time *T* using Fokker-Planck equation (solid line) and Kramer's rate (dashed line) are compared with the results obtained by Monte-Carlo simulation (triangle), and experimental measurement (square) with respect to the scaled noise level α. Inset figure shows zoomed view for small α.

bifurcation in the bistable circuit, which satisfies the assumption of utilizing the normal form for analysis in this work. The input voltage amplitude V_{esc} that triggers non-smooth saddle-node bifurcation is recorded and utilized to derive the scaled escape time $T = (V_{esc} - V_i^{cr})/(RC\, r_V)$. Note that the scaled escape time is greater than zero when delayed bifurcation occurs, while it gives negative value for premature bifurcations. The mean $\langle T \rangle$ and standard deviation $SD\,\langle T \rangle$ of the escape time are obtained from 100 runs for each condition with various sweep rates and noise levels. In Figure 4.3, the mean and standard deviation of the escape times estimated by the theoretical framework using Fokker-Planck equation (solid curve) and adiabatic approximation (dashed line) for large α are plotted with the experimentally obtained results (square) as a function of scaled noise level α. In addition, Monte-Carlo based results (triangle) obtained by numerically solving the scaled stochastic normal form in Eq. (4.16) for 1000 times via Euler-Maruyama method [150] are included in Figure 4.3 for comparison. It can be observed that the escape statistics estimated by the scaled normal form are in good agreement with the numerically and experimentally determined results. Both of the delayed ($T > 0$) and premature ($T < 0$) escape events in the bistable circuit are successfully predicted for small and large values of scaled noise level, respectively. Overall, the experimental and numerical investigation results obtained for a wide range of bifurcation parameter sweep rates and noise levels strongly support and validate the prediction obtained by the proposed scaled normal form Eq. (4.7). The theoretical analysis derived based on normal form herein will provide an effective new means for predicting the onset of critical transitions related to saddle-node bifurcation in a variety of non-smooth systems under non-stationary and stochastic influences.

4.4. Summary and Conclusion

The non-stationary and stochastic influences on the activation of non-smooth saddle-node bifurcation are investigated to develop a theoretical foundation for predicting critical parameters that activate escape from a stable equilibrium. A new scaled normal form of non-smooth saddle-node bifurcation is derived, which enables examining the dual influence on the escape event by using a single parameter. The distribution of the onsets of bifurcation is then quantitatively predicted from the Fokker-Planck equation corresponding to the scaled normal form. Numerical and experimental investigations using a double-well Duffing analog circuit successfully verify the accuracy of the predictions obtained by the theoretical framework. Since the predictive strategy developed here is based on normal form analysis, it is expected that this theoretical framework will provide a straightforward and accurate means for estimating critical conditions that lead to sudden large jumps in the response of various practical contexts associated with non-smooth saddle-node bifurcation.

CHAPTER 5

Enhancing Impedance-Based SHM using Bistable and Adaptive Piezoelectric Circuitry

5.1. Introduction

While Chapter 3 has vividly illustrated the potential for integrating the bifurcation-based (BB) sensing strategy using bistable circuitry with the impedance-based SHM, the preliminary study was based on employing stationary structural responses in relatively low frequency range as input for the bistable circuit. This chapter investigates a novel BB sensing method utilizing a network of bistable circuits that enables high frequency interrogation to determine small damage-induced impedance changes, while considering the unavoidable noise and non-stationary influences on the bifurcation activations revealed in Chapter 4. In conjunction with the data enrichment concept investigated in Chapter 2, this chapter develops a new impedance-based SHM approach that can accurately identify the location and severity of small structural damages under realistic noise influences.

In the following sections, the damage identification approach utilizing adaptive piezoelectric circuitry is first summarized. Then, the new approach for damage-induced impedance change measurement using bifurcations in an array of bistable circuits is discussed with design guidelines considering practical implementations. Numerical and experimental damage identification efforts are conducted to verify the effectiveness of the proposed approach against noise contamination. Following the investigations, concluding remarks are provided to summarize and reflect upon the potential of the new approach.

5.2. Overview of Damage Identification Using Adaptive Piezoelectric Circuitry

This section briefly reviews the damage identification algorithm previously introduced in Chapter 2, which is integrated with the bifurcation-based sensing approach explored in this chapter. Figure 5.1 shows a schematic of an example structure integrated with electric circuit for piezoelectric impedance measurement and adaptive piezoelectric circuit with tunable inductor. The piezoelectric admittance $Y(\omega)$, inverse of the

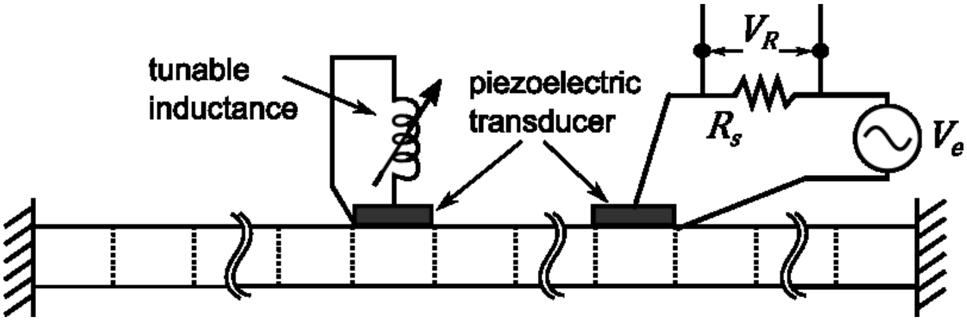

Figure 5.1. Illustration of monitored structure integrated with adaptive piezoelectric circuitry.

piezoelectric impedance, at frequency ω is obtained by the voltage drop V_R across the resistor R_s [27],

$$Y(\omega) = \frac{1}{R_s}\frac{V_R}{V_e}, \tag{5.1}$$

where V_e is the excitation voltage. By employing the spectral element method [82,85], the admittance of the integrated system can be derived as

$$Y(\omega) = \frac{1}{R_s}k_1\left[k_2\mathbf{\Phi}_p\mathbf{S}^{-1}(\omega)\mathbf{\Phi}_p^{\mathrm{T}} + 1\right] \tag{5.2}$$

where $\mathbf{S}(\omega)$ represents the frequency dependent dynamic stiffness matrix and k_1, k_2 are coefficients related to the geometry and material properties of the integrated system. The vector $\mathbf{\Phi}_p$ indicates the location of the piezoelectric transducer in the model discretized into N elements. For example, when damage is assumed as local stiffness reduction in the structure, a vector of damage indices can be defined as $\mathbf{d} = [\mathrm{d}_1, \mathrm{d}_2, \dots, \mathrm{d}_\mathrm{N}\ ]^\mathrm{T}$, where d_i represents stiffness reduction of the i-th element. Since the stiffness terms are nonlinearly formulated in the dynamic stiffness matrix inverse $\mathbf{S}^{-1}(\omega)$ of the damaged structure, Taylor series expansion of $Y(\omega)$ is employed to derive the inverse problem and explicitly determine the stiffness reduction induced by damage.

$$\Delta\boldsymbol{Y}(\mathbf{d}) = \mathbf{G}\times\mathbf{d} \tag{5.3}$$

where sensitivity matrix $\mathbf{G} = \partial\boldsymbol{Y}(\omega)/\partial\mathbf{d}|_{\mathbf{d}=0}$ and $\Delta\boldsymbol{Y}(\mathbf{d})$ is a vector of damage-induced piezoelectric admittance changes. The location and severity of the damage can be identified by solving for the damage index vector $\hat{\mathbf{d}}$ that minimizes the difference between the vector of experimentally measured admittance change $\Delta\boldsymbol{Y}_m$ and the vector of admittance changes predicted by the baseline model $\Delta\boldsymbol{Y}(\mathbf{d})$.

$$\hat{\mathbf{d}} = \mathrm{argmin}_{\mathbf{d}}\|\Delta\boldsymbol{Y}_m - \Delta\boldsymbol{Y}(\mathbf{d})\| \tag{5.4}$$

This inverse problem is often highly underdetermined since the number of independent impedance measurement data sets are generally far smaller than the number of required system parameters, which leads the damage index vector $\hat{\mathbf{d}}$ to be unstable and severely sensitive to noise in $\Delta \boldsymbol{Y}_e$. However, this limitation can be addressed by utilizing an adaptive piezoelectric circuitry with tunable inductor integrated to the monitored structure. For example, when the inductance values are strategically tuned from L_1 to L_n [76,151], n different sets of inverse equations can be obtained, i.e., $\Delta \boldsymbol{Y}(L_i) = \mathbf{G}(L_i) \times \mathbf{d}$, where the sensitivity matrix $\mathbf{G}(L_i)$ and the admittance changes $\Delta \boldsymbol{Y}(L_i)$ are both dependent on the inductance value L_i. By augmenting these equations in a matrix form and substituting into Eq. (5.4), one can significantly enhance the underdetermined inverse problem by increasing independent information about the damage in the inverse problem formulation as the following:

$$\hat{\mathbf{d}} = \operatorname{argmin}_{\mathbf{d}} \|\Delta \boldsymbol{Y}_m^L - \Delta \boldsymbol{Y}^L(\mathbf{d})\| \tag{5.5}$$

$$\Delta \boldsymbol{Y}^L(\mathbf{d}) = \begin{Bmatrix} \Delta\mathbf{Y}(L_1) \\ \Delta\mathbf{Y}(L_2) \\ \vdots \\ \Delta\mathbf{Y}(L_n) \end{Bmatrix} = \begin{bmatrix} \mathbf{G}(L_1) \\ \mathbf{G}(L_2) \\ \vdots \\ \mathbf{G}(L_n) \end{bmatrix} \times \mathbf{d} \tag{5.6}$$

where $\Delta \boldsymbol{Y}_m^L$ is the vector of experimentally measured admittance changes of the integrated system with corresponding inductances.

5.3. Impedance Change Measurement Using Bifurcations in Bistable Circuitry Network

Section 5.2 shows that the impedance variations induced by damage occurrence are utilized as input for the damage identification routine enhanced by the adaptive piezoelectric circuitry. Yet, the impedance changes induced by small damages may not be easy to accurately measure. This is because with high frequency interrogation, the response can be suppressed by structural damping and thus easily be buried in noise. In order to address this concern, this research develops a new method that enables robust measurement of the damage-induced impedance variations against noise contamination by utilizing the bifurcation phenomena in a network of bistable circuits for structural damage identification.

5.3.1. Overview of Impedance Change Measurement Using a Network of Bistable Circuits

Figure 5.2(a) presents the configuration of a beam structure integrated with the proposed bistable and adaptive piezoelectric circuitry. The double-well Duffing analog circuit [103,126,146] employed as bistable circuit in this study (Figure 4.2(a)) involves saddle-node bifurcation activated when the input voltage amplitude exceeds a critical threshold, while the excitation frequency is fixed at a value that is below the linear resonance frequency of the circuit. As a result, the circuit undergoes sudden and dramatic change in the output voltage level with minute input voltage variation around the critical threshold. For example, when the input voltage amplitude is lower than the bifurcation threshold, the bistable circuit output voltage undergoes small amplitude, intrawell oscillations; whereas for higher input levels, the circuit may exhibit output with large amplitude interwell oscillations. We capitalize on this drastic response change that yields remarkable sensitivity to the input voltage variation for measuring minute changes in the piezoelectric impedance induced by damage occurrence.

By strategically integrating the bistable circuitry with the host structure and piezoelectric transducer as shown in Figure 5.2(a), the electromechanical impedance that reflects the structural response effectively becomes the input to the bistable circuit following gain adjustment. As a result, by monitoring the bifurcation in the output voltage V_o that is activated by the impedance changes, one can assess the structural change associated with the occurrence of damage. Figure 5.2(b) shows an example of structural response around resonance obtained by the piezoelectric transducer. Since structural damage is assumed as local stiffness reduction in this study, the occurrence of damage reduces the resonance frequency and increases the structural response at frequencies below the linear natural frequency. When a bistable circuit is designed such that the bifurcation threshold (h0 in Figure 5.2(b)) is located between the structural responses of the healthy and damaged structures for harmonic excitation at frequency ω_o, the healthy structure may generate small amplitude intrawell oscillation in the output voltage of the bistable circuit since the input voltage level is lower than the bifurcation threshold, while the damaged structure may induce large amplitude interwell oscillation as compared in Figure 5.2(c). This drastic change in the output voltage can be utilized to assess the impedance change induced by damage.

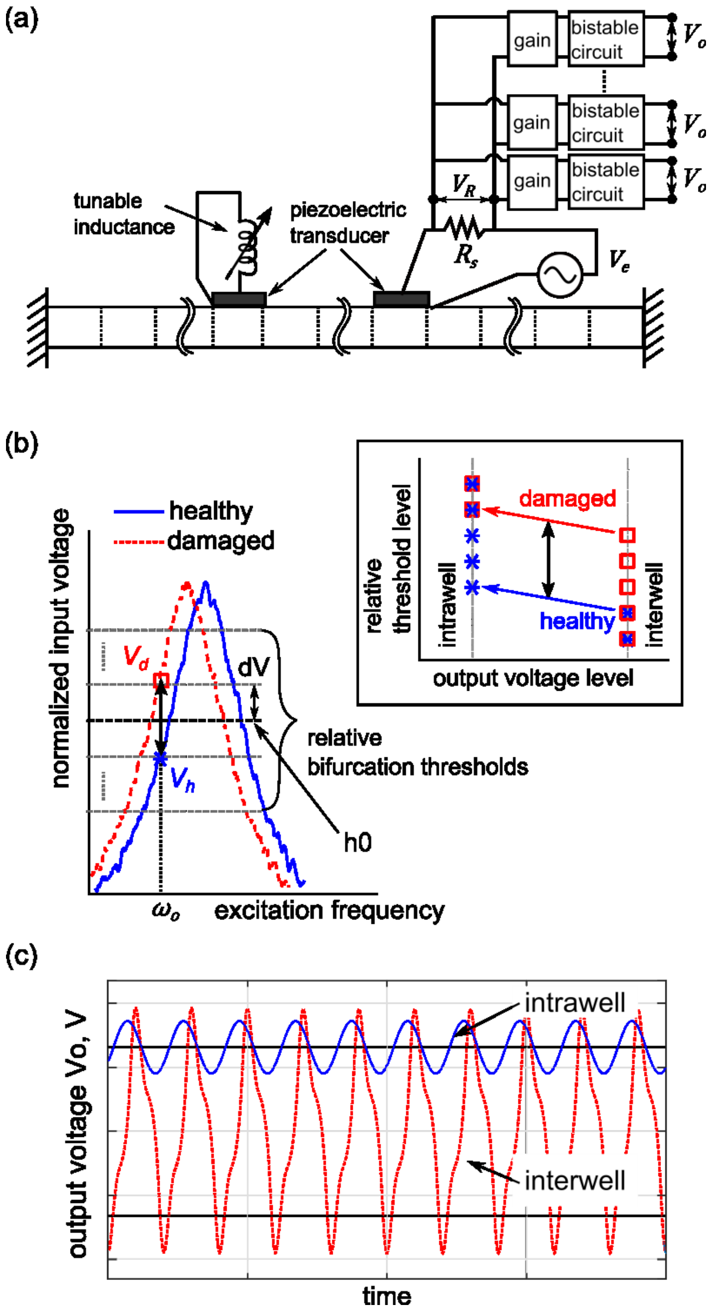

Figure 5.2. (a) Illustration of a structure integrated with bistable and adaptive piezoelectric circuitry. (b) Example of normalized input voltage levels of healthy and damaged structures. The right inset image shows a representative output voltage level profile with respect to the relative bifurcation threshold values determined by the input gain values of each bistable circuit for healthy and damaged structures. (c) Example bistable circuit output voltage time series for intrawell and interwell dynamics.

By capitalizing on the negligible backward coupling due to the characteristics of op-amp in the bistable circuit [103], one can apply the structural response at a single frequency as input to a network of identical bistable circuits in parallel, as presented in Figure 5.2(a). The input voltage amplitudes for each bistable circuit are then adjusted by systematically tuning the gain values so that the adjusted input amplitudes are sequentially located at relatively different levels within a range that encompasses the bifurcation threshold. By evaluating the output voltages of each bistable circuit whether they exhibit intra- or interwell oscillations and comparing the results for the healthy and damaged structures, the damage-induced impedance change can be accurately determined as will be described below. For example, when the healthy structural response is applied to a bistable circuit with relatively high gain value, the circuit may exhibit interwell oscillation as the input level become larger than the bifurcation threshold. On the other hand, the bistable circuit with relatively low gain value may show intrawell oscillation in the response. In this way, when the gain values for each bistable circuit are selected to be sequentially decreasing, the corresponding circuit responses initially exhibiting interwell oscillation will suddenly change to the intrawell since the relative bifurcation threshold value increases with respect to the input voltage level. The sudden change occurs at a certain bistable circuit where the relative threshold value exceeds the normalized input voltage level. As a result, one may obtain a digitized (either intra- or interwell oscillations) array of bistable circuit responses that exhibits a notable jump as presented in the inset of Figure 5.2(b). Repeating this process for the damaged structure may yield a similar array of responses but with a sudden jump at a bistable circuit with a different relative threshold value. As illustrated in the inset image of Figure 5.2(b), for relatively low (high) threshold values, the bistable circuit output voltage may exhibit interwell (intrawell) oscillations for both healthy and damaged structures; whereas bistable circuits having the relative threshold values between the input voltages from the healthy and damaged structures will show remarkably different output voltage levels for each structure. Therefore, the damaged-induced impedance change at the specific frequency can be determined from the notable difference between these digitized arrays for the healthy and damaged structures. By repeating this procedure for other frequencies, the piezoelectric impedance variations can be accurately quantified to be utilized in the damage identification routine presented in Section 5.2. Therefore, by utilizing the dramatic changes in the bistable circuit responses, we can measure minute impedance changes induced by small structural damages.

5.3.2. Gain Selection Strategy Considering Practical Implementation

The core principle of the proposed bifurcation-based sensing approach is based on tracking the onset of saddle-node bifurcation that induces dramatic change in the response level. On the other hand, it is well known that saddle-node bifurcation could be strongly affected by some influences that are unavoidable and ever-present in practical applications. For example, noise may yield a distribution of premature bifurcation points [116–118] that activate bifurcation even before the governing parameter reaches the deterministic bifurcation threshold, while non-stationarity of the bifurcation parameters may delay the onset of bifurcation [119,120]. As a result, it is critical to distinguish whether the bifurcation is activated due to actual damage-related structural changes or the noise and nonstationary influences to successfully implement the advanced BB sensing approach. Therefore, in this section such statistical characteristics of the bifurcation points are theoretically investigated and incorporated to strategically selecting the gain values for BB sensing in practical applications.

In this research, the target structure is harmonically excited at frequency ω_o with increasing amplitude up to V_e at a rate of μ_e. The structural response obtained by voltage drop V_R across the resistor R_s with additive Gaussian white noise is applied as input voltage V_i to the array of bistable circuits following gain adjustments. The stochastic and non-stationary influences on the activation of classical smooth saddle-node bifurcations can be investigated by utilizing the stochastic normal form of dynamic saddle-node bifurcation, which is a simplified form that describes the system dynamics local to the bifurcating point [125,126]. Since the bistable circuit exhibits non-smooth dynamical behavior due to the nonlinear feedback loop among an op-amp and a pair of diodes, we develop a normal form of non-smooth saddle-node bifurcation to examine the local dynamics near the bifurcation point:

$$z' = \tau + |z| + \alpha\xi. \tag{5.7}$$

where z is a scaled output voltage of the bistable circuit, $(\ )'$ indicates differentiation with respect to scaled time τ, and α is scaled noise level according to the sweep rate. ξ is Gaussian white noise with autocorrelation $\langle \xi(t)\xi(\tilde{t})\rangle = 2\delta(t-\tilde{t})$. By solving the well-known Kramer's rate [116] corresponding to the normal form (5.7) with a straight forward back-calculation, we can theoretically estimate the distribution of input voltage amplitudes V_{esc} that trigger the non-smooth saddle-node bifurcation for given noise and sweep conditions, which will be utilized for determining the gain values. Detailed derivation can be found in Chapter 4.

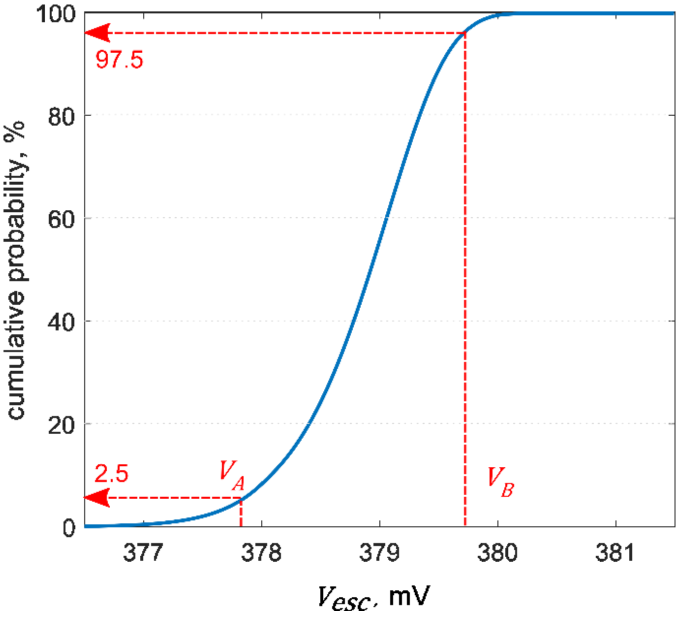

Figure 5.3. Cumulative probability distribution of bifurcation points.

Figure 5.3 shows an example of the theoretically estimated cumulative probability distribution of bifurcation points in the bistable circuit when the input sweep rate is 4 V/s and the standard deviation of the measurement noise is 10 mV. The horizontal axis is the input voltage amplitude and the cumulative probability is provided along the vertical axis. If the gain value is designed such that the input voltage amplitude V_i is swept up to V_A in Figure 5.3, which is approximately two standard deviations $SD\langle V_{esc}\rangle$ below the mean value $\langle V_{esc}\rangle$, the bistable circuit will undergo saddle-node bifurcation from intra- to interwell oscillations with 2.5 % probability. In other words, the bistable circuit will have 97.5 % probability to exhibit intrawell oscillation. On the other hand, gain value selected to sweep the input amplitude up to V_B point, which is on the opposite side of the mean value, may induce interwell oscillation in the response with a probability of 97.5 %. In other words, the input amplitude increase from V_A to V_B may activate saddle-node bifurcation with approximately 95% probability. Therefore, in this research the gain values are determined such that the input voltage amplitudes $V_i = G_n V_R$ for each bistable circuit are sequentially separated by 4 standard deviations of the escape voltage distribution, which results in

$$G_n = \frac{\langle V_{esc}\rangle - (4n-2) SD\langle V_{esc}\rangle}{V_R} \tag{5.8}$$

where G_n the gain value for the n-th bistable circuit in the array. As a result, the damage-induced change of structural response amplitude ΔV_R can be determined by comparing whether the bifurcation has occurred in each bistable circuit for the healthy and damaged structures. For example, if the bifurcation has occurred at the p-th and q-th circuits of the array for the healthy and damaged structures, respectively, yielding significant jump in the response amplitude as illustrated in the inset of Figure 5.2(b), the difference in the bistable circuit response array can be mapped to the corresponding damage-induced structural response change as

$$\Delta V_R \approx \frac{4(q-p)\, SD\langle V_{esc}\rangle}{G_0} \tag{5.9}$$

Finally, the damage-induced admittance (inverse of the impedance) change ΔY can be determined as Eq. (5.10) and be utilized for damage prediction with the identification algorithm presented in the Section 5.2.

$$\Delta Y = \frac{1}{R} \frac{\Delta V_R}{V_e} \tag{5.10}$$

Therefore, by incorporating the theoretically estimated bifurcation statistics into developing a bifurcation-based sensing strategy, the impedance variations can be accurately determined via monitoring the dramatic changes in the response levels of the bistable circuit array.

5.4. Numerical Investigations

5.4.1. Case Study: Damage Identification under Noise Influences

In this section, a numerical case study is conducted to verify the proposed damage identification approach by using a beam structure model integrated with bistable and adaptive piezoelectric circuitry shown in Figure 5.2(a). A fixed-fixed beam structure evenly discretized into 31 elements is integrated with piezoelectric transducers at the 3rd and 21st elements, which are respectively connected to a tunable inductor for data enrichment and a bistable circuitry network for impedance change measurement. Damage is represented by 1 % and 1.5 % structural stiffness reductions at the 13th and 24th elements, respectively. Since the damage effect is more significant near the resonance peaks, the impedance changes are assessed at 5 frequencies around each resonance frequency for damage identification. Then, the inductances are tuned for each resonance in the frequency range of 5 kHz to 11 kHz following the procedure introduced in [75,151]. The proposed bifurcation-based sensing approach is implemented by numerically solving the governing equation in Eqs. (5.11) and (5.12), which is derived assuming ideal op-amp characteristics and the Shockley's diode model [149],

$$L\frac{\mathrm{d}I_L}{\mathrm{dt}} = (k-1)V_D - I_L R - 2R_3 I_s \, sinh\left(\frac{V_D}{\eta V_T}\right) + (1-k)V_i \tag{5.11}$$

$$C\frac{\mathrm{d}V_D}{\mathrm{dt}} = \frac{I_L - 2I_s \, sinh\left(\frac{V_D}{\eta V_T}\right)}{\frac{2R_3 I_s}{\eta V_T} cosh\left(\frac{V_D}{\eta V_T}\right)+1} \tag{5.12}$$

where L, C, and R are the bistable circuit inductance, capacitance, and resistance, respectively. V_D, η, V_T, and I_s represent voltage drop over an open diode, ideality factor, thermal voltage, and reverse bias saturation current of the diode, respectively. V_i and I_L

respectively indicate the input voltage and the current flowing through the inductor. The feedback gain is $k = 1 + R_2/R_1$. The output voltage V_o can be derived as $V_o = V_D + 2R_3I_s \sinh(V_D/\eta V_T)$. Since it is well known that the double-well Duffing oscillator exhibits non-unique steady-state dynamics, especially near its principle resonance frequency [103,152], the bistable circuit parameters are designed such that the harmonic excitation frequency is much lower than the principle resonance frequency in order to reliably activate the saddle-node bifurcation. Relevant parameters of the integrated system are listed in Table 5.1. In this case study, Gaussian white noise with standard deviation of 10 mV (approximately 28 dB signal-to-noise ratio) is added to the input signal prior to gain adjustments. The gain values are determined based on the procedure described in Section 5.3 for the given noise level. Figure 5.4 shows the measurement error distribution of damage-induced piezoelectric admittance changes determined by the (a) conventional method that compares the spectral amplitudes of the healthy and damaged structural responses and (b) proposed approach utilizing the bistable circuit network. It is clearly observed that the proposed method provides significantly enhances the measurement accuracy by more than 300 % compared to the conventional approach by decreasing the standard deviation of measurement error from approximately 4.9×10^{-6} to 1.6×10^{-6}.

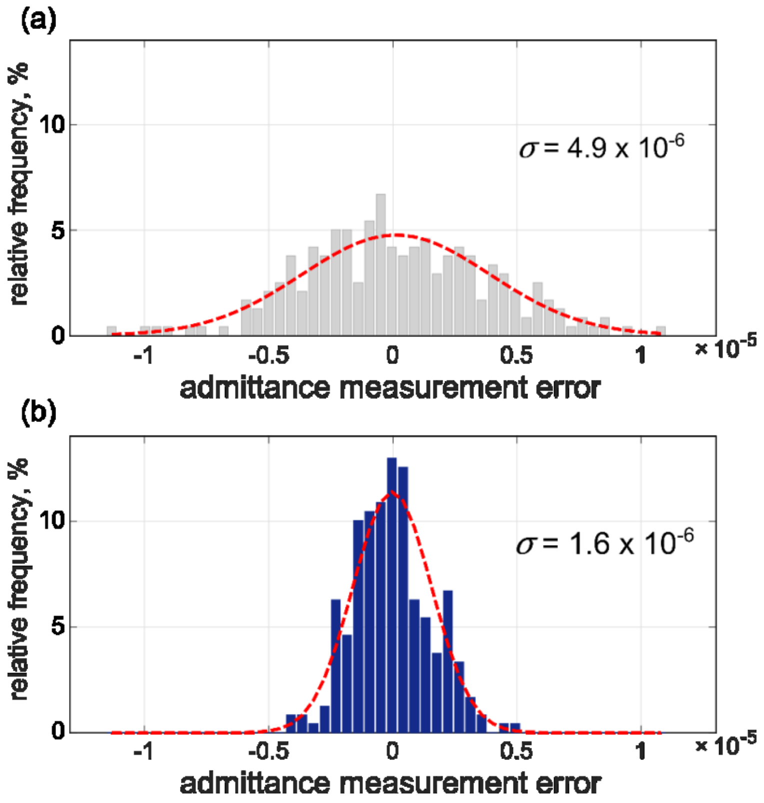

Figure 5.4. Distributions of admittance change measurement errors obtained by the (a) conventional and (b) proposed approaches. Standard deviations are given alongside the Gaussian fits to each distribution plotted as dashed lines.

Figure 5.5 presents the damage location and severity identification results. The horizontal axis indicates the element number and the predicted damage severity (elemental stiffness reduction) is provided along the vertical axis. The dashed boxes indicate the actual location and severity of the damages introduced in this case study. When the conventional approach is applied to measure the impedance change without utilizing the adaptive piezoelectric circuitry for data enrichment, the damaged elements are falsely identified with the largest damage of 5.1 % stiffness reduction at the 23rd element as shown in Figure 5.5(a). On the other hand, Figure 5.5(b) shows that applying the data enrichment approach to the damage-induced impedance changes obtained by the conventional method improves the damage prediction. It can be observed that the damage at the 24th element with 1.5 % stiffness reduction is approximately predicted, yet damage at the 13th element is not identified correctly. Since structural health monitoring systems may not distinguish false alarms from accurate damage identification, such incorrect prediction may mislead subsequent corrective measures. In contrast, when the proposed bistable and adaptive piezoelectric circuitry is employed, damage identification results accurately pinpoint the location and severity of damages under noise influences as shown in Figure 5.5(c).

Table 5.1. System parameters.

<table>
<tr><td colspan="4">Beam structure</td><td colspan="4">Piezoelectric transducer</td></tr>
<tr><td colspan="2">Length × Thickness × Width, mm</td><td colspan="2">607.8 × 7.62 × 3.175</td><td colspan="2">Length × Thickness × Width, mm</td><td colspan="2">17 × 7.62 × 0.191</td></tr>
<tr><td colspan="2">Young’s modulus, GPa</td><td colspan="2">73.4</td><td colspan="2">Young’s modulus, GPa</td><td colspan="2">66</td></tr>
<tr><td colspan="2">Density, kg/m^3</td><td colspan="2">2780</td><td colspan="2">Density, kg/m^3</td><td colspan="2">7800</td></tr>
<tr><td colspan="2">Loss factor, %</td><td colspan="2">0.15</td><td colspan="2">Permittivity, F/m</td><td colspan="2">1.6×10^{-8}</td></tr>
<tr><td colspan="2">Poisson’s ratio</td><td colspan="2">0.33</td><td colspan="2">Piezoelectric constant, m/V</td><td colspan="2">-190×10^{-12}</td></tr>
<tr><td colspan="4">Bistable circuit</td><td colspan="4">Inductance values for data enrichment</td></tr>
<tr><td>L, uH</td><td>10</td><td>R_3, kΩ</td><td>2</td><td>L_1, mH</td><td>134.6</td><td>L_5, mH</td><td>56.4</td></tr>
<tr><td>C, nF</td><td>40</td><td>I_s, nA</td><td>4.352</td><td>L_2, mH</td><td>106.4</td><td>L_6, mH</td><td>46.6</td></tr>
<tr><td>R, Ω</td><td>30</td><td>η</td><td>1.906</td><td>L_3, mH</td><td>85.1</td><td>L_7, mH</td><td>38.8</td></tr>
<tr><td>$\boldsymbol{R_1}$, $\boldsymbol{R_2}$, k Ω</td><td>1</td><td>V_T, mV</td><td>26</td><td>L_4, mH</td><td>68.9</td><td>L_8, mH</td><td>32.6</td></tr>
</table>

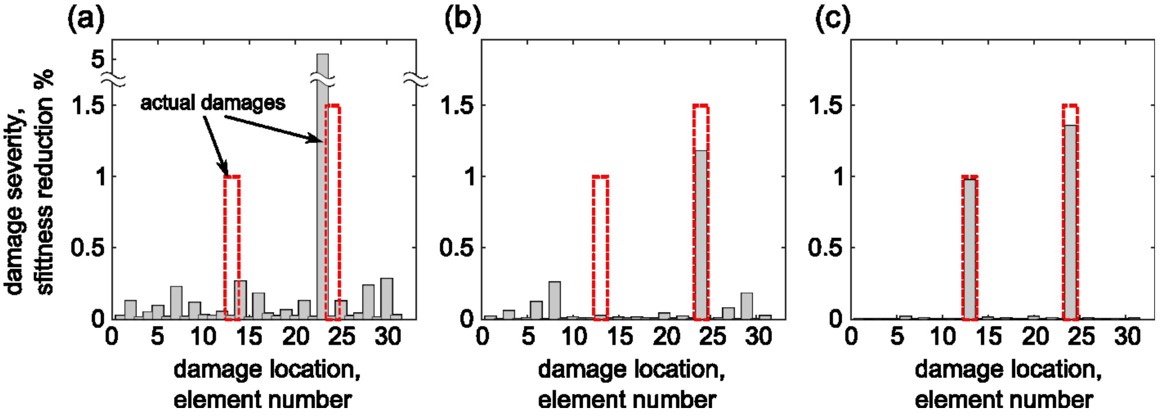

Figure 5.5. Damage identification results obtained by using (a) conventional method, (b) adaptive piezoelectric circuitry only, and (c) integrated bistable and adaptive piezoelectric circuitry

5.4.2. Damage Identification Study for Various Damage Profiles

The prior section presented damage identification results for a single case with damages at two locations of the structure. It was found that utilizing the proposed approach significantly improved the damage identification performance under realistic noise influences, which otherwise greatly degrades the viability of damage identification. In this section, we examine the reliability of the proposed approach by further extending the numerical investigation of damage identification for various damage profiles with different numbers and severities, while keeping other conditions the same as Section 5.4.1. The damage is assumed to be located at from one to three different locations of the beam structure with four different severities (0.5, 1, 1.5, and 2% local stiffness reduction). The damage identification routine is performed for 924 different cases of damage profiles including 124 conditions of single damage and 400 conditions for two and three damages, respectively, which are randomly selected out of their total possible combinations. The root mean square deviation (RMSD) between the actual $\mathbf{d}^{actual}$ and identified $\hat{\mathbf{d}}$ damages is employed to quantify the damage prediction error and compare the performance of damage identification.

$$RMSD = \sqrt{\frac{\sum_{i=1}^{N}\left(\hat{d}_i - d_i^{actual}\right)^2}{\sum_{i=1}^{N} {d_i^{actual}}^2}} \tag{5.13}$$

where $\hat{d}_i$, d_i^{actual} are the predicted and actual damage indices of the i-th element, respectively.

Figure 5.6 compares the distributions of damage prediction errors obtained by utilizing the (a) conventional and (b) proposed methods. The damage prediction error is presented along the vertical axis and the horizontal shows its relative frequency. The first and third quartiles of the distributions are indicated by dashed lines with numerical values

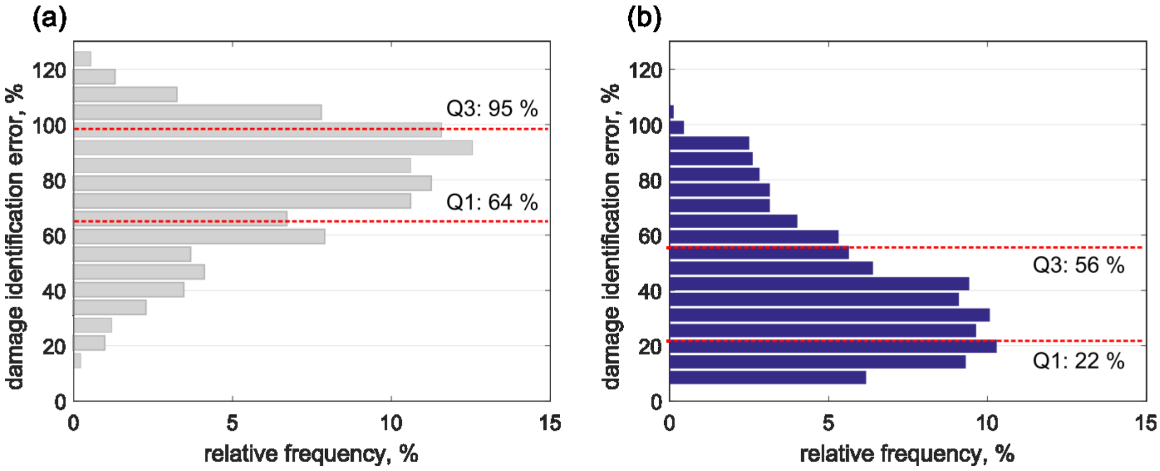

Figure 5.6. Distributions of damage identification errors obtained by using the (a) conventional and (b) proposed methods. Dashed lines included in both plots indicate the first (Q1) and third (Q3) quartiles of each distribution, respectively.

given alongside. It is seen that the damage prediction result is greatly improved by employing the proposed approach, where the modes with maximum relative frequency and medians of the error distributions decrease from approximately 92 % and 81 % to 20 % and 36 %, respectively. From these results, it can be concluded that the proposed method utilizing the bistable and adaptive piezoelectric circuitry significantly enhances the reliability of damage identification under noise influences.

5.5. Experimental Investigation

Experimental damage interrogation on an aluminum beam structure (Al-2024) is performed to validate the effectiveness of the proposed approach. The experimental configuration is shown in Figure 5.7(a). The damage is introduced by a surface notch at the 25th element of the beam structure discretized into 61 elements. The notch is 0.09 mm deep and 10.4 mm long, which may result in approximately 8.3 % reduction of the local bending stiffness [78]. The piezoelectric transducers (PSI-5A4E) attached on the top surface of the 29th and 41st elements are connected to a tunable inductor for impedance data enrichment and a bistable circuit for impedance measurement, respectively. By strategically selecting the inductance values of a synthetic inductor that consists of op-amps (LM324), resistors, and capacitors (Figure 5.7(b)) [89], the dynamics of the electromechanically coupled system are favorably altered to obtain an enriched data set of damage-induced impedance change measurements. The dimensions of the beam structure and piezoelectric transducers and the circuitry parameter values of the synthetic inductor and the bistable circuit are provided in Table 5.2.

The proposed bifurcation-based sensing method may be implemented in two ways: parallel and iterative methods. Figure 5.2(a) shows an example of the parallel approach where the structural response measured by the piezoelectric transducer effectively becomes input to a network of bistable circuits in parallel to examine whether each bistable circuit exhibited intra- or interwell oscillations. On the other hand, in this study we have employed the iterative method with a single bistable circuit to realize the proposed sensing algorithm for damage identification as shown in Figure 5.7(a). The electromechanically coupled system is harmonically excited with amplitudes swept in a

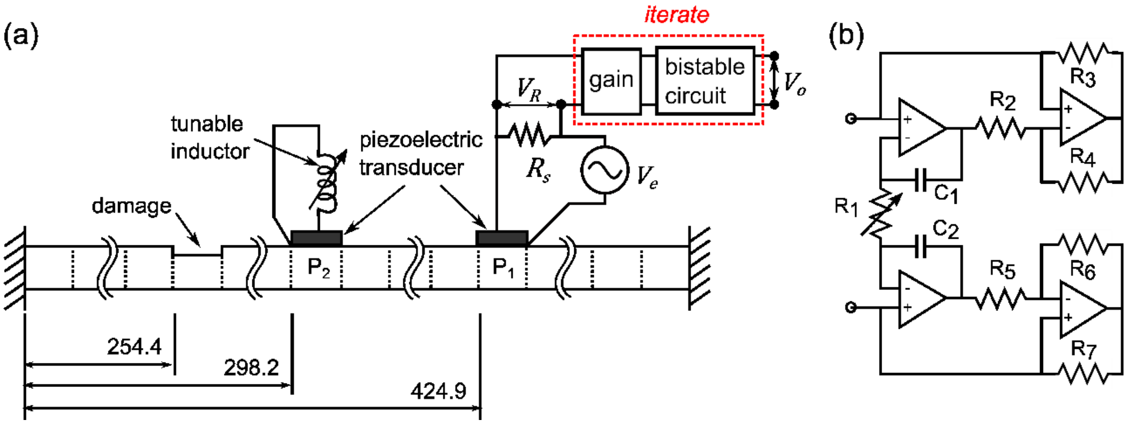

Figure 5.7. (a) Configuration of the experimental beam structure integrated with bistable and adaptive piezoelectric circuitry (distances given in millimeters). (b) Schematic illustration of the synthetic inductor.

Table 5.2. Experimental system parameters.

Beam, mm	627.2 × 7.21 × 3.175		P_1, mm	16.85 × 7.09 × 0.191		P_2, mm	16.3 × 7.09 × 0.191	
Circuitry element	C_1, nF	C_2, nF	R_2, Ω	R_3, Ω	R_4, Ω	R_5, Ω	R_6, Ω	R_7, Ω
	9.788	9.807	4620	4629	4629	4628	4632	4629
	L, mH	39.45	40.367	41.272	45.32	46.16	63.1	80.12
	R_1, Ω	850	870	890	980	1000	1371	1750

rate of 4 V/s, and the resulting the structural response measured by voltage drop across the resistor is iteratively fed to the bistable circuit following gain adjustments that corresponding to the sequentially selected values in the parallel method. In order to account for measurement noise in practice, Gaussian white noise with standard deviation of 50 mV (approximately 15 dB signal-to-noise ratio) is applied to the input signal prior to the gain adjustments. The gain values are selected according to the guideline presented in Section 5.2 such that the relative levels of the bifurcation threshold are separated by four standard deviations of the estimated escape distribution. For each iteration, the bistable circuit response is evaluated for whether it exhibited intra- or interwell oscillations. The two methods should provide equal sensing performance when the strategies are correctly performed. Since the damage is introduced as a surface notch in the experiment, the damage indices are restricted to have positive coefficients in the inverse algorithm assuming stiffness reduction.

The damage prediction results obtained by the conventional method and the new approach utilizing bistable circuitry are presented in the left (a, b) and right (c, d) columns of Figure 5.8, respectively. The damage identification routines are carried out for 10 runs, and the averaged results (local stiffness reductions in each element) are plotted in Figure 5.8(a,c) where the vertical axis indicates the element number and the number of inductance tunings are provided along the horizontal axis. For both measurement methods, the damage prediction results indicate wrong location when the data enrichment technique is not applied where the number of inductance tunings is one. However, as the number of inductance tunings increases, the damage identification results based on the proposed approach converge to the correct location and finally pinpoint damage at the 25th element with 7.3 % stiffness reduction, close to the actual value of 8.3%. In contrast, although the damage predictions from the conventional method converge around the actual damage location, the final damage is predicted to be 5 % stiffness reduction at the 25th element. The damage identification errors plotted in Fig 8(b,d) further exemplify the effectiveness of the proposed method. The damage identification errors (RMSD) of the ten individual results (dashed line) are presented as a function of the number of inductance tunings. The mean values are shown in solid line with first standard deviations indicated by error bars. For both measurement methods, the damage identification errors show decreasing trends as the number of inductance tuning increases, which demonstrates the effectiveness of data enrichment strategy utilizing the adaptive piezoelectric circuitry. On the other hand, the deviations of the prediction errors determined by the proposed method remain small and the final prediction error is 38%, while the conventional method yields large deviations in the prediction errors and its final prediction error is 73 %, approximately twice of the proposed method. Overall, the experimental results support and verify that the proposed approach utilizing the integrated bistable and adaptive piezoelectric circuitry enables accurate and robust damage identification under noise contamination.

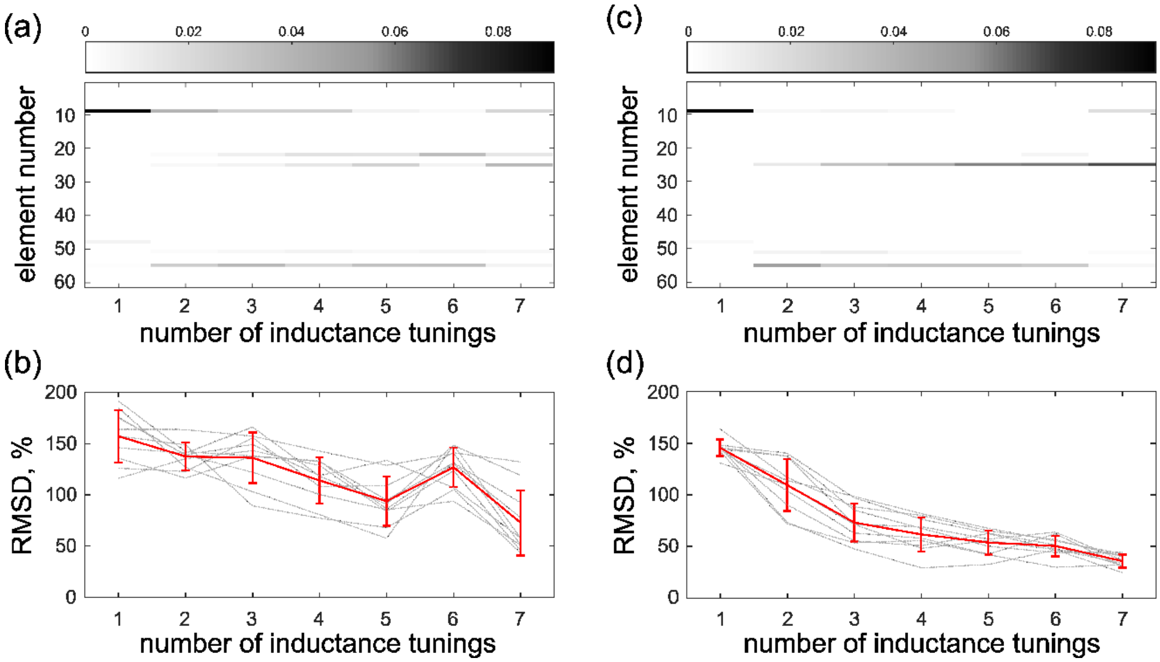

Figure 5.8. Experimental damage identification results obtained by the conventional and new bifurcation approaches are presented in columns (a, b) and (c, d), respectively. Figure (a, c) show the damage identification results and the corresponding damage prediction errors (RMSD) are plotted in (b, d) with respect to the number of inductance tunings.

5.6. Summary and Conclusion

This chapter investigates a novel approach that utilizes an integrated bistable and adaptive piezoelectric circuitry to enhance the robustness and accuracy of electromechanical impedance-based damage identification. By changing the dynamic characteristics of the integrated system using adaptive piezoelectric circuitry, we can obtain a significantly increased number of impedance changes with respect to identical damage profile, which are accurately measured by monitoring the bifurcation activations in the bistable circuit array. As a result, the measurement method and the underdetermined inverse problem for damage identification are fundamentally improved to provide much more robust damage predictions against noise and measurement error. Numerical and experimental case studies have successfully verified that the impedance change measurements and the resulting damage identification performance are significantly enhanced by utilizing the proposed approach. Overall, the results of this chapter demonstrate the potential of implementing the advanced bifurcation-based sensing approach, not only for the impedance-based SHM to provide a new robust pathway in practical implementations, but also for a broad range of sensing and identification applications that are exposed to noise problem.

CHAPTER 6

Scholarly Contributions, Broader Impacts, and Recommendations

6.1. Summary of Scholarly Contributions and Broder Impacts

This research aims to extend the potential of the piezoelectric impedance-based damage identification approaches by developing a new methodology that improves the severely underdetermined inverse problem for accurate damage identification, and by introducing a novel approach that can accurately determine the damage-induced piezoelectric impedance variations under environmental noise and damping influences. The scholarly contributions and broader impacts of this thesis work are summarized below.

- The data enrichment concept developed in this thesis addresses the critical limitation of seriously underdetermined inverse problem for piezoelectric impedance-based damage identification. The impedance measurements are significantly enriched with respect to same structural defect by integrating the adaptive piezoelectric circuitry with monitored structure and selectively tuning the inductance values in the circuitry. The enriched data sets are then utilized to improve the rank deficiency of the inverse problem. This idea of data enrichment using adaptive piezoelectric circuity not only enhances the accuracy and robustness of impedance-based damage identification but also shows new insights into strategically employing multi-physics couplings to fundamentally address various underdetermined inverse problem formulations.

- This research advances the state of the art by developing a new bifurcation-based sensing strategy utilizing bistable circuits. The results demonstrate excellent potential of this approach that can accurately determine the damage-induced piezoelectric impedance variations under environmental noise and dissipation. It is found that the integration of bistable and adaptive piezoelectric circuitry even further enhances the accuracy and robustness of the impedance model-based damage identification which are otherwise compromised. The novel sensing strategy utilizing bistable circuit and its design criteria are expected to have broader impact since the bistable circuit is the key element to extend the applicability of the advanced bifurcation-based sensing method from microscale to a wide range of meso-/macroscale systems that are exposed to noise problem.
- The theoretical investigation on the dynamic and stochastic activation of saddle-node bifurcation is aimed to improve the accuracy in determining the onset of saddle-node bifurcation since the core principle of the bifurcation-based sensing approach is based on tracking the bifurcation activation points. The results not only enhance the performance of bifurcation-based sensing

scheme, but also derive new insights for estimating the sensing limit of bifurcation-based sensing approaches under noise and non-stationary influences. Furthermore, the rigorous theoretical framework developed based on the stochastic normal form of saddle-node bifurcation in non-smooth dynamical systems provides important scholarly contributions to the fundamental understanding of how various non-smooth and nonlinear dynamical systems exhibit saddle-node bifurcations under noise and non-stationary influences. It is expected that these findings will provide a straightforward and accurate means for estimating critical conditions that lead to sudden large jumps in the response of various practical contexts associated with non-smooth saddle-node bifurcation where noise is ever-present.

Overall, this thesis makes an important impact to advance the state of the art impedance-based SHM by addressing the two major limitations based on the literature review in Chapter 1, and is expected to aid the transition of the impedance-based approaches into more reliable implementation in SHM applications.

6.2. Recommendations for Future Work

This thesis has developed a novel methodology that fundamentally improves the underdetermined inverse problem of the piezoelectric impedance model-based damage identification approach by tailoring adaptive piezoelectric circuitry, and a new sensing platform that enables unprecedented sensing resolution using nonlinear bifurcation phenomena in bistable circuits. The escape statistics of saddle-node bifurcation in non-smooth dynamical systems is theoretically estimated to further improve the accuracy in determining the onset of bifurcations under stochastic and non-stationary influences. These advancements were leveraged to significantly enhance the accuracy and robustness of piezoelectric impedance-based structural health monitoring. Nonetheless, the current state of the art still has room for improvements to achieve more reliable SHM implementations and opportunities to extend the insights gained in this thesis. This chapter lays out the author's recommendations for important areas of future work.

Despite the advancements, transitioning SHM from laboratory settings to real structures yet remains a challenge in comparison to its great importance. In particular, major challenges in real world implementation include uncertainties from various sources, which significantly compromise the reliability of damage identification. Therefore, it is recommended that future research effort focus on further developing sensing and modeling approaches to reduce these uncertainties. A comprehensive approach that accurately quantifies and effectively utilizes the uncertainties is required to enhance the reliability of damage identification. Furthermore, since it is obvious that a certain sensor or actuator cannot have unlimited coverage area, the author perceives that it is critical to develop a strategy that synthesizes a robust sensor network to fully capitalize on the potential of the new sensing platform and damage identification algorithm developed in this thesis. Sensor networking strategies that satisfy both requirements of SHM and wireless network design with redundant coverage will have great potential in not only enhancing the reliability of damage diagnosis but also realizing sensor self-diagnosis and robust decision making.

This thesis has developed a rigorous theoretical framework that estimates the statistical characteristics of saddle-node bifurcation activation under ever-present noise and non-stationary influences. This insight is not limited to developing bifurcation-based sensing techniques. Sudden drastic transitions in the dynamics of complex nonlinear systems are often observed in various fields of, for example, aeroelasticity of aircraft [153], power grids [154], ecological [112,155] and climate [112,114] systems, and financial markets [156]. Accurately predicting the onset of these transitions in advance is crucial for understanding how to utilize or prevent the dramatic and sudden changes that these systems undergo. Therefore, it is recommended to extend the insights gained in this thesis to explore novel methods to quantitatively forecast the activation of these transitions. For example, the theoretical framework developed in this thesis for predicting the saddle-node bifurcations will be a foundation for analyzing the cascaded critical transitions in the interconnected complex systems.

BIBLIOGRAPHY

[1] Inman D J, Farrar C R, Junior V L and Junior V S 2005 *Damage Prognosis: For Aerospace, Civil and Mechanical Systems* ed D J Inman, C R Farrar, V L Junior and V S Junior (Hoboken: John Wiley & Sons Ltd)

[2] Balageas D 2006 Introduction to Structural Health Monitoring *Structural Health Monitoring* ed D Balageas, C-P Fritzen and A Güemes (London: ISTE Ltd.) pp 13–43

[3] Rytter A 1993 *Vibration-Based Inspection of Civil Engineering Structures* (Aalborg University, Denmark)

[4] Farrar C R, Doebling S W and Nix D A 2001 Vibration-Based Structural Damage Identification *Philos. Trans. R. Soc. London. Ser. A Math. Phys. Eng. Sci.* **359** 131–49

[5] Carden E P and Fanning P 2004 Vibration Based Condition Monitoring: A Review *Struct. Heal. Monit.* **3** 355–77

[6] Fan W and Qiao P 2011 Vibration-based Damage Identification Methods: A Review and Comparative Study *Struct. Heal. Monit.* **10** 83–111

[7] Salawu O S 1997 Detection of Structural Damage through Changes in Frequency: A Review *Eng. Struct.* **19** 718–23

[8] Kim J-T, Ryu Y-S, Cho H-M and Stubbs N 2003 Damage Identification in Beam-Type Structures: Frequency-Based Method vs Mode-Shape-Based Method *Eng. Struct.* **25** 57–67

[9] Jiang L J, Tang J and Wang K W 2006 An Enhanced Frequency-shift-based Damage Identification Method Using Tunable Piezoelectric Transducer Circuitry *Smart Mater. Struct.* **15** 799–808

[10] Shi Z Y, Law S S and Zhang L M 2000 Damage Localization by Directly Using Incomplete Mode Shapes *J. Eng. Mech.* **126** 656–60

[11] Lee J J, Lee J W, Yi J H, Yun C B and Jung H Y 2005 Neural Networks-Based Damage Detection for Bridges Considering Errors in Baseline Finite Element Models *J. Sound Vib.* **280** 555–78

[12] Pandey A K, Biswas M and Samman M M 1991 Damage Detection from Changes in Curvature Mode Shapes *J. Sound Vib.* **145** 321–32

[13] Hamey C S, Lestari W, Qiao P and Song G 2004 Experimental Damage Identification of Carbon/Epoxy Composite Beams Using Curvature Mode Shapes *Struct. Heal. Monit.* **3** 333–53

[14] Lestari W, Qiao P and Hanagud S 2006 Curvature Mode Shape-based Damage Assessment of Carbon/Epoxy Composite Beams *J. Intell. Mater. Syst. Struct.* **18** 189–208

[15] Raghavan A and Cesnik C E S 2007 Review of guided-wave structural health monitoring *Shock Vib. Dig.* **39** 91–114

[16] Sohn H, Park G, Wait J R, Limback N P and Farrar C R 2004 Wavelet-based Active Sensing for Delamination Detection in Composite Structures *Smart Mater. Struct.* **13** 153–60

[17] Liu Z, Sun K, Song G, He C and Wu B 2015 Damage Localization in Aluminum Plate with Compact Rectangular Phased Piezoelectric Transducer Array *Mech. Syst. Signal Process.* **10** 1–12

[18] Ihn J and Chang F 2004 Detection and Monitoring of Hidden Fatigue Crack Growth Using a Built-in Piezoelectric Sensor/Actuator Network: II. Validation Using Riveted Joints and Repair Patches *Smart Mater. Struct.* **13** 621–30

[19] Diamanti K, Soutis C and Hodgkinson J M 2005 Non-destructive Inspection of Sandwich and Repaired Composite Laminated Structures *Compos. Sci. Technol.* **65** 2059–67

[20] Lemistre M and Balageas D 2001 Structural Health Monitoring System Based on Diffracted Lamb Wave Analysis by Multiresolution Processing *Smart Mater. Struct.* **10** 504–11

[21] Kim Y-H, Kim D-H, Han J-H and Kim C-G 2007 Damage Assessment in Layered Composites Using Spectral Analysis and Lamb Wave *Compos. Part B Eng.* **38** 800–9

[22] Tua P S, Quek S T and Wang Q 2004 Detection of Cracks in Plates Using Piezo-actuated Lamb Waves *Smart Mater. Struct.* **13** 643–60

[23] Park G, Sohn H, Farrar C R and Inman D J 2003 Overview of Piezoelectric Impedance-

Based Health Monitoring and Path Forward *Shock Vib. Dig.* **35** 451–63

[24] Annamdas V and Soh C K 2010 Application of Electromechanical Impedance Technique for Engineering Structures: Review and Future Issues *J. Intell. Mater. Syst. Struct.* **21** 41–59

[25] Annamdas V and Radhika M A 2013 Electromechanical Impedance of Piezoelectric Transducers for Monitoring Metallic and Non-metallic Structures: A Review of Wired, Wireless and Energy-harvesting Methods *J. Intell. Mater. Syst. Struct.* **24** 1021–42

[26] Liang C, Sun F P and Rogers C A 1994 Coupled Electro-Mechanical Analysis of Adaptive Material Systems -- Determination of the Actuator Power Consumption and System Energy Transfer *J. Intell. Mater. Syst. Struct.* **5** 12–20

[27] Peairs D M, Park G and Inman D J 2004 Improving Accessibility of the Impedance-Based Structural Health Monitoring Method *J. Intell. Mater. Syst. Struct.* **15** 129–39

[28] Lynch J P and Loh K J 2006 A Summary Review of Wireless Sensors and Sensor Networks for Structural Health Monitoring *Shock Vib. Dig.* **38** 91–128

[29] Sun F P, Chaudhry Z, Liang C and Rogers C A 1995 Truss Structure Integrity Identification Using PZT Sensor-Actuator *J. Intell. Mater. Syst. Struct.* **6** 134–9

[30] Park G, Cudney H H and Inman D J 2000 Impedance-Based Health Monitoring of Civil Structural Components *J. Infrastruct. Syst.* **6** 153–60

[31] Yang Y, Liu H, Annamdas V and Soh C K 2009 Monitoring Damage Propagation Using PZT Impedance Transducers *Smart Mater. Struct.* **18** 45003

[32] Wang X and Tang J 2010 Damage Detection Using Piezoelectric Admittance Approach with Inductive Circuitry *J. Intell. Mater. Syst. Struct.* **21** 667–76

[33] Wang X and Tang J 2010 An Enhanced Piezoelectric Impedance Approach for Damage Detection with Circuitry Integration *Smart Mater. Struct.* **19** 45001

[34] Zhou W and Zuo L 2012 Sensitivity-Enhanced Admittance-Based Structure Health Monitoring Using a Higher-Order Resonant Circuit *Smart Mater. Struct.* **21** 105023

[35] Ayres J W, Lalande F, Chaudhry Z and Rogers C a 1998 Qualitative Impedance-based Health Monitoring of Civil Infrastructures *Smart Mater. Struct.* **7** 599–605

[36] Soh C K, Tseng K K-H, Bhalla S and Gupta A 2000 Performance of Smart Piezoceramic Patches in Health Monitoring of a RC Bridge *Smart Mater. Struct.* **9** 533–42

[37] Park G, Cudney H H and Inman D J 2001 Feasibility of Using Impedance-based Damage Assessment for Pipeline Structures *Earthq. Eng. Struct. Dyn.* **30** 1463–74

[38] Giurgiutiu V, Zagrai A and Bao J 2002 Piezoelectric Wafer Embedded Active Sensors for Aging Aircraft Structural Health Monitoring *Struct. Heal. Monit.* **1** 41–61

[39] Giurgiutiu V, Zagrai A and Bao J 2004 Damage Identification in Aging Aircraft Structures with Piezoelectric Wafer Active Sensors *J. Intell. Mater. Syst. Struct.* **15** 673–87

[40] Cuc A, Giurgiutiu V, Joshi S and Tidwell Z 2007 Structural Health Monitoring with Piezoelectric Wafer Active Sensors for Space Applications *AIAA J.* **45** 2838–50

[41] Zagrai A N, Doyle D, Gigineishvili V, Brown J, Gardenier H and Arritt B 2010 Piezoelectric Wafer Active Sensor Structural Health Monitoring of Space Structures *J. Intell. Mater. Syst. Struct.* **21** 921–40

[42] Giurgiutiu V, Friedman H, Bender J, Borg T, Yost M J, Newcomb W, Black A, Bost J and Stewart C D 2004 Electromechanical Impedance Sensor for In Vivo Monitoring the Body Reaction to Implants *J. Investig. Surg.* **17** 257–70

[43] Bhalla S and Bajaj S 2008 Bone Characterization Using Piezo-Transducers as Bio-Medical Sensors *Strain* **44** 475–8

[44] Boemio G, Rizzo P and Nardo L De 2011 Assessment of Dental Implant Stability by Means of The Electromechanical Impedance Method *Smart Mater. Struct.* **20** 45008

[45] Lalande F, Rogers C A, Childs B and Chaudhry Z 1996 High-Frequency Impedance Analysis for NDE of Complex Precision Parts *Proceedings of the SPIE* vol 2717pp 237–43

[46] Wandowski T, Opoka S, Alinowski P M and Ostachowicz W 2015 The Performance of Three Electromechanical Impedance Damage Indicators on Structural Element with Bolted Joints *Proc. of NDT in Aerospace symposium, The e-Journal of Nondestructive Testing* vol 20

[47] Pavelko I, Pavelko V, Kuznetsov S and Ozolinsh I 2014 Bolt-joint Structural Health Monitoring by the Method of Electromechanical Impedance *Aircr. Eng. Aerosp. Technol.* **86** 207–14

[48] Giurgiutiu V, Reynolds A and Rogers C A 1999 Experimental Investigation of E/M Impedance Health Monitoring of Spot- Welded Structural Joints *J. Intell. Mater. Syst.*

Struct. **10** 802–12

[49] Annamdas V, Ian L S, Pang H L J and Soh C K 2014 Monitoring of Fatigue in Welded Beams Using Piezoelectric Wafer Based Impedance Technique *J. Nondestruct. Eval.* **33** 124–40

[50] Roth W and Giurgiutiu V 2017 Structural Health Monitoring of an Adhesive Disbond through Electromechanical Impedance Spectroscopy *Int. J. Adhes. Adhes.* **73** 109–17

[51] Dugnani R, Zhuang Y, Kopsaftopoulos F and Chang F-K 2016 Adhesive Nond-line Degradation Detection via a Cross-correlation Electromechanical Impedance–Based Approach *Struct. Heal. Monit.* **15** 650–67

[52] Zagrai A N and Giurgiutiu V 2002 Electro-Mechanical Impedance Method for Crack Detection in Thin Plates *J. Intell. Mater. Syst. Struct.* **12** 709–18

[53] Tseng K K-H and Naidu A S K 2002 Non-parametric Damage Detection and Characterization Using Smart Piezoceramic Material *Smart Mater. Struct.* **11** 317–29

[54] Rabelo D D S, Jr V S, Mendes R, Neto F and Lacerda H B 2017 Impedance-based Structural Health Monitoring and Statistical Method for Threshold-level Determination Applied to 2024-T3 Aluminum Panels under Varying Temperature *Struct. Heal. Monit.* **16** 365–81

[55] Koh Y L, Rajic N, Chiu W K and Galea S 1999 Smart Structure for Composite Repair *Compos. Struct.* **47** 745–52

[56] Malinowski P, Wandowski T and Ostachowicz W 2015 The Use of Electromechanical Impedance Conductance Signatures for Detection of Weak Adhesive Bonds of Carbon Fibre-reinforced Polymer *Struct. Heal. Monit.* **14** 332–44

[57] Wandowski T, Malinowski P H and Ostachowicz W M 2017 Temperature and Damage Influence on Electromechanical Impedance Method Used for Carbon Fibre-Reinforced Polymer Panels **28** 782–98

[58] Giurgiutiu V and Zagrai A 2005 Damage Detection in Thin Plates and Aerospace Structures with the Electro-Mechanical Impedance Method *Struct. Heal. Monit.* **4** 99–118

[59] da Silva S, Dias Junior M and Lopes Junior V 2008 Structural Health Monitoring in Smart Structures Through Time Series Analysis *Struct. Heal. Monit.* **7** 231–44

[60] Figueiredo E, Park G, Farinholt K M, Farrar C R and Lee J-R 2012 Use of Time-Series Predictive Models for Piezoelectric Active-Sensing in Structural Health Monitoring

Applications *J. Vib. Acoust.* **134** 41014

[61] Lynch J P 2005 Design of a Wireless Active Sensing Unit for Localized Structural Health Monitoring *Struct. Control Heal. Monit.* **12** 405–23

[62] Shin H, Yun C, Park G, Farinholt K M, Lee J, Park C, Jun S and Farrar C R 2012 Assessing Joint Integrity of a Lug Assembly Using Piezoelectric Active Sensors *Struct. Control Heal. Monit.* **19** 621–31

[63] Lopes Jr V, Park G, Cudney H H and Inman D J 2000 Impedance-Based Structural Health Monitoring with Artificial Neural Networks *J. Intell. Mater. Syst. Struct.* **11** 206–14

[64] Specht D F 1990 Probabilistic Neural Networks *Neural Networks* **3** 109–18

[65] Min J, Park S, Yun C-B, Lee C-G and Lee C 2012 Impedance-based Structural Health Monitoring Incorporating Neural Network Technique for Identification of Damage Type and Severity *Eng. Struct.* **39** 210–20

[66] Park G, Farrar C R, Rutherford A C and Robertson A N 2006 Piezoelectric Active Sensor Self-Diagnostics Using Electrical Admittance Measurements *J. Vib. Acoust.* **128** 469

[67] Baptista F G and Filho J V 2010 Optimal Frequency Range Selection for PZT Transducers in Impedance-based SHM Systems *Sensors Journal, IEEE* **10** 1297–303

[68] Xu Y and Liu G 2002 A Modified Electro-mechanical Impedance Model of Piezoelectric Actuator-sensors for Debonding Detection of Composite Patches *J. Intell. Mater. Syst. Struct.* **13** 389–96

[69] Bhalla S and Soh C K 2004 Electromechanical Impedance Modeling for Adhesively Bonded Piezo-Transducers *J. Intell. Mater. Syst. Struct.* **15** 955–72

[70] Fairweather J A and Craig K C 1998 Incorporating Finite Element Techniques to Simplify the Impedance Modeling of Active Structures *Proc. SPIE 3323, Smart Structures and Materials 1998: Mathematics and Control in Smart Structures* vol 3323pp 602–13

[71] Littlefield A G, Fairweather J A and Craig K C 2002 Use of FEA Derived Impedances to Design Active Structures *J. Intell. Mater. Syst. Struct.* **13** 377–88

[72] Lim Y Y and Soh C K 2014 Towards More Accurate Numerical Modeling of Impedance Based High Frequency Harmonic Vibration *Smart Mater. Struct.* **23** 35017

[73] Tseng K K, Wang L and Others 2005 Impedance-Based Method for Nondestructive Damage Identification *J. Eng. Mech.* **131** 58–64

[74] Alford R M, Kelly K R and Boore D M 1974 Accuracy of Finite-Difference Modeling of The Acoustic Wave Equation *Geophysics* **39** 834–42

[75] Jiang L J, Tang J and Wang K W 2008 On the Tuning of Variable Piezoelectric Transducer Circuitry Network for Structural Damage Identification *J. Sound Vib.* **309** 695–717

[76] Wang K W and Tang J 2008 *Adaptive Structural Systems with Piezoelectric Transducer Circuitry* (New York: Springer)

[77] Doyle J F 1989 *Wave Propagation in Structure: An FFT-based Spectral Analysis Methodology* (New York: Springer)

[78] Lee U and Shin J 2002 A Frequency-domain Method of Structural Damage Identification Formulated from Dynamic Stiffness Equation of Motion *J. Sound Vib.* **257** 615–34

[79] Lee U 2009 *Spectral Element Method in Structural Dynamics* (Singapore: John Wiley & Sons)

[80] Ritdumrongkul S, Abe M, Fujino Y and Miyashita T 2004 Quantitative Health Monitoring of Bolted Joints using a Piezoceramic Actuator–Sensor *Smart Mater. Struct.* **13** 20–9

[81] Lee U, Kim D and Park I 2013 Dynamic Modeling and Analysis of the PZT-Bonded Composite Timoshenko Beams: Spectral Element Method *J. Sound Vib.* **332** 1585–609

[82] Peairs D M, Inman D J and Park G 2007 Circuit Analysis of Impedance-based Health Monitoring of Beams Using Spectral Elements *Struct. Heal. Monit.* **6** 81–94

[83] Ritdumrongkul S and Fujino Y 2006 Identification of the Location and Level of Damage in Multiple-Bolted-Joint Structures by PZT Actuator-Sensors *J. Struct. Eng.* **132** 304–11

[84] Guo Z and Sun Z 2010 Impedance-based Damage Identification: A Numerical Study Using Spectral Elements *Proc. SPIE 7647, Sensors and Smart Structures Technologies for Civil, Mechanical, and Aerospace Systems* vol 7647p 76474A

[85] Wang X and Tang J 2009 Damage Identification Using Piezoelectric Impedance Approach and Spectral Element Method *J. Intell. Mater. Syst. Struct.* **20** 907–21

[86] Aster R C, Borchers B and Thurber C H 2012 *Parameter Estimation and Inverse Problems* (Waltham: Academic Press)

[87] Sirohi J and Chopra I 2000 Fundamental Understanding of Piezoelectric Strain Sensors *J. Intell. Mater. Syst. Struct.* **11** 246–57

[88] Friedman Z and Kosmatka J B 1993 An Improved Two-node Timoshenko Beam Finite Element *Comput. Struct.* **47** 473–81

[89] Chen W-K 1986 *Passive and Active Filters: Theory and Implementations* (Hoboken: Wiley)

[90] Koh B H and Ray L R 2004 Feedback Controller Design for Sensitivity-Based Damage Localization *J. Sound Vib.* **273** 317–35

[91] Jiang L J and Wang K W 2009 An Experiment-based Frequency Sensitivity Enhancing Control Approach for Structural Damage Detection *Smart Mater. Struct.* **18** 65005

[92] Jiang L J, Tang J and Wang K W 2007 An Optimal Sensitivity-Enhancing Feedback Control Approach via Eigenstructure Assignment for Structural Damage Identification *J. Vib. Acoust.* **129** 771

[93] Zorin A 1996 Quantum-limited Electrometer Based on Single Cooper Pair Tunneling. *Phys. Rev. Lett.* **76** 4408–11

[94] Vijay R, Devoret M H and Siddiqi I 2009 Invited Review Article: The Josephson Bifurcation Amplifier. *Rev. Sientific Instruments* **80** 111101

[95] Zhang W and Turner K L 2005 Application of Parametric Resonance Amplification in A Single-Crystal Silicon Micro-oscillator Based Mass Sensor *Sensors Actuators A Phys.* **122** 23–30

[96] Younis M I and Alsaleem F 2009 Exploration of New Concepts for Mass Detection in Electrostatically-Actuated Structures Based on Nonlinear Phenomena *J. Comput. Nonlinear Dyn.* **4** 21010

[97] Kumar V, Boley J W, Yang Y, Ekowaluyo H, Miller J K, Chiu G T-C and Rhoads J F 2011 Bifurcation-Based Mass Sensing Using Piezoelectrically-Actuated Microcantilevers *Appl. Phys. Lett.* **98** 153510

[98] Harne R L and Wang K W 2014 A Bifurcation-Based Coupled Linear-Bistable System for Microscale Mass Sensing *J. Sound Vib.* **333** 2241–52

[99] Lifshitz R and Cross M 2008 Nonlinear Dynamics of Nanomechanical and Micromechanical Resonators *Reviews of Nonlinear Dynamics and Complexity* ed H G Schuster (Hoboken: Wiley-VCH)

[100] Lim J and Epureanu B I 2012 Forecasting Bifurcation Morphing: Application to Cantilever-based Sensing *Nonlinear Dyn.* **67** 2291–8

[101] Lim J and Epureanu B I 2011 Forecasting a Class of Bifurcations: Theory and Experiment *Phys. Rev. E* **83** 16203

[102] Lim J and Epureanu B I 2011 Exploiting Delayed Nonlinear Feedback for Sensing Based on Bifurcation Morphing *Int. J. Struct. Stab. Dyn.* **11** 621–40

[103] Harne R L and Wang K W 2013 Robust Sensing Methodology for Detecting Change with Bistable Circuitry Dynamics Tailoring *Appl. Phys. Lett.* **102** 203506

[104] Paek J, Chintalapudi K, Govindan R, Caffrey J and Masri S 2005 A Wireless Sensor Network for Structural Health Monitoring: Performance and Experience *Embedded Networked Sensors, 2005. EmNetS-II. The Second IEEE Workshop on* pp 1–10

[105] Kuznet͡sov Y A 1998 *Elements of Applied Bifurcation Theory* (Springer)

[106] Kovacic I and Brennan M J 2011 *The Duffing Equation: Nonlinear Oscillators and their behavior* (Hoboken: John Wiley & Sons Ltd)

[107] Devoret M H, Esteve D, Martinis J M, Cleland A and Clarke J 1987 Resonant Activation of a Brownian Particle out of a Potential Well: Microwave-enhanced Escape from the Zero-voltage State of a Josephson Junction *Phys. Rev. B* **36** 58–73

[108] Aldridge J S and Cleland a. N 2005 Noise-enabled Precision Measurements of a Duffing Nanomechanical Resonator *Phys. Rev. Lett.* **94** 156403

[109] Stambaugh C and Chan H B 2006 Noise-activated Switching in a Driven Nonlinear Micromechanical Oscillator *Phys. Rev. B - Condens. Matter Mater. Phys.* **73** 172302

[110] Koper M T M 1998 Non-linear Phenomena in Electrochemical Systems *J. Chem. Soc. Faraday Trans.* **94** 1369–78

[111] Dakos V, Van Nes E H, D'Odorico P and Scheffer M 2012 Robustness of Variance and Autocorrelation as Indicators of Critical Slowing Down *Ecology* **93** 264–71

[112] Scheffer M, Carpenter S R, Lenton T M, Bascompte J, Brock W, Dakos V, van de Koppel J, van de Leemput I a., Levin S a., van Nes E H, Pascual M and Vandermeer J 2012 Anticipating Critical Transitions *Science (80-.).* **338** 344–8

[113] D'Souza K, Epureanu B I and Pascual M 2015 Forecasting Bifurcations from Large Perturbation Recoveries in Feedback Ecosystems *PLoS One* **10** e0137779

[114] Lenton T M 2011 Early Warning of Climate Tipping Points *Nat. Clim. Chang.* **1** 201–9

[115] Scheffer M, Bascompte J, Brock W a, Brovkin V, Carpenter S R, Dakos V, Held H, van

Nes E H, Rietkerk M and Sugihara G 2009 Early-warning Signals for Critical Transitions. *Nature* **461** 53–9

[116] Hanggi P 1986 Escape from a Metastable State *J. Stat. Phys.* **42** 105–48

[117] Meunier C and Verga A D 1988 Noise and bifurcations *J. Stat. Phys.* **50** 345–75

[118] Dykman M I, Schwartz I B and Shapiro M 2005 Scaling in Activated Escape of Underdamped Systems *Phys. Rev. E - Stat. Nonlinear, Soft Matter Phys.* **72** 1–8

[119] Lu C-H and Evan-Iwanowski R M 1994 The Nonstationary Effects on a Softening Duffing Oscillator *Mech. Res. Commun.* **21** 555–64

[120] Mandel P and Erneux T 1987 The Slow Passage Through a Steady Bifurcation: Delay and Memory Effects *J. Stat. Phys.* **48** 1059–70

[121] Breban R, Nusse H and Ott E 2003 Scaling Properties of Saddle-node Bifurcations on Fractal Basin Boundaries *Phys. Rev. E* **68** 66213

[122] Berglund N and Gents B 2006 *Noise-Included Phenomena in Slow-Fast Dynamical Systems: A Sample-Paths Approach* (Springer)

[123] Kuehn C 2015 *Multiple Time Scale Dynamics* (New York: Springer)

[124] Nicolis C and Nicolis G 2014 Dynamical Responses to Time-dependent Control Parameters in the Presence of Noise: A Normal Form Approach *Phys. Rev. E* **89** 1–14

[125] Miller N J and Shaw S W 2012 Escape statistics for parameter sweeps through bifurcations *Phys. Rev. E* **85** 46202

[126] Kim J, Harne R L and Wang K W 2017 Predicting Non-Stationary and Stochastic Activation of Saddle-Node Bifurcation *J. Comput. Nonlinear Dyn.* **12** 11009

[127] Leine R I and Van Campen D H 2002 Stick-slip Whirl Interaction in Drillstring Dynamics *J. Vib. Acoust.* **124** 209–20

[128] Sung C K and Yu W S 1992 Dynamics of a Harmonically Excited Impact Damper: Bifurcations and Chaotic Motion *J. Sound Vib.* **158** 317–29

[129] Holmes P, Full R J, Koditschek D and Guckenheimer J 2006 The Dynamics of Legged Locomotion: Models, Analyses, and Challenges *SIAM Rev.* **48** 207–304

[130] Iqbal S, Zang X, Zhu Y and Zhao J 2014 Bifurcations and Chaos in Passive Dynamic Walking: A Review *Rob. Auton. Syst.* **62** 889–909

[131] di Bernardo M, Budd C J, Champneys A R, Kowalczyk P, Nordmark A B, Tost G O and

Piiroinen P T 2008 Bifurcations in Nonsmooth Dynamical Systems ∗ **50** 629–701

[132] Kim J, Harne R L and Wang K W 2015 Enhancing Structural Damage Identification Robustness to Noise and Damping With Integrated Bistable and Adaptive Piezoelectric Circuitry *J. Vib. Acoust.* **137** 11005

[133] Chua L 1994 Chua's Circuit 10 Years Later *Int. J. Circuit Theory Appl.* **22** 279–305

[134] Zhao X, Schaeffer D G, Berger C M, Krassowska W and Gauthier D J 2008 Cardiac Alternans Arising From an Unfolded Border-Collision Bifurcation *J. Comput. Nonlinear Dyn.* **3** 41004

[135] Caballé J, Jarque X and Michetti E 2006 Chaotic Dynamics in Credit Constrained Emerging Economies *J. Econ. Dyn. Control* **30** 1261–75

[136] Mosekilde E and Laugesen J L 2007 Nonlinear Dynamic Phenomena in the Beer Model *Syst. Dyn. Rev.* **23** 229–52

[137] Simpson D J W 2010 *Bifurcations in Piecewise-Smooth Continuous Systems* (Singapore: World Scientific Publishing Co. Pte. Ltd)

[138] Leine R I and Nijmeijer H 2004 *Dynamics and Bifurcations of Non-Smooth Mechanical Systems* vol 18(Springer-Verlag)

[139] di Bernardo M, Budd C J C J, Champneys A R A R and Kowalczyk P 2008 *Piecewise-smooth Dynamical Systems: Theory and Applications* (Springer)

[140] Natsiavas S 1989 Periodic Response and Stability of Oscillators with Symmetric Trilinear Restoring Force *J. Sound Vib.* **134** 315–31

[141] Masri S F and Caughey T K 1966 On the Stability of the Impact Damper *J. Appl. Mech.* **33** 586–92

[142] Shaw S W and Holmes P J 1983 A Periodically Forced Piecewise Linear Oscillator *J. Sound Vib.* **90** 129–55

[143] Luo A C J 2005 The Mapping Dynamics of Periodic Motions for a Three-piecewise Linear System under a Periodic Excitation *J. Sound Vib.* **283** 723–48

[144] Kuehn C 2009 Scaling of Saddle-node Bifurcations: Degeneracies and Rapid Quantitative Changes *J. Phys. A Math. Theor.* **42** 45101

[145] Risken H 1983 *The Fokker-Planck Equation: Methods of Solution and Applications* (Springer-Verlag)

[146] Tamasevicius A, Mykolaitis G, Pyragas V and Pyragas K 2007 Delayed Feedback Control of Periodic Orbits without Torsion in Nonautonomous Chaotic Systems: Theory and Experiment *Phys. Rev. E* **76** 26203

[147] Forgoston E and Schwartz I B 2009 Escape Rates in a Stochastic Environment with Multiple Scales *SIAM J. Appl. Dyn. Syst.* **8** 1190–217

[148] Holmes P 1979 A Nonlinear Oscillator with a Strange Attractor *Philos. Trans. R. Soc. A Math. Phys. Sci.* **292** 419–48

[149] Rizzoni G 2009 *Fundamentals of Electrical Engineering* (New York: McGraw-Hill)

[150] Higham. D J 2001 An Algorithmic Introduction to Numerical Simulation of Stochastic Differential Equations *SIAM Rev.* **43** 525–46

[151] Kim J and Wang K W 2014 An Enhanced Impedance-based Damage Identification Method using Adaptive Piezoelectric Circuitry *Smart Mater. Struct.* **23** 95041

[152] Szemplinska-Stupnicka W and Rudowski J 1993 Steady States in the Twin-well Potential Oscillator: Computer Simulations and Approximate Analytical Studies. *Chaos* **3** 375–85

[153] Chung K W, He Y B and Lee B H K 2009 Bifurcation Analysis of a Two-degree-of-freedom Aeroelastic System with Hysteresis Structural Nonlinearity by a Perturbation-incremental Method *J. Sound Vib.* **320** 163–83

[154] Grillo S, Massucco S, Morini A, Pitto A and Silvestro F Bifurcation Analysis and Chaos Detection in Power Systems *Universities Power Engineering Conference, 2008. UPEC 2008. 43rd International IEEE.* pp 1–6

[155] Guttal V and Jayaprakash C 2007 Impact of Noise on Bistable Ecological Systems *Ecol. Modell.* **201** 420–8

[156] May R M, Levin S a and Sugihara G 2008 Complex systems: ecology for bankers. *Nature* **451** 893–5